ATOMIC DATA GENERATION AND COLLISIONAL RADIATIVE MODELING OF AR II, AR III,

AND NE I FOR LABORATORY AND ASTROPHYSICAL PLASMAS

Except where reference is made to the work of others, the work described in this dissertation is my own or was done in collaboration with my advisory committee. This dissertation does not include proprietary or classified information.

_____
Jorge Manuel Muñoz Burgos

Certificate of Approval:

_____   _____
Robert F. Boivin, Co-Chair   Stuart D. Loch, Co-Chair
Assistant Professor   Assistant Professor
Physics   Physics

_____   _____
Michael S. Pindzola   Yu Lin
Professor   Professor
Physics   Physics

_____
George T. Flowers
Dean
Graduate School

ATOMIC DATA GENERATION AND COLLISIONAL RADIATIVE MODELING OF AR II, AR III,

AND NE I FOR LABORATORY AND ASTROPHYSICAL PLASMAS

Jorge Manuel Muñoz Burgos

A Dissertation

Submitted to

the Graduate Faculty of

Auburn University

in Partial Fulfillment of the

Requirements for the

Degree of

Doctor of Philosophy

Auburn, Alabama
August 10, 2009

ATOMIC DATA GENERATION AND COLLISIONAL RADIATIVE MODELING OF AR II, AR III,

AND NE I FOR LABORATORY AND ASTROPHYSICAL PLASMAS

Jorge Manuel Muñoz Burgos

Permission is granted to Auburn University to make copies of this dissertation at its
discretion, upon the request of individuals or institutions and at
their expense. The author reserves all publication rights.

_____
Signature of Author

_____
Date of Graduation

Jorge Manuel Muñoz Burgos, son of Jorge Armando Muñoz Pacheco and Esther Burgos Serrano, was born on October 21th, 1976, in the city of Guadalajara in the state of Jalisco, Mèxico. He attended Preparatoria Varonil U.A.G. in Guadalajara, and graduated June 10th, 1994. He entered Universidad Autonoma de Guadalajara in August, 1994 and received a B. S. degree in Electrical Engineering and Communications in June 27th, 1998. After graduation he worked from June 1998 to August 1999 as Research and Development Engineer for Sistemas y Accesos Controlados S.A. de C.V. (Now Hydra Technologies, www.hydra-technologies.com) in Guadalajara, Mèxico. In January, 2000, he entered the graduate program at Florida Institute of Technology in Melbourne, Florida. He obtained a M. S. degree in Electrical Engineering in Electromagnetics in July, 2001, and a M. S. degree in Physics in August, 2003. He attended Auburn University from August, 2003 to July, 2009, where he obtained the Ph.D. degree in Physics. He has been offered a postdoctoral position at General Atomics in San Diego, California, to conduct research in Plasma Boundary Interface at the DIII-D TOKAMAK Nuclear Fusion Experimental Reactor.

Dissertation Abstract

Atomic Data Generation and Collisional Radiative Modeling of Ar II, Ar III, and Ne I for Laboratory and Astrophysical Plasmas

Jorge Manuel Muñoz Burgos

Doctor of Philosophy, August 10, 2009
(M.S. Physics, Florida Institute of Technology, 2003)
(M.S. EE, Florida Institute of Technology, 2001)
(B.S. EE, Universidad Autonoma de Guadalajara, 1998)

206 Typed Pages

Directed by Stuart D. Loch and Robert F. Boivin

Accurate knowledge of atomic processes plays a key role in modeling the emission in laboratory as well as in astrophysical plasmas. These processes are included in a collisional-radiative model and the results are compared with experimental measurements for Ar and Ne ions from the ASTRAL (Auburn Steady sTate Research fAciLity) experiment. The accuracy of our model depends upon the quality of the atomic data we use. Atomic data for near neutral systems present a challenge due to the low accuracy of perturbative methods for these systems. In order to improve our model we rely on non-perturbative methods such as R-Matrix and RMPS (R-Matrix with Pseudo-States) to include correlation in the collision cross-sections. These methods are computationally demanding, requiring supercomputing resources, and producing very accurate atomic collision data. For Ar^+ and Ne, R-Matrix data was already available, however for Ar^{2+} we had to set up new R-Matrix calculations. To set up a new calculation we require good quality atomic structure. A new code (LAMDA) was developed to optimize the atomic structure for different ions in AUTOSTRUCTURE. The AUTOSTRUCTURE code was used and optimized by systematically adjusting the orbital scale factors with the help of a Singular Value Decomposition algorithm.

We then tested the quality of our newly optimized atomic structure by comparing the level or term energies, and line strengths from our optimized structure with those given by NIST.

In the case of Ar^+ we compared R-Matrix electron-impact excitation data against the results from a new RMPS calculation. The aim was to assess the effects of continuum-coupling effects on the atomic data and the resulting spectrum. We do our spectral modeling using the ADAS suite of codes. Our collisional-radiative formalism assumes that the excited levels are in quasi-static equilibrium with the ground and metastable populations. In our model we allow for N_e and T_e variation along the line of sight by fitting our densities and temperature profiles with those measured within the experiment. The best results so far have been obtained by the fitting of the experimental temperature and density profiles with $Gaussian$ and polynomial distribution functions. The line of sight effects were found to have a significant effect on the emission modeling.

The relative emission rates were measured in the ASTRAL helicon plasma source. A spectrometer which features a 0.33 m Criss-Cross Scanning monochromator and a CCD camera is used for this study. ASTRAL produces bright intense Ar and Ne plasmas with $n_e = 10^{11}$ to 10^{13} cm^{-3} and $T_e = 2$ to 10 eV. A series of 7 large coils produce an axial magnetic field up to 1.3 kGauss. A fractional helix antenna is used to introduce RF power up to 2 kWatt. Two RF compensated Langmuir probes are used to measure T_e and N_e. In a series of experiment Ar II, Ar III, and Ne transitions are monitored as a function of T_e, while N_e is kept nearly constant. Observations revealed that T_e is by far the most significant parameter affecting the emission rate coefficients, thus confirming our predictions. The spectroscopy measurements are compared with those from our spectral modeling which in turn help us to compare the effectiveness of the new atomic data calculations with those from other calculations. It also shows some differences between the R-Matrix and the RMPS data due to continuum coupling effects for Ar II, and Ne. We believe that this is the first experimental observation of continuum-coupling effects.

We performed a new R-Matrix calculation for Ar^{2+}. Emission from Ar^{2+} is seen in planetary nebulae, in H II regions, and from laboratory plasmas. Our calculation improved upon existing electron-impact excitation data for the $3p^4$ configuration of Ar^{2+} and calculated new data for the excited levels. Electron-impact excitation collision strengths were calculated using the R-Matrix intermediate-coupling (IC) frame-transformation method and the R-Matrix Breit-Pauli method. Excitation cross-sections are calculated between all levels of the configurations $3s^2\,3p^4$, $3s\,3p^5$, $3p^6$, $3p^5\,3d$, and $3s^2\,3p^3$ nl ($3d \leq nl \leq 5s$). $Maxwellian$ effective collision strengths are generated from the collision strength data. Good agreement is found in the collision strengths calculated using the two R-Matrix methods. The effects of the new data on line ratio diagnostics were studied. The collision strengths are compared with literature values for transitions within the $3s^2\,3p^4$ configuration. The new data has a small effect on T_e values obtained from the $I(\lambda 7135\mathring{A} + \lambda 7751\mathring{A})/I(\lambda 5192\mathring{A})$ line ratio, and a larger effect on the N_e values obtained from the $I(\lambda 7135\mathring{A})/I(\lambda 9\mu m)$ line ratio. The final effective collision strength data is archived online.

Neon as well as Argon is a species of current interest in fusion TOKAMAK studies. It is used for radiative cooling of the divertor region and for disruption mitigation. It could also be useful as a spectral diagnostic if better atomic data were available. We present results from modeling emission line intensity for neutral neon by using Plane Wave $Born$, R-Matrix, and RMPS electron-impact excitation calculations. We benchmark our theoretical calculations against cross-section measurements, then against spectral measurements from ASTRAL.

ACKNOWLEDGMENTS

It is written: *The fear of the Lord is the beginning of knowledge, But fools despise wisdom and instruction* (Proverbs 1:7). Or, as Psalm 19:1,2 says: *The heavens declare the glory of God; And the firmament shows His handiwork. Day unto day utters speech, And night unto night reveals knowledge.* To You my *God*, *Lord*, *Savior*, and *King Jesus Christ*, for always being with me, and for showing me that through You all things are possible. To You alone be the kingdom, the power, and the glory forever. To my loving mother Esther, for her faith, hard work, and prayers. Thank you for taking care of us during the hard times and for teaching us to love the *God* of *Abraham*, *Isaac*, and *Jacob* in Whose loving and mighty hand we stand. To my brother Alex, and sister Erika, for all their love and support. To my deceased dad Jorge whom I hope to see one day in glory. For all the rest of my dear and supportive family and friends, thank you for all your encouragement and prayers. To the selfless help, support, and hard working example from my two academic advisors and friends Dr. Stuart D. Loch in the theoretical aspect, and Dr. Robert F. Boivin in the experimental. Thank you for all your help, patience, and guidance. To Dr. Connor P. Ballance, for all his help, time, hard work, and patience in helping us understand the R-Matrix theory, and teaching us to use the parallel codes that played a key role in the development of this dissertation. To all my doctoral committee members; Dr. Michael S. Pindzola, Dr. Yu Lin, and Dr. Michael L. McKee, thank you for taking the time to review this dissertation. To Dr. Oleg V. Batishchev from MIT, thank you for your encouragement and support. To Auburn University, a very special place where I made such wonderful friends. To the hard working people of my native country *México*, to the wonderful people of *The United States of America* for kindly opening the doors for me in your beautiful country, and to the beloved children of *Israel*, a testimony that *God* is always faithful and truthful. May *God* bless you all.

Style manual or journal used Journals of the American Physical Society (together with the style known as "auphd"). Bibliography follows the style used by the American Physical Society.

Computer software used The document preparation package TeX (specifically LaTeX) together with the departmental style-file `auphd.sty`.

TABLE OF CONTENTS

INTRODUCTION

Spectral emission modeling has been key for many diagnostics in astrophysical and laboratory plasmas. This modeling has particular interest in the field of astrophysics when studying emission from planetary nebulae, solar corona, or the interstellar medium, which cannot be accessed with probes. In laboratory plasmas the conditions are often too hostile for probe measurements. Therefore we require accurate models for the atomic processes involved in plasma emission in order to get a reliable interpretation of spectral observations. Several challenges arise when trying to model the spectral emission coming from a hot plasma, and in developing plasma spectral diagnostics. These difficulties include the need for accurate atomic data, knowledge of the temperature and density distributions within the plasma, and an understanding of the plasma and atomic timescales.

Emission from Ar II, Ar III, and Ne I will be the main focus of the work described here. The emission from these species in the ASTRAL Auburn helicon plasma source will be modeled with two main purposes in mind. Firstly we seek to use the experiment to test the atomic data for Ar and Ne. Secondly we intend to develop spectral diagnostics that can be used for other Ar and Ne plasmas. Ar and Ne are of interest in fusion TOKAMAK plasmas to radiatively cool the divertor and to mitigate plasma disruptions. Ar is of special interest in planetary nebulae spectroscopy, with forbidden lines for Ar III being used as T_e and N_e diagnostics. In the remainder of this chapter a brief overview of the rest of the dissertation will be given.

Chapter 2 deals with the general concepts of modeling spectral emission and introduces different atomic processes that contribute to the population of specific atomic levels. We introduce the collisional-radiative model [1] used in modeling the emission from plasmas. We also describe our application of collisional-radiative theory to the calculation of excited populations and ionization balance using the Atomic Data Analysis Structure (ADAS) suite of codes. This method encompasses both the low density coronal, and high density Local Thermodynamic Equilibrium (LTE) description of the emission from the ion we intend to model. It also includes ionization and recombination processes to and from metastable levels of the next ionization stage.

Chapter 3 describes calculations of atomic structure that are needed for computing electron-impact ionization as well as electron-impact excitation cross-sections. The accuracy of the atomic structure of the atom and/or ion is essential in the calculation of atomic collision quantities. In order to calculate our atomic structure we make use of the AUTOSTRUCTURE [2] code. We also make use of the graphical interface version of the AUTOSTRUCTURE code, GASP [3], to simplify our calculation procedures. We also explore the capability of fine tuning our atomic structure by the introduction of variational adjustment of scale factors (λs). We propose and use a new optimization procedure base on Singular Value Decomposition (SVD) [4] to calculate the optimal scale factors that we need in order to optimize and improve our the quality of our atomic structure.

Chapter 4 gives a general description of some of the most widely used methods to calculate electron-impact ionization data and electron-impact excitation data. We start in section 4.2 with an explanation of the Plane Wave $Born$ approximation, where the incoming electron is described by a plane wave, and the target as a static isotropic potential.

In section 4.3 we give a short introduction to Distorted Wave theory, where we allow the incoming wave to be affected by the target potential and therefore be distorted. We also give a short introduction to R-Matrix theory in section 4.5, and explain the use of pseudo-states, or R-Matrix with Pseudo-States (RMPS), in order to model the interactions with the continuum which also help us improve our atomic structure. These methods will be used throughout the dissertation for the collisional atomic data that will be used in the spectral emission modeling. In section 4.5 we give an overview of the Burgess-Tully plots [5]. These plots allow us to display electron-impact excitation data in a dimensionless way by using suitable scaling procedures. These scaling procedures remove the main asymptotic energy (or temperature) dependence for the given data. The energy (temperature) is also scaled so as to become a dimensionless variable which ranges from 0 at the threshold energy (zero temperature) to 1 at infinite energy (temperature). This way we can display the whole variation of a collision strength in a single graph, and help us to compare the whole data with previous calculations.

Chapter 5 gives a description of the **A**uburn **S**teady s**T**ate **R**esearch f**A**ci**L**ity ASTRAL. This is a helicon device where we generate intense Ar and Ne plasma columns in order to study and measure spectral-line emission of plasmas and test them at different plasma conditions. Although in our work we focus mainly in Ar and Ne emission, ASTRAL has also been used to study He and CO_2 plasma emission. We discuss the efficiency of the helicon source as a mean to generate dense plasmas heated by radio waves. Helicon sources are very useful for basic plasma studies. Helicon devices also have the advantage that the antenna is outside the plasma, which helps reducing the introduction of contaminants into the plasma. In this chapter we also describe measurements of the plasma densities and temperatures by using two RF compensated $Langmuir$ probes.

These measurements form the benchmark in which we compare our collisional-radiative model for Ar and Ne, with the aim of developing reliable non-invasive methods for plasma diagnostic based on spectral line ratio measurements. In our spectral analysis we compensate for wavelength due to the response of the spectrometer to different spectral regions. We have used an absolutely calibrated Oriel Halogen Lamp in order to measure the response of the spectrometer as a function of wavelength. In appendix B we present a short discussion of the wavelength calibration procedures.

Chapter 6 deals with the modeling of the Ar II emission, as well as experimental measurements of line intensities and ratios in order to develop temperature diagnostics for argon plasmas. The accuracy of the modeling depends on the quality of the atomic data. Therefore one of the aims of this work is to use this experimental data to determine if the Ar experimental emission from ASTRAL can be used to test newly calculated atomic data sets in our collisional-radiative model. We use the spectral measurements to test recent dielectronic recombination (DR) data for the low charge states of argon. We also identify Ar II line ratios that are sensitive to continuum coupling effects in the excitation cross-sections. These ratios could be used to benchmark new RMPS electron-impact excitation data [6], and show where previous non-pseudo-states data [47] may be insufficient for the modeling. This could provide the first experimental observation of continuum coupling effects.

Chapter 7 presents a new R-Matrix calculation for the Ar^{2+} ion with an optimized atomic structure calculation. We compare our new calculation with previous R-Matrix calculations performed by Johnson & Kingston [7], and Galavis et al. [8]. Johnson & Kingston calculated excitations within the configuration $3s^23p^4$ and $3s3p^5$ of Ar^{2+}. Their calculation was generated in (LS) coupling and transformed to level-resolution using the JAJOM (Saraph [9]) method. Galavis also used the R-Matrix method to calculate level-resolved excitations within the $3s^23p^4$ configuration. They used a large configuration-interaction calculation to get their atomic structure. We compare these calculations and we then discuss the applications of Ar III forbidden line spectra as electron temperature and density diagnostics of planetary nebula [10]. We also identify some temperature sensitive line ratios that could be observed in laboratory plasmas.

Chapter 8 employs different sets of electron-impact excitation data in the collisional-radiative model, in order to predict intensity line emission from neutral neon plasmas. We first use Plane Wave $Born$ (see section 4.2) electron-impact excitation data calculated by Martin O'Mullane, and available in the ADAS [11] database. This represents the modeling currently used in the fusion community. We also use R-Matrix excitation data calculated by Zatsarinny and Bartschat [72]. We then compare the atomic structures, excitation cross-sections, and emission modeling with new RMPS (LS) and R-Matrix (IC) electron-impact excitation data calculated by Griffin and Ballance [71]. The line emission modeling predictions from each of the data sets is then compared with different sets of experimental measurements from ASTRAL. We find that none of the data sets are in complete agreement with the experimental measurements, likely due to physical effects missing in each of the data sets. The comparison suggests that a level-resolved R-Matrix with Pseudo-States calculation is required to model Ne spectral emission in low temperature, high density plasmas.

COLLISIONAL-RADIATIVE MODEL

2.1 Introduction

To produce a modeled spectrum one needs to account for all the populating mechanisms in a collisional-radiative model. Our application of collisional-radiative theory to the calculation of excited populations is based on the Atomic Data Analysis Structure (ADAS) suite of codes to our population and emission modeling [11]. These codes are based on the collisional-radiative theory first developed by Bates, Kingston, and McWhirter [1] in 1962, and later generalized by Summers and Hooper [12, 13]. Supplementary details related to the collisional-radiative formalism can be found in Burgess and Summers [14]. The method aims to encompass both the low density coronal and the high density Local Thermodynamic Equilibrium (LTE) description of an ion, and to track the shifting balance between radiative and collisional processes. The ion consists of a set of levels with radiative and collisional couplings. Ionization and recombination to and from metastables of the next ionization stage (i.e. the plus ion stage) are included.

2.2 Atomic Processes

There are many kinds of processes that play a role in populating a level. In order to accurately build the collisional-radiative model we must account for each atomic process that contributes to the population in an individual level. These include (but are not limited to)

- Spontaneous decay ($A_{i \rightarrow j}$)

- Auger rate ($A^a_{i \rightarrow \sigma}$)

- Electronic collisional excitation/de-excitation ($q^e_{i \rightarrow j}$/ $q^e_{j \rightarrow i}$)

- Ionization ($S_{i \rightarrow \sigma}$)

- Recombination: radiative (α^r_i), dielectronic (α^d_i), and three-body (α^3_i)
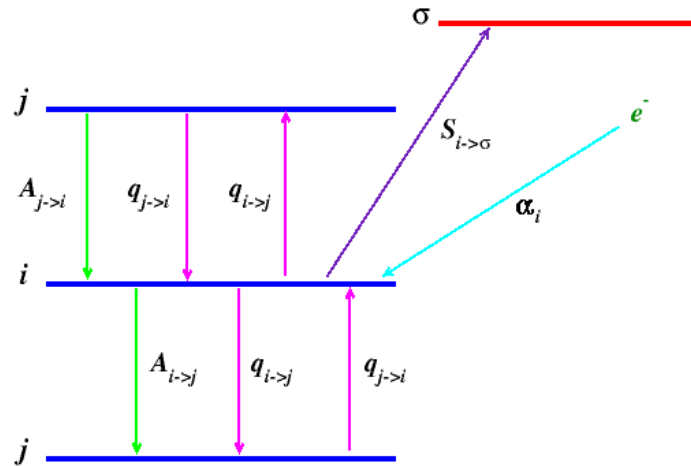
Figure 2.1: Populating processes for the ith atomic level.

Figure 2.1 illustrates some of the processes that contribute to the population for the ith atomic level. Where i represents the specific level we describe, j represents any higher or lower energy level than i, and σ denotes the ground and metastable indices of the $z + 1$ ion stage. Notice that other processes such as charge exchange or proton collisions can be included in the collisional-radiative formalism. For this work we will ignore both of these processes.

2.3   Equations and Matrix Representation

The ion consists of a set of levels with radiative and collisional couplings. The time dependence of the population N_i of an arbitrary level i, in ion stage $+z$ is given by the next set of coupled differential equations

$$\frac{dN_i}{dt} = \sum_\sigma n_e N_\sigma^{z+1}(\alpha_i^r + \alpha_i^d + n_e\alpha_i^3) + \sum_{j<i} N_j n_e q_{j\rightarrow i}^e + \sum_{j>i} N_j(n_e q_{j\rightarrow i}^e + A_{j\rightarrow i})$$
$$- N_i\left\{\sum_{j>i} n_e q_{i\rightarrow j}^e + \sum_{j<i}(n_e q_{i\rightarrow j}^e + A_{i\rightarrow j}) + \sum_\sigma (n_e S_{i\rightarrow\sigma} + A_{i\rightarrow\sigma}^a)\right\} \tag{2.1}$$

where n_e is the free electron density. It can be shown [11] that we can reduce this equation to a more compact form

$$\frac{dN_i}{dt} = \sum_\sigma n_e N_\sigma^{z+1} r_{i\sigma} + \sum_j C_{ij} N_j \tag{2.2}$$

with a populating term for $i \neq j$,

$$C_{ij} = A_{j\rightarrow i} + n_e q_{j\rightarrow i}^e + n_e q_{j\rightarrow i}^p \tag{2.3}$$

a loss term for $i = j$,

$$C_{ii} = -\left(\sum_{i>j} A_{i\rightarrow j} + n_e \sum_{j\neq i} q_{i\rightarrow j}^e + \sum_\gamma n_e S_{i\gamma} + \sum_\gamma A_{i\gamma}^a\right) \tag{2.4}$$

and a composite recombination coefficient $r_{i\sigma} = \alpha_i^r + \alpha_i^d + N_e \alpha_i^3$. This way we can rewrite equation (2.2) s

$$\sum_j C_{ij} N_j = \frac{dN_i}{dt} - \sum_\sigma n_e N_\sigma^{z+1} r_{i\sigma} \qquad (2.5)$$

or in the matrix form

$$
\begin{pmatrix}
C_{11} & C_{12} & \dots & C_{1N} \\
C_{21} & C_{22} & \dots & C_{2N} \\
\vdots & \vdots & \ddots & \vdots \\
C_{N1} & C_{N2} & \dots & C_{NN}
\end{pmatrix}
\cdot
\begin{pmatrix}
N_1 \\
N_2 \\
\vdots \\
N_N
\end{pmatrix}
=
\begin{pmatrix}
\frac{dN_1}{dt} - \sum_\sigma n_e N_\sigma^{z+1} r_{1\sigma} \\
\frac{dN_2}{dt} - \sum_\sigma n_e N_\sigma^{z+1} r_{2\sigma} \\
\vdots \\
\frac{dN_N}{dt} - \sum_\sigma n_e N_\sigma^{z+1} r_{N\sigma}
\end{pmatrix}
\qquad (2.6)
$$

where we define C as the collisional-radiative matrix. In order to solve the system we can simplify it considerably by taking into account the timescales of the system.

2.4 Timescales

For typical plasma conditions for TOKAMAK or Helicon devices, the excited levels have extremely fast radiative decay rates while the ground and metastable levels have much longer lifetimes. The excited levels can be assumed to be in instantaneous equilibrium with the ground and metastable populations. This is called the quasi-static approximation and results in all but the ground and metastable rate of change of populations being set to zero in equation (2.6). This allows the calculation of the excited populations to be split into two parts; an ionization balance calculation to work out the ground and metastable populations of each ion stage, and an excited level population calculation for the levels within a given ion stage.

2.4.1 Plasma Timescales

It can be shown [15] that the particle self-collision time is given by

$$\tau = 0.12 \frac{1}{\alpha c a_o^2} \left(\frac{m}{m_e} \right)^{1/2} \left(\frac{kT_e}{I_H} \right)^{3/2} \frac{1}{Nz^4 \ln \Lambda} \tag{2.7}$$

where $\Lambda = 12\pi n_e \lambda_D^3$ and λ_D is the $Debye$ length. From equation (2.7) we get the relative collision times

$$\tau_{ee} : \tau_{ii} : \tau_{ie} = 1 : \frac{1}{z^4} \left(\frac{m_i}{m_e} \right)^{1/2} \left(\frac{T_i}{T_e} \right)^{3/2} : \frac{1}{z^2} \left(\frac{\pi}{6} \right)^{1/2} \left(\frac{m_i}{m_e} \right) \tag{2.8}$$

Table 2.1 shows some approximate collision time values for coronal, as well as fusion divertor plasmas

Time (sec)	Solar Corona $n_e = 5 \times 10^8$ cm^{-3} $T_e \sim 10^6$ K	Fusion Plasma $n_e = 1 \times 10^{13}$ cm^{-3} $T_e \sim 1$ keV
τ_{ee}	0.18	3×10^{-4}
τ_{ii}	8	1.3×10^{-2}
τ_{ie}	200	0.5

Table 2.1: Typical collision time values.

In all of our modeling we will assume that the free electrons have a $Maxwellian$ distribution, thus all of our electron-impact excitation effective collision strengths will be generated for $Maxwellian$ free electrons.

2.4.2 Atomic Timescales

The relaxation timescales of an excited level i, can be estimated from

$$\tau_o \sim \frac{1}{\sum_j n_e q_{i \to j} + \sum_j A_{i \to j}} \tag{2.9}$$

Taking $A_{i \to j} \sim 10^8 (z + 1)^4$ we can approximate equation (2.9) by

$$\tau_o \sim \frac{10^{-8}}{(z + 1)^4} \tag{2.10}$$

Since the ground state cannot radiatively decay, therefore its time scale is determined by ionization

$$\tau_g \sim \frac{10^7}{n_e} (z + 1)^2 \left(\frac{I_H}{kT} \right)^{1/2} \exp(\chi/kT) \tag{2.11}$$

where χ is the ionization potential. If an excited state's radiative routes to lower levels all have low radiative transition probability (e.g. spin changing transitions) then it is classified as a metastable and $\tau_m \sim \tau_g$. Bound states with energy above the ionization limit may autoionize via interaction with the continuum. These states have extremely short lifetimes $\tau_a \sim 10^{-12}$ sec. Thus, we have the following timescale relations

$$\tau_a \ll \tau_o \ll \tau_m \sim \tau_g \tag{2.12}$$

2.5 Solution of the CR Matrix

Taking into consideration the relaxation time of the ground and metastables in comparison with the relaxation time from any other excited levels, we make use of the quasi-static approximation. Therefore, the excited levels reach equilibrium much faster than the ground/metastable due to all the excitations, de-excitations, and all the other processes that take place to contribute to their population. Taking into account an m number of metastables (including the ground state), we can rewrite some of the time derivatives in equation (2.6) subject to the conditions $\frac{dN_\rho}{dt} \neq 0$ for $1 \leq \rho \leq m$, and $\frac{dN_i}{dt} = 0$ for $i > m$, therefore we get

$$
\begin{pmatrix}
C_{11} & C_{12} & \ldots & C_{1N} \\
C_{21} & C_{22} & \ldots & C_{2N} \\
\vdots & \vdots & \ddots & \vdots \\
C_{m1} & C_{m2} & \ldots & C_{mN} \\
C_{m+11} & C_{m+12} & \ldots & C_{m+1N} \\
\vdots & \vdots & \ddots & \vdots \\
C_{N1} & C_{N2} & \ldots & C_{NN}
\end{pmatrix}
\cdot
\begin{pmatrix}
N_1 \\
N_2 \\
\vdots \\
N_m \\
N_{m+1} \\
\vdots \\
N_N
\end{pmatrix}
=
\begin{pmatrix}
\frac{dN_1}{dt} - \sum_\sigma n_e N_\sigma^{z+1} r_{1\sigma} \\
\frac{dN_2}{dt} - \sum_\sigma n_e N_\sigma^{z+1} r_{2\sigma} \\
\vdots \\
\frac{dN_m}{dt} - \sum_\sigma n_e N_\sigma^{z+1} r_{m\sigma} \\
-\sum_\sigma n_e N_\sigma^{z+1} r_{m+1\sigma} \\
\vdots \\
-\sum_\sigma n_e N_\sigma^{z+1} r_{N\sigma}
\end{pmatrix}
\tag{2.13}
$$

Setting the time dependence of the excited levels to zero, allows the population of an 'ordinary' level to be determined as a function of the ground and metastable populations of the Z ion stage (N_ρ), and of the $Z = 1$ ion stage (N_σ^{Z+1}). In order to achieve this goal we want to eliminate any time dependence on our system of equations. We can do this in just few steps by eliminating unnecessary time dependent differential equations. We start by rearranging equation (2.13).

We subtract every term that is multiplied by the first metastable state N_1 from the LHS, and add it to the RHS of equation (2.13). From here we get

$$
\begin{pmatrix}
C_{12} & \cdots & C_{1N} \\
C_{22} & \cdots & C_{2N} \\
\vdots & \ddots & \vdots \\
C_{m2} & \cdots & C_{mN} \\
C_{m+12} & \cdots & C_{m+1N} \\
\vdots & \ddots & \vdots \\
C_{N2} & \cdots & C_{NN}
\end{pmatrix}
\cdot
\begin{pmatrix}
N_2 \\
\vdots \\
N_m \\
N_{m+1} \\
\vdots \\
N_N
\end{pmatrix}
=
\begin{pmatrix}
\frac{dN_1}{dt} - \sum_\sigma n_e N_\sigma^{z+1} r_{1\sigma} - C_{11} N_1 \\
\frac{dN_2}{dt} - \sum_\sigma n_e N_\sigma^{z+1} r_{2\sigma} - C_{21} N_1 \\
\vdots \\
\frac{dN_m}{dt} - \sum_\sigma n_e N_\sigma^{z+1} r_{m\sigma} - C_{m1} N_1 \\
- \sum_\sigma n_e N_\sigma^{z+1} r_{m+1\sigma} - C_{m+11} N_1 \\
\vdots \\
- \sum_\sigma n_e N_\sigma^{z+1} r_{N\sigma} - C_{N1} N_1
\end{pmatrix}
\quad (2.14)
$$

Since we are only solving for the excited levels, we extract from equation (2.14) the differential equation for the first metastable state N_1

$$
\sum_{n=2}^{N} C_{1n} N_n = \frac{dN_1}{dt} - \sum_\sigma n_e N_\sigma^{z+1} r_{1\sigma} - C_{11} N_1
\qquad (2.15)
$$

13

therefore we obtain our equation in the reduced form

$$
\begin{pmatrix}
C_{22} & \cdots & C_{2N} \\
\vdots & \ddots & \vdots \\
C_{m2} & \cdots & C_{mN} \\
C_{m+12} & \cdots & C_{m+1N} \\
\vdots & \ddots & \vdots \\
C_{N2} & \cdots & C_{NN}
\end{pmatrix}
\cdot
\begin{pmatrix}
N_2 \\
\vdots \\
N_m \\
N_{m+1} \\
\vdots \\
N_N
\end{pmatrix}
=
\begin{pmatrix}
\frac{dN_2}{dt} - \sum_\sigma n_e N_\sigma^{z+1} r_{2\sigma} - C_{21} N_1 \\
\vdots \\
\frac{dN_m}{dt} - \sum_\sigma n_e N_\sigma^{z+1} r_{m\sigma} - C_{m1} N_1 \\
- \sum_\sigma n_e N_\sigma^{z+1} r_{m+1\sigma} - C_{m+11} N_1 \\
\vdots \\
- \sum_\sigma n_e N_\sigma^{z+1} r_{N\sigma} - C_{N1} N_1
\end{pmatrix}
\tag{2.16}
$$

By repeating the same procedure $m - 1$ number of times for the rest of metastables we end up reducing the equation to the form

$$
\begin{pmatrix}
C_{m+12} & \cdots & C_{m+1N} \\
\vdots & \ddots & \vdots \\
C_{N2} & \cdots & C_{NN}
\end{pmatrix}
\cdot
\begin{pmatrix}
N_{m+1} \\
\vdots \\
N_N
\end{pmatrix}
=
\begin{pmatrix}
- \sum_\sigma n_e N_\sigma^{z+1} r_{m+1\sigma} - \sum_{\rho=1}^{m} C_{m+1\rho} N_\rho \\
\vdots \\
- \sum_\sigma n_e N_\sigma^{z+1} r_{N\sigma} - \sum_{\rho=1}^{m} C_{N\rho} N_\rho
\end{pmatrix}
\tag{2.17}
$$

Finally, we can easily solve equation (2.17) and get the solution for the population of the jth 'ordinary' level in the form

$$
N_j^z = - \sum_\rho \sum_i C_{ji_{(r)}}^{-1} C_{i\rho} N_\rho^z - \sum_\sigma \sum_i C_{ji_{(r)}}^{-1} r_{i\gamma} N_\sigma^{z+1} n_e
\tag{2.18}
$$

Notice that the inverse matrix in equation (2.18) $C^{-1}_{ji_{(r)}}$ is not the inverse of the collisional-radiative matrix defined by equation (2.6), but rather the inverse of the reduced collisional-radiative matrix from equation (2.17). As equation (2.18) shows, the solution for the equilibrium population for any 'ordinary' level depends upon the "known" population of the ground and metastable levels. In order to get the ground and metastable population we calculate the ionization balance (see section 2.6) for the specified ion stage. We notice that in general these ground and metastable population could be generated from a non-equilibrium ionization balance calculation, with account taken for plasma transport effects. For the modeling of the ASTRAL plasma presented later in this dissertation, it will be shown that an equilibrium ionization balance calculation will be sufficient. Figure 2.2 shows the results of the population dependence on metastables ($\frac{N_i}{n_e N_1}$) as a function of electron density for the Ar^+ ion. We can clearly see the three different regimes (Coronal, Collisional-Radiative, and LTE). Our ASTRAL plasma has an electron density of $\sim 1 \times 10^{12}$ cm^{-3}, and is clearly in the collisional-radiative regime.
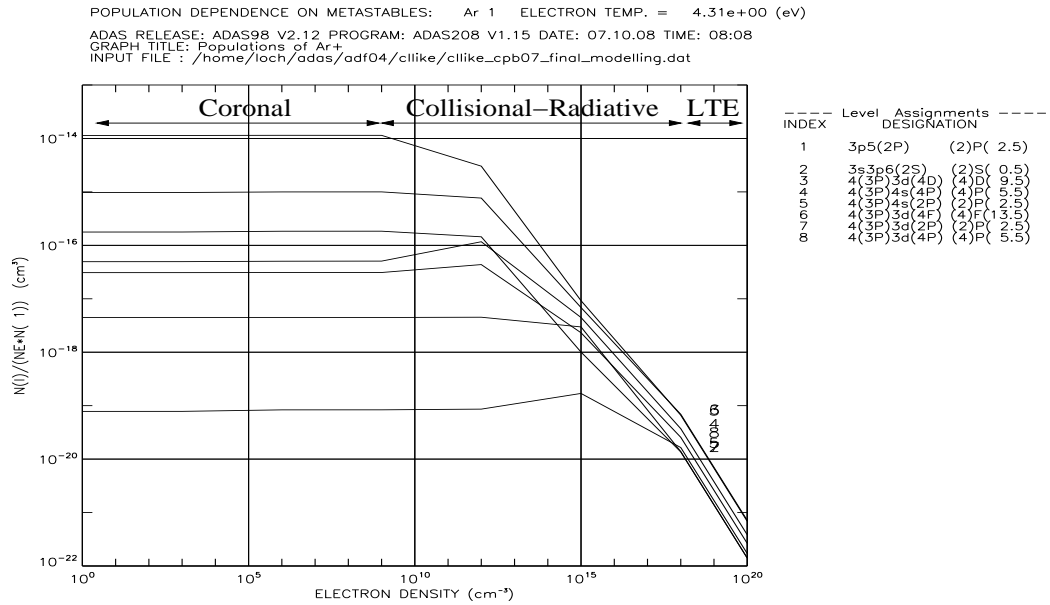
Figure 2.2: Normalized level population dependence with respect to electron density.

2.6 Ionization Balance Calculations

In order to solve our collisional-radiative model we need to know the ground and metastable populations of the ions of an element in equilibrium in a thermal plasma. Consider an element $\mathbf{X}$ of nuclear charge z_o, the populations of the ionization stages are denoted by

$$N_z : z = 0, \ldots, z_o \tag{2.19}$$

When considering the z ion stage we include in the calculation its own ionization $S_{z \to z+1}$, and only the ionization from the lowest ion stage $S_{z-1 \to z}$. When talking about recombination we will only include those from the adjacent ion stages; $\alpha_{z \to z-1}$, $\alpha_{z+1 \to z}$. The time dependence of the ionization stage populations is given by

$$\frac{dN_z}{dt} = n_e S_{z-1 \to z} N_{z-1} - \left(n_e S_{z \to z+1} + n_e \alpha_{z \to z-1} \right) N_z$$
$$+ n_e \alpha_{z+1 \to z} N_{z+1} \tag{2.20}$$

Rewriting equation (2.20) into matrix form we obtain

$$
\begin{pmatrix}
-n_e S_{0 \to 1} & n_e \alpha_{1 \to 0} & 0 & 0 & \ldots & 0 \\
n_e S_{0 \to 1} & -n_e \left(S_{1 \to 2} + \alpha_{1 \to 0} \right) & n_e \alpha_{1 \to 0} & 0 & \ldots & 0 \\
0 & n_e S_{1 \to 2} & . & . & \ldots & . \\
\vdots & \vdots & \vdots & \vdots & \ddots & \vdots \\
0 & 0 & . & . & \ldots & .
\end{pmatrix}
\cdot
\begin{pmatrix}
N_0 \\
N_1 \\
N_2 \\
\vdots \\
N_{z_o}
\end{pmatrix}
=
\begin{pmatrix}
\frac{dN_0}{dt} \\
\frac{dN_1}{dt} \\
\frac{dN_2}{dt} \\
\vdots \\
\frac{dN_{z_o}}{dt}
\end{pmatrix}
\tag{2.21}
$$

16

subject to the normalization condition

$$N_{Tot} = \sum_{z=0}^{z_o} N_z \tag{2.22}$$

where N_{Tot} is the number density of ions of element $\mathbf{X}$ in any ionization stage. Including equation (2.22) into equation (2.21) and adding an extra column of zeros into the matrix to keep it square we get

$$
\begin{pmatrix}
-n_e S_{0\to 1} & n_e \alpha_{1\to 0} & 0 & \ldots & 0 & 0 \\
n_e S_{0\to 1} & -n_e\left(S_{1\to 2}+\alpha_{1\to 0}\right) & n_e\alpha_{1\to 0} & \ldots & 0 & 0 \\
0 & n_e S_{1\to 2} & . & \ldots & . & 0 \\
\vdots & \vdots & \vdots & \ddots & \vdots & \vdots \\
0 & 0 & . & \ldots & . & 0 \\
1 & 1 & 1 & \ldots & 1 & 0
\end{pmatrix}
\cdot
\begin{pmatrix}
N_0 \\
N_1 \\
N_2 \\
\vdots \\
N_{z_o} \\
0
\end{pmatrix}
=
\begin{pmatrix}
\frac{dN_0}{dt} \\
\frac{dN_1}{dt} \\
\frac{dN_2}{dt} \\
\vdots \\
\frac{dN_{z_o}}{dt} \\
N_{Tot}
\end{pmatrix}
\tag{2.23}
$$

In equilibrium ionization balance, the time derivatives are set to zero in equation (2.23). We write the solution of our ionization balance in the form

$$
\begin{pmatrix}
N_0 \\
N_1 \\
N_2 \\
\vdots \\
N_{z_o} \\
0
\end{pmatrix}
=
\begin{pmatrix}
-n_e S_{0\to 1} & n_e \alpha_{1\to 0}+n_H C_{1\to 0} & 0 & \ldots & 0 & 0 \\
n_e S_{0\to 1} & -n_e\left(S_{1\to 2}+\alpha_{1\to 0}\right) & n_e\alpha_{1\to 0} & \ldots & 0 & 0 \\
0 & n_e S_{1\to 2} & . & \ldots & . & 0 \\
\vdots & \vdots & \vdots & \ddots & \vdots & \vdots \\
0 & 0 & . & \ldots & . & 0 \\
1 & 1 & 1 & \ldots & 1 & 0
\end{pmatrix}^{-1}
\cdot
\begin{pmatrix}
0 \\
0 \\
0 \\
\vdots \\
0 \\
N_{Tot}
\end{pmatrix}
\tag{2.24}
$$

17

Finally, since we don't know the exact value for N_{Tot}, we solve for the equilibrium fractional abundances N_z/N_{Tot} at a set of temperatures and densities.

$$
\begin{pmatrix}
\frac{N_0}{N_{Tot}} \\
\frac{N_1}{N_{Tot}} \\
\frac{N_2}{N_{Tot}} \\
\vdots \\
\frac{N_{z_o}}{N_{Tot}} \\
0
\end{pmatrix}
=
\begin{pmatrix}
-n_e S_{0\to 1} & n_e \alpha_{1\to 0} & 0 & \ldots & 0 & 0 \\
n_e S_{0\to 1} & -n_e\left(S_{1\to 2} + \alpha_{1\to 0}\right) & n_e \alpha_{1\to 0} & \ldots & 0 & 0 \\
0 & n_e S_{1\to 2} & . & \ldots & . & 0 \\
\vdots & \vdots & \vdots & \ddots & \vdots & \vdots \\
0 & 0 & . & \ldots & . & 0 \\
1 & 1 & 1 & \ldots & 1 & 0
\end{pmatrix}^{-1}
\cdot
\begin{pmatrix}
0 \\
0 \\
0 \\
\vdots \\
0 \\
1
\end{pmatrix}
\tag{2.25}
$$

We notice that the above equations can be easily extended to include contributions from charge exchange and proton collisions. These will be negligible processes in our plasmas and will not be considered. Also the above equation are for the 'stage-to-stage' ionization balance and do not resolve metastables within an ion stage. The equation can easily be generalized to include metastables with the introduction of 'cross coupling' coefficients [13].

Figures 2.3 and 2.4 show the results for the ionization balance calculations of Ar, and Ne for the neutrals and the first four ion stages.
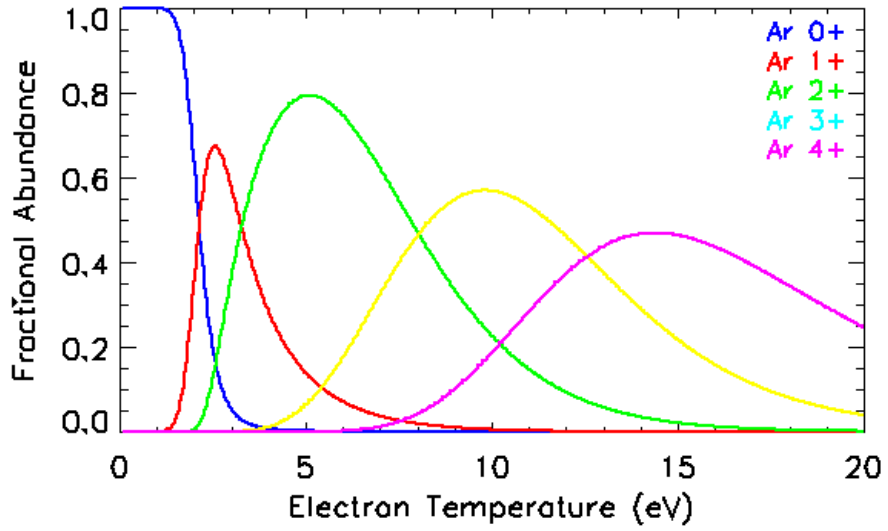
Figure 2.3: Ionization balance of Ar ($n_e = 10^{11}$ cm^{-3}).
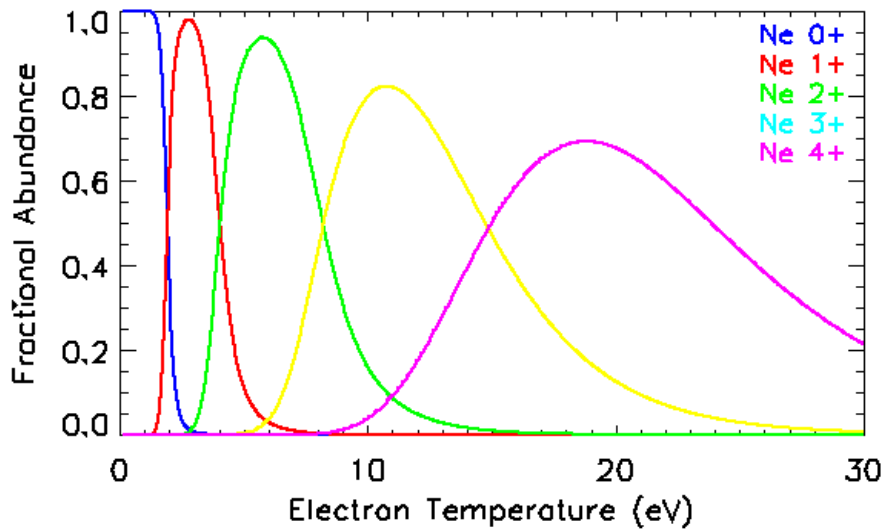
Figure 2.4: Ionization balance of Ne ($n_e = 10^{11}$ cm^{-3}).

CHAPTER 3

ATOMIC STRUCTURE DATA

3.1 Introduction

Spectroscopy studies of the light emitted (or absorbed) by atoms and ions depend upon an accurate description of the collisional processes involved. In order to compute accurate collision cross-sections for the different atomic processes, the accuracy of the atomic structure of the atom (or ion) is essential. As we saw in chapter 2.2, these processes depend upon plasma temperature, density, and plasma conditions. In order to compute high quality collision data we make use of the AUTOSTRUCTURE [2], GASP [3], and the LAMDA (see section 3.4) set of codes to compute and optimize our atomic structure that we later use to calculate the collisional atomic data we need. In this chapter we do not intend to cover the whole complexity of the atomic structure computation process, there are many text books that cover this subject extensively [16, 17]. We will focus on giving a general overview of it, and the process of optimization of the atomic structure.

3.2 Atomic Structure

For an atom with atomic number Z, and containing N electrons where $1 \le N \le Z$, and ignoring the spin-orbit interaction, the general $Hamiltonian$ operator is given by

$$H = \sum_i \left\{ -\nabla_i^2 - \frac{2(Z-N)}{r_i} + \sum_{i>j} \frac{2}{r_{ij}} \right\} \tag{3.1}$$

where $r_i = |\vec{r_i}|$ is the distance to the ith electron from the nucleus, $r_{ij} = |\vec{r_i} - \vec{r_j}|$ is the distance between the ith and j^{th} electrons, and the summation over $i > j$ is over all pairs of electrons. The distances are given in $Bohr$ units (a_o), and energies in $Rydbergs$. Plugging this $Hamiltonian$ into the time-independent $Schrödinger$ equation ($H_i \varphi_i = E_i \varphi_i$) for each individual electron we get

$$\left\{ -\frac{d^2}{dr_i^2} + \frac{l_i(l_i+1)}{r_i^2} + V(r_i) \right\} \varphi_i = E_i \varphi_i \tag{3.2}$$

where we define the effective potential $V(r_i)$ as

$$V(r_i) = \frac{2(Z-N)}{r_i} + \sum_{i>j} \frac{2}{r_{ij}} \tag{3.3}$$

and φ_i is the solution for each individual electron. As we see in equation (3.3), if we set to zero the interaction potential between electrons we reduce the problem to a simple hydrogenic model which we can solve analytically for each electron. The electron-electron interaction term means that an analytic solution is no longer possible and an exact numerical solution is still very difficult. Therefore we simplify the problem by the use of approximations.

Using the expansion of moments for the electrostatic repulsion among the electrons, we rewrite the interaction potential as

$$\frac{1}{r_{ij}} = \frac{1}{|\vec{r_i} - \vec{r_j}|} = \sum_{l=0}^{\infty} \frac{r_<^l}{r_>^{l+1}} P_l(u) \tag{3.4}$$

with u being the cosine of the angle between $\vec{r_i}$ and $\vec{r_j}$, and $r_>$, $r_<$ are the greater or the lesser of r_i and r_j. Let us now consider the monopole moment, and also assuming that all the other electrons are represented as a uniform and spherical electronic cloud of density $\rho(r)$, and radius r_o, the effective potential is given by

$$V(r_i) = \frac{-2(Z-N)}{r_i} + \int_0^{r_o} \frac{2}{r_>} \rho(r) 4\pi r^2 dr \tag{3.5}$$

This is the $Thomas - Fermi$ potential for a test charge electron at a distance r_i from the nucleus. Let us now consider the dipole and quadrupole moments, in which case the effective potential is given by

$$V(r_i) = \frac{-2(Z-N)}{r_i} + \int_0^{r_o} \rho(r_j) \left[\frac{2}{r_>} + C_1 \frac{r_<}{r_>^2} + C_2 \frac{r_<^2}{r_>^3} \right] 4\pi r_j^2 dr_j \tag{3.6}$$

where C_1 and C_2 contain the dipole and quadrupole angular terms that depend on the angular positions $\vec{r_i}$ and $\vec{r_j}$ of every pair of electrons of the atom. Under the assumption of uncorrelated single-electron wave functions these C_1 and C_2 terms are zero. However, if one allows for correlation, electrons classically tend to be at opposite sides of the nucleus due to their repulsive nature, and the C_1 and C_2 terms are finite [18].

They are referred as *electron correlation terms*. Terms beyond the monopole are small and can be treated as perturbations, thus

$$V^c(r_i) \approx V(r_i) + \frac{C_1}{r_i^2} \int_0^{r_i} \rho(r_j) r_j^3 dr_j + C_1 r_i \int_r^{r_o} \rho(r_j) dr_j$$
$$+ \frac{C_2}{r_i^3} \int_0^{r_i} \rho(r_j) r_j^4 dr_j + C_2 r_i^2 \int_{r_i}^{r_o} \frac{\rho(r_j)}{r_j} dr_j \tag{3.7}$$

This is the $Thomas - Fermi - Dirac$ potential, and by taking into account the contribution of electron exchange, the charge density includes additional terms

$$\rho(r) = \frac{1}{2\pi^2} \left\{ \frac{1}{\pi} + \left[\frac{1}{\pi^2} + V_o - V(r) \right]^{1/2} \right\}^3 \tag{3.8}$$

where

$$V_o = \frac{-15}{16\pi^2} - \frac{2(Z-N)}{r_o}$$

On the other hand, the $Thomas - Fermi - Dirac - Amaldi$ (TFDA) potential introduces variational scaling parameters (λs) to the potential of the form

$$V_{TFDA}(r_i; \lambda) = V_{TFD}(r_i/\lambda) \tag{3.9}$$

In this way, the corrected potential V^c can be computed numerically by writing $\rho(r)$ in terms of $V(r)$ by means of equation (3.8) while the electron correlation coefficients are determined variationally on the eigenenergies of the system, i.e.

$$
\begin{aligned}
V^c(r) =& V(r) + \lambda\frac{8}{3\pi}\left[\frac{1}{r^2}\int_0^r \rho(r_2)r_2^3 dr_2 + \int_r^{r_o} \rho(r_2)dr_2\right] \\
&+ \lambda\frac{8}{3\pi}\left[\frac{1}{r^2}\int_0^r \rho(r_2)r_2^4 dr_2 + r^2\int_r^{r_o} \frac{\rho(r_2)}{r_2}dr_2\right]
\end{aligned}
\tag{3.10}
$$

This potential is included in the code AUTOSTRUCTURE v.18 [2], an extension of the program SUPERSTRUCTURE [19]. In section 3.4 we employ the TFDA with scaling parameters λ_{nl} being determined variationally by a Singular Value Decomposition (SVD) method for each orbital. Having defined our effective potential V^c by equation (3.10), we now proceed to solve equation (3.2) for each individual electron by giving solutions in the form

$$
\varphi_i(\vec{r_i}) = \frac{P_{n_il_i}(r_i)}{r_i}Y_{l_i}^{m_i}(\theta_i,\phi_i)\sigma_{m_{s_i}}(S_{i_z})
\tag{3.11}
$$

where $P_{n_il_i}$ is the radial function to be computed, $Y_{l_i}^{m_i}$ are the spherical harmonics, and $\sigma_{m_{s_i}}$ is the term arising from the spin coordinates. Since the effective potential V^c varies due to the screening of the nuclear charge, we need to calculate a new potential for each different electron when calculating its wave function. We also apply the $Pauli$ exclusion principle by including the exchange of two electrons with antisymmetrized product functions.

For a given k configuration, with an N number of electrons, we get

$$\psi_k = \left(\varphi_1(\vec{r_1}), \varphi_2(\vec{r_2}), \ldots, \varphi_N(\vec{r_N})\right) \tag{3.12}$$

where

$$\left(\varphi_1(\vec{r_1}), \varphi_2(\vec{r_2}), \ldots, \varphi_N(\vec{r_N})\right) = \frac{1}{\sqrt{N!}} \begin{vmatrix} \varphi_1(\vec{r_1}) & \varphi_1(\vec{r_2}) & \cdots & \varphi_1(\vec{r_N}) \\ \varphi_2(\vec{r_1}) & \varphi_2(\vec{r_2}) & \cdots & \varphi_2(\vec{r_N}) \\ \vdots & \vdots & \ddots & \vdots \\ \varphi_N(\vec{r_1}) & \varphi_N(\vec{r_2}) & \cdots & \varphi_N(\vec{r_N}) \end{vmatrix} \tag{3.13}$$

With the properties that if $\varphi_m = \varphi_n$ then $\psi_k = 0$, and if $\vec{r_m} = \vec{r_n}$ then $\psi_k = 0$. For a certain configuration k we get

$$\psi_k = \frac{1}{\sqrt{N!}} \sum_p (-1)^p \varphi_1(\vec{r_{j1}}) \varphi_2(\vec{r_{j2}}), \ldots, \varphi_N(\vec{r_{jN}}) \tag{3.14}$$

with p being the number of permutations that the electrons can take in the specific configuration k. We now take the problem of determining the quantitative form of the radial factors $P_{n_i l_i}(r_i)$ appearing in equation (3.11). By plugging equation (3.11) into equation (3.2) we get

$$\left\{ -\frac{d^2}{dr_i^2} + \frac{l_i(l_i + 1)}{r_i^2} + V^c(r_i) \right\} P_{n_i l_i}(r_i) = E_{il} P_{n_i l_i}(r_i) \tag{3.15}$$

These equations may be solved by numerical or analytic methods. In the numerical case the radial equations are treated as a set of coupled integro-differential equations in which the radial-wave functions $P_{n_i l_i}(r_i)$ are variables. Because the radial wave functions must obey the boundary conditions $P_{n_i l_i}(0) = 0$, and $\lim\limits_{r \to \infty} P_{n_i l_i}(r) = 0$. A solution can thus be obtained numerically by integrating to self-consistency and the boundary conditions satisfied. In the analytic case the radial functions are expressed in an analytic form. The standard approach is to express each radial-wave function in terms of normalized radial basis functions called $Slater$-type orbitals [17]

$$P_{n_i l_i}(r) = \sum_j b_{ij} \frac{(2\xi_{ij})^{l_{ij}+1/2}}{\sqrt{(2l_{ij})!}} r^{l_{ij}} e^{-\xi_{ij} r} \tag{3.16}$$

Also in order to fine tune our structure as in the case of the TFDA potential, we could also include scale factors λs in order to shift the radial position of the orbitals

$$P_{n_i l_i}(r) = \sum_j b_{ij} \frac{(2\xi_{ij})^{l_{ij}+1/2}}{\sqrt{(2l_{ij})!}} (\lambda r)^{l_{ij}} e^{-\xi_{ij}(\lambda r)} \tag{3.17}$$

The AUTOSTRUCTURE code also includes the option of $Slater$-type orbitals with scaling parameters.
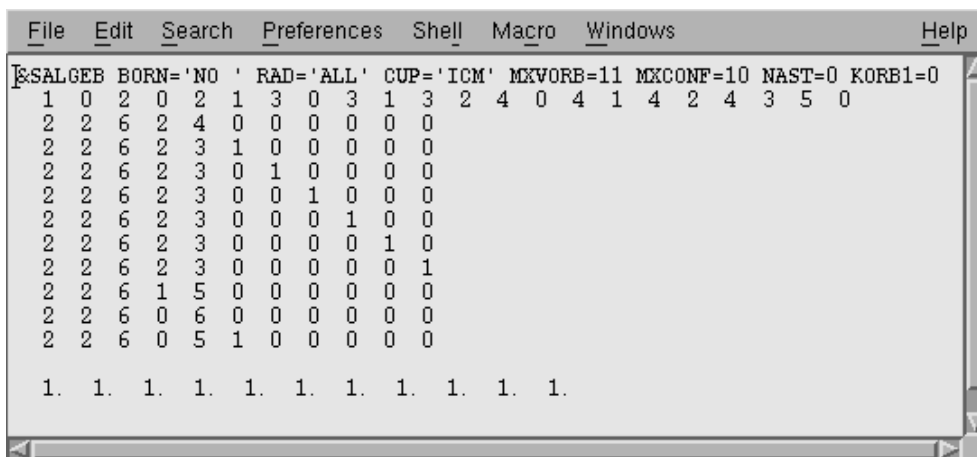
3.3 Atomic Structure Codes

3.3.1 AUTOSTRUCTURE

AUTOSTRUCTURE [2] is a general program for the calculation of atomic and ionic energy levels, radiative and autoionization rates, and photoionization cross-sections in (LS), or intermediate coupling using non-relativistic (IC, LS) or semi-relativistic (ICM, MVD) wavefunctions. It is in effect a superset of the code SUPERSTRUCTURE [19] on which it was initially based. The nuclear charge and the level of accuracy desired determines whether (IC), (LS), (ICM), or (MVD) coupling should be used. The configurations to be chosen include those for which data is wanted, plus (optionally) additional configurations to improve the accuracy of the structure by including the Configuration Interaction (CI). This defines a unique angular algebra problem. The CI expansion is related closely to the choice of radial functions. The better the choice of radial functions, the smaller the CI expansion required to obtain a given level of accuracy, which in turn leads to a smaller computational problem. Each nl radial function is calculated in a model potential $Thomas - Fermi - Dirac - Amaldi$ (TFDA) or $Slater$-Type-Orbital (STO). Both include optional scaling parameters to fine tune the atomic structure. These scaling parameters can be optimized automatically by minimizing a weighted sum of term energies chosen by the user. The (IC), (LS), (ICM), or (MVD) $Hamiltonian$ is diagonalized to obtain eigenenergies and eigenvectors with which to construct the transition rates. AUTOSTRUCTURE has also the capability to calculate collision strengths Ω_{ij}s by using the Plane Wave $Born$ approximation (see chapter 4.2).

3.3.2 GASP

GASP (Graphical AutoStructure Package) [3] is a java front end to the atomic structure package AUTOSTRUCTURE [2], developed under the Rollins College Student-Faculty Collaborative Scholarship Research program (Loria, Blossey, Ballance and Griffin). The purpose of this program is to offer a graphical user interface to run the AUTOSTRUCTURE code. As an example, we have chosen the input file for the computation of the structure of the case of the Ar^{2+} ion. The typical input file (das file) for the AUTOSTRUCTURE code requires the list of the orbitals as well as each configuration, the advantage of GASP is that it generates the configurations automatically by promoting the electrons in the different specified sub-shells. The typical AUTOSTRUCTURE input file for a case of the Ar^{2+} ion is shown in figure 3.1

```
File   Edit   Search   Preferences   Shell   Macro   Windows                    Help

&SALGEB BORN='NO ' RAD='ALL' CUP='ICM' MXVORB=11 MXCONF=10 NAST=0 KORB1=0
   1  0  2  0  2  1  3  0  3  1  3  2  4  0  4  1  4  2  4  3  5  0
   2  2  6  2  4  0  0  0  0  0  0
   2  2  6  2  3  1  0  0  0  0  0
   2  2  6  2  3  0  1  0  0  0  0
   2  2  6  2  3  0  0  1  0  0  0
   2  2  6  2  3  0  0  0  1  0  0
   2  2  6  2  3  0  0  0  0  1  0
   2  2  6  2  3  0  0  0  0  0  1
   2  2  6  1  5  0  0  0  0  0  0
   2  2  6  0  6  0  0  0  0  0  0
   2  2  6  0  5  1  0  0  0  0  0

   1.  1.  1.  1.  1.  1.  1.  1.  1.  1.  1.
```

Figure 3.1: AUTOSTRUCTURE input file for a case of the Ar^{2+} ion.

As we can see from figure 3.1, we need to have knowledge of the different input parameters that we specify for the calculation. We show in figure 3.2 the graphical interface of GASP to compute the same case shown in figure 3.2.
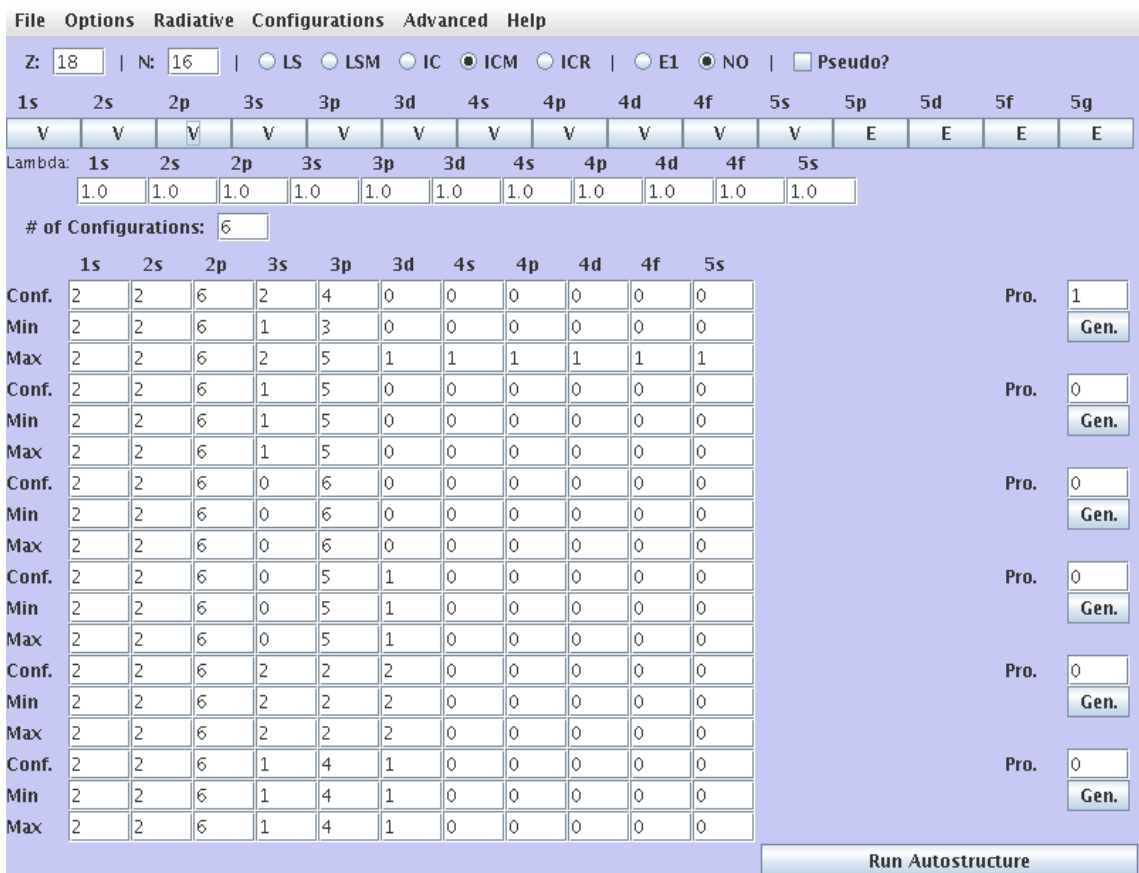
Figure 3.2: GASP interface showing a computation for a case of the Ar^{2+} ion.

3.4 Atomic Structure Optimization

3.4.1 Introduction

Cross-section computations as well as radiative and autoionization rates, oscillator strengths, energy levels, photoionization cross-sections, and many other important atomic quantities depend on the basic foundation of a good atomic structure. Accurate collisional-radiative modeling depends on such atomic quantities and plays a key role in the development of diagnostics used in fusion as well as astrophysical plasmas. There are many challenges arising when trying to calculate good atomic structure, especially when it comes to near neutral systems. The collision calculations can grow very large as we include more and more configurations in our system, this is particularly true for R-Matrix calculations. Several codes for atomic structure have been developed over the years [20]. We are working with the AUTOSTRUCTURE [2, 3] code to generate radial files that will be used for collision cross-section calculations using the R-Matrix codes [21]. A lot of time and effort is spend in the optimization task of the orbitals in AUTOSTRUCTURE by varying the scale factors (see section 3.2). This process is quite challenging since it requires experience in atomic structure calculation to know which orbitals are to be varied. It could be a lengthy and tedious process. To get an idea whether our structure is good or not we compute energy levels and line strengths, and then we compare them to those available in accurate data sources such as the ones found in the NIST tables [22]. Our aim is to provide an automatic way to compute the optimal structure by linearizing the dependence of the energy levels Ei, and line strengths Sij to the scale factors (λs), and from there to solve the inverse of the normalized $Jacobian$ matrix by using Singular Value Decomposition (SVD) [4] to get the optimal scale factors that we need.

3.4.2 Linearization of the Model

Linearization methods are widely used in many fields of physics [23]. We are using the same concepts to optimize our atomic structure. In order to monitor and compare the quality of our atomic structure we make use of the NIST atomic database. The selected quantities we use are the NIST energies (levels or terms) Ei_{nist}, and either the line strengths Sij_{nist}, the oscillator strengths fij_{nist}, or $Einstein$'s Ajk_{nist} coefficients. In our modeling we will use line strengths instead of oscillator strengths due to their independence to the energy of the transitions. Since both the energies and line strengths depend upon the scale factors (λs), we linearize both and approximate the relation between the NIST quantities and our modeled values as $E_{nist} \approx E_{model}(\lambda) + \frac{\partial E}{\partial \lambda} \delta \lambda$, and $S_{nist} \approx S_{model}(\lambda) + \frac{\partial S}{\partial \lambda} \delta \lambda$. We rearrange these equations as

$$\Delta E = E_{nist} - E_{model}(\lambda) \approx \frac{\partial E}{\partial \lambda} \delta \lambda \tag{3.18}$$

$$\Delta S = S_{nist} - S_{model}(\lambda) \approx \frac{\partial S}{\partial \lambda} \delta \lambda \tag{3.19}$$

In order to be able to include both of these different quantities in our optimization, we normalize both of them by their respective NIST values, therefore

$$\frac{\Delta E}{E_{nist}} \approx \frac{1}{E_{nist}} \frac{\partial E}{\partial \lambda} \delta \lambda \tag{3.20}$$

$$\frac{\Delta S}{S_{nist}} \approx \frac{1}{S_{nist}} \frac{\partial S}{\partial \lambda} \delta \lambda \tag{3.21}$$

This way we rewrite our complete model for any n number of energies, any m number of line strengths, and any l number of scale factors as

$$
\begin{pmatrix}
\frac{\Delta E_1}{E_{nist1}} \\
\frac{\Delta E_2}{E_{nist2}} \\
\vdots \\
\frac{\Delta E_n}{E_{nistn}} \\
\frac{\Delta S_1}{S_{nist1}} \\
\frac{\Delta S_2}{S_{nist2}} \\
\vdots \\
\frac{\Delta S_m}{S_{nistm}}
\end{pmatrix}
\approx
\begin{pmatrix}
\frac{1}{E_{nist1}}\frac{\partial E_1}{\partial \lambda_1} & \frac{1}{E_{nist1}}\frac{\partial E_1}{\partial \lambda_2} & \cdots & \frac{1}{E_{nist1}}\frac{\partial E_1}{\partial \lambda_l} \\
\frac{1}{E_{nist2}}\frac{\partial E_2}{\partial \lambda_1} & \frac{1}{E_{nist2}}\frac{\partial E_2}{\partial \lambda_2} & \cdots & \frac{1}{E_{nist2}}\frac{\partial E_2}{\partial \lambda_l} \\
\vdots & \vdots & \ddots & \vdots \\
\frac{1}{E_{nistn}}\frac{\partial E_n}{\partial \lambda_1} & \frac{1}{E_{nistn}}\frac{\partial E_n}{\partial \lambda_2} & \cdots & \frac{1}{E_{nistn}}\frac{\partial E_n}{\partial \lambda_l} \\
\frac{1}{S_{nist1}}\frac{\partial S_1}{\partial \lambda_1} & \frac{1}{S_{nist1}}\frac{\partial S_1}{\partial \lambda_2} & \cdots & \frac{1}{S_{nist1}}\frac{\partial S_1}{\partial \lambda_l} \\
\frac{1}{S_{nist2}}\frac{\partial S_2}{\partial \lambda_1} & \frac{1}{S_{nist2}}\frac{\partial S_2}{\partial \lambda_2} & \cdots & \frac{1}{S_{nist2}}\frac{\partial S_2}{\partial \lambda_l} \\
\vdots & \vdots & \ddots & \vdots \\
\frac{1}{S_{nistm}}\frac{\partial S_m}{\partial \lambda_1} & \frac{1}{S_{nistm}}\frac{\partial S_m}{\partial \lambda_2} & \cdots & \frac{1}{S_{nistm}}\frac{\partial S_m}{\partial \lambda_l}
\end{pmatrix}
\cdot
\begin{pmatrix}
\delta\lambda_1 \\
\delta\lambda_2 \\
\vdots \\
\delta\lambda_l
\end{pmatrix}
\tag{3.22}
$$

We rewrite the model in vector notation as $\mathbf{\Delta P} \approx \mathbf{M} \cdot \boldsymbol{\delta\lambda}$. Where we have defined $\mathbf{\Delta P}$ as the normalized vector for the difference of quantities, $\mathbf{M}$ as the normalized $\boldsymbol{Jacobian}$ matrix, and $\boldsymbol{\delta\lambda}$ as the correction scale factors vector. We write the solution of the vector of the correction of the scale factors as

$$
\begin{pmatrix}
\delta\lambda_1 \\
\delta\lambda_2 \\
\vdots \\
\delta\lambda_l
\end{pmatrix}
\approx
\begin{pmatrix}
\frac{1}{E_{nist1}}\frac{\partial E_1}{\partial \lambda_1} & \frac{1}{E_{nist1}}\frac{\partial E_1}{\partial \lambda_2} & \cdots & \frac{1}{E_{nist1}}\frac{\partial E_1}{\partial \lambda_l} \\
\frac{1}{E_{nist2}}\frac{\partial E_2}{\partial \lambda_1} & \frac{1}{E_{nist2}}\frac{\partial E_2}{\partial \lambda_2} & \cdots & \frac{1}{E_{nist2}}\frac{\partial E_2}{\partial \lambda_l} \\
\vdots & \vdots & \ddots & \vdots \\
\frac{1}{E_{nistn}}\frac{\partial E_n}{\partial \lambda_1} & \frac{1}{E_{nistn}}\frac{\partial E_n}{\partial \lambda_2} & \cdots & \frac{1}{E_{nistn}}\frac{\partial E_n}{\partial \lambda_l} \\
\frac{1}{S_{nist1}}\frac{\partial S_1}{\partial \lambda_1} & \frac{1}{S_{nist1}}\frac{\partial S_1}{\partial \lambda_2} & \cdots & \frac{1}{S_{nist1}}\frac{\partial S_1}{\partial \lambda_l} \\
\frac{1}{S_{nist2}}\frac{\partial S_2}{\partial \lambda_1} & \frac{1}{S_{nist2}}\frac{\partial S_2}{\partial \lambda_2} & \cdots & \frac{1}{S_{nist2}}\frac{\partial S_2}{\partial \lambda_l} \\
\vdots & \vdots & \ddots & \vdots \\
\frac{1}{S_{nistm}}\frac{\partial S_m}{\partial \lambda_1} & \frac{1}{S_{nistm}}\frac{\partial S_m}{\partial \lambda_2} & \cdots & \frac{1}{S_{nistm}}\frac{\partial S_m}{\partial \lambda_l}
\end{pmatrix}^{-1}
\cdot
\begin{pmatrix}
\frac{\Delta E_1}{E_{nist1}} \\
\frac{\Delta E_2}{E_{nist2}} \\
\vdots \\
\frac{\Delta E_n}{E_{nistn}} \\
\frac{\Delta S_1}{S_{nist1}} \\
\frac{\Delta S_2}{S_{nist2}} \\
\vdots \\
\frac{\Delta S_m}{S_{nistm}}
\end{pmatrix}
\tag{3.23}
$$

Or also rewritten as $\delta\lambda \approx M^{-1} \cdot \Delta P$. Having the correction for the scale factors, we use them to obtain the new scale factors $\lambda_{new} = \lambda_{old} + \delta\lambda$. With these new scale factors we recompute our model and compare it again with the NIST quantities, and rerun the process over again. To compare the success of our optimization process, we compare the initial and final values for the least square χ^2, which is given by $\chi^2 = \Delta P_1^2 + \Delta P_2^2 + \ldots + \Delta P_{N+M}^2$.

3.4.3 Inverse Matrix Computation

One of the problems we face in trying to compute the inverse of the normalized $(n+m) \times l$ $Jacobian$ matrix M, is that may not be square $(n+m) \neq l$, and we also run the risk that it may be singular. To overcome these problems we get the closest solution of the inverse by decomposing the matrix using Singular Value Decomposition [4], therefore we can express the matrix M as

$$M = U \cdot S \cdot V^T \tag{3.24}$$

where U is a $(n+m) \times (n+m)$ unitary matrix, S is a $(n+m) \times l$ diagonal matrix with non-negative real numbers on the diagonal, and V^T denotes the conjugate transpose of V which is a $l \times l$ unitary matrix. These matrices have the following properties

- The columns of V form a set of orthonormal "input" or "analyzing" basis vector directions for M.

- The columns of U form a set orthonormal "output" basis vector directions for M.

- The matrix S contains the singular values, which can be thought of as scalar "gain controls" by which each corresponding input is multiplied to give a corresponding output.

Since our aim is to minimize the least square χ^2, we can do this successfully by computing the "inverse" or the pseudo-inverse of the matrix which is defined as

$$\mathbf{M}^{-1} \approx \mathbf{V} \cdot \mathbf{S}^{-1} \cdot \mathbf{U}^{\mathbf{T}} \tag{3.25}$$

The matrix $\mathbf{S}$ is a diagonal matrix which contains K singular values. The number of singular values determines the rank of the matrix, and the singular values are ordered in descendent form $S_1 > S_2 > \ldots > S_K$

$$\mathbf{S} = \begin{pmatrix} S_1 & 0 & 0 & \ldots & 0 & 0 & \ldots & 0 \\ 0 & S_2 & 0 & \ldots & 0 & 0 & \ldots & 0 \\ \vdots & \vdots & \vdots & \ddots & \vdots & \vdots & \vdots & \vdots \\ 0 & 0 & 0 & \ldots & S_K & 0 & \ldots & 0 \\ 0 & 0 & 0 & \ldots & 0 & 0 & \ldots & 0 \\ \vdots & \vdots & \vdots & \ddots & \vdots & \vdots & \vdots & \vdots \\ 0 & 0 & 0 & \ldots & 0 & 0 & \ldots & 0 \end{pmatrix} \tag{3.26}$$

The K rank of the matrix represents the number of "dimensions". The difficulty is to select the P number of singular values that we need to compute this pseudo-inverse where $P \leq K$. Since we need to compute the vector of the scale factor corrections $\delta\lambda$, we choose to apply some physical restrictions. In order not to affect the different atomic orbitals by too much while we optimize others, we choose a range of values for the total scale factors, in our case this range is

$$0.8 \leq \lambda_{new} = \lambda_{old} + \delta\lambda \leq 1.2 \tag{3.27}$$

With this restriction in place we select the P number of singular values to compute the singular values inverse matrix $\mathbf{S}^{-1}$

$$\mathbf{S}^{-1} = \begin{pmatrix} \frac{1}{S_1} & 0 & 0 & \ldots & 0 & 0 & \ldots & 0 \\ 0 & \frac{1}{S_2} & 0 & \ldots & 0 & 0 & \ldots & 0 \\ \vdots & \vdots & \vdots & \ddots & \vdots & \vdots & \vdots & \vdots \\ 0 & 0 & 0 & \ldots & \frac{1}{S_P} & 0 & \ldots & 0 \\ 0 & 0 & 0 & \ldots & 0 & 0 & \ldots & 0 \\ \vdots & \vdots & \vdots & \ddots & \vdots & \vdots & \vdots & \vdots \\ 0 & 0 & 0 & \ldots & 0 & 0 & \ldots & 0 \end{pmatrix} \qquad (3.28)$$

There is not a specific method to know how many P singular values we need to use to compute the inverse of the singular values matrix. Therefore we use trial and error until we meet condition (3.27). In case condition (3.27) is not met, then we have to use a different strategy, namely multiply the $\boldsymbol{Jacobian}$ matrix by a certain factor greater than one and then compute the corrections again. If condition (3.27) still goes unmet, then again we multiply the $\boldsymbol{Jacobian}$ matrix by a greater factor and compute the optimization again. The reason why we multiply the $\boldsymbol{Jacobian}$ matrix by a factor is to increase the value of its derivatives, by increasing these values we reduce the size of the corrections for the scale factors $\boldsymbol{\delta\lambda}$, in order to meet the condition (3.27). We demonstrate this process better in figure 3.3.
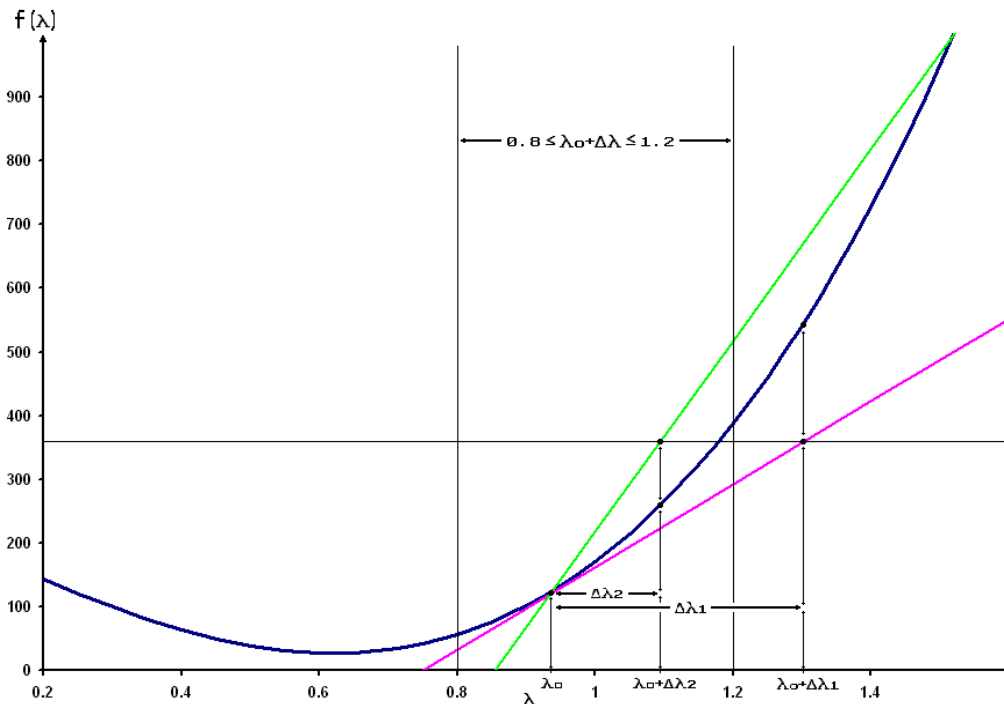
Figure 3.3: Representation of the variation of the orbitals with respect to the scale factors λs.

As we see in figure 3.3, the function $f(\lambda)$ may represent any of the atomic orbitals that depend on the scale factor λ, and the "$Jacobian$" value or derivative is represented by the value of the slope of the purple line. If we compute the correction $\Delta\lambda_1$ by using the value of the "real" derivative, we would violate condition (3.27), and as shown in the figure we would end up out of the set boundaries. Therefore, if we multiply the value of the derivative by a factor greater than one, we get the new increased value for the slope in this example represented by the green line. By using this new value of the derivative to compute the new correction $\Delta\lambda_2$, we now satisfy condition (3.27), and our new value for λ is now within the set boundaries.

3.4.4 Results

As an example of the optimization process, we have chosen the Ar^{2+} ion, in which we have used eleven orbitals and ten configurations. These configurations are

- $1s^2 2s^2 2p^6 3s^2 3p^4$ (Ground)

- $1s^2 2s^2 2p^6 3s^2 3p^3 3d$

- $1s^2 2s^2 2p^6 3s^2 3p^3 4s$

- $1s^2 2s^2 2p^6 3s^2 3p^3 4p$

- $1s^2 2s^2 2p^6 3s^2 3p^3 4d$

- $1s^2 2s^2 2p^6 3s^2 3p^3 4f$

- $1s^2 2s^2 2p^6 3s^2 3p^3 5s$

- $1s^2 2s^2 2p^6 3s 3p^5$

- $1s^2 2s^2 2p^6 3p^6$

- $1s^2 2s^2 2p^6 3p^5 3d^1$

Therefore, we have eleven scaling factors λs, one for each of the eleven orbitals 1s, 2s, 2p, 3s, 3p, 3d, 4s, 4p, 4d, 4f, and 5s. The initial values for all the λs is set to one, and the boundaries are set to satisfy the condition given by equation (3.27). The program will read two input files corresponding to the ASCII tables from the NIST energy values, and the NIST $Einstein$'s A_{jk} coefficients. The LAMDA code has the option of transforming these coefficients into line strengths S_{jk} and then run the optimization.

Results of the optimization process for the first iteration are presented in figure 3.4.

```
                                                    lamdaout
     Start of program

  niter =  8  ne = 116  nLT = 17  nlevtrm =  185  nlamda = 11  coupling = IC

   *********** Iteration #  1 ************

   Lamda#    Chi Sqr        % diff

     0     1.665210E+01     100.000000
     1     1.664435E+01      99.953436
     2     1.635237E+01      98.200024
     3     1.639650E+01      98.465032
     4     1.603977E+01      96.322770
     5     1.534574E+01      92.154968
     6     1.771968E+01     106.411047
     7     1.667738E+01     100.151772
     8     1.503951E+01      90.315952
     9     9.878634E+00      59.323640
    10     1.665229E+01     100.001137
    11     1.647207E+01      98.918845
   All     7.531238E+00      45.226947

   All     7.531238E+00      45.226947

   Desired Energy  Initial Energy  %Diff   Final Energy   %Diff      Configuration  Term  J

     0.010134880    0.009702380    4.2674   0.010460940    3.2172         3s2.3p4   3P   1
     0.014308980    0.013764940    3.8021   0.014782500    3.3093         3s2.3p4   3P   0
     0.127668550    0.143280550   12.2285   0.150642800   17.9952         3s2.3p4   1D   2
     0.303139580    0.289737970    4.4209   0.287903880    5.0260         3s2.3p4   1S   0
     1.037026090    1.281568470   23.5811   1.044756870    0.7455          3s.3p5   3P*  2
     1.046110450    1.289585060   23.2743   1.053922940    0.7468          3s.3p5   3P*  1
     1.050946080    1.293739270   23.1023   1.058699810    0.7378          3s.3p5   3P*  0
     1.312427970    1.592261850   21.3218   1.353075850    3.0972          3s.3p5   1P*  1
     1.320293530    1.645442700   24.6270   1.371171750    3.8536   3s2.3p3.(4S*).3d  5D*  1
     1.320341040    1.645602240   24.6346   1.371404880    3.8675   3s2.3p3.(4S*).3d  5D*  2
     1.320403350    1.645842570   24.6470   1.371760020    3.8895   3s2.3p3.(4S*).3d  5D*  3
     1.320528670    1.646179180   24.6606   1.372262810    3.9177   3s2.3p3.(4S*).3d  5D*  4
     1.429919410    1.770260660   23.8014   1.507884940    5.4524   3s2.3p3.(4S*).3d  3D*  3
     1.430960930    1.771072600   23.7681   1.508837420    5.4423   3s2.3p3.(4S*).3d  3D*  1
     1.474885020    1.839525430   24.7233   1.583385380    7.3565   3s2.3p3.(2D*).3d  1S*  0
     1.483153580    1.818277070   22.5953   1.558261390    5.0641   3s2.3p3.(2D*).3d  3F*  2
     1.486059290    1.821072990   22.5438   1.561636190    5.0857   3s2.3p3.(2D*).3d  3F*  3
     1.489712130    1.824562290   22.4775   1.565852530    5.1111   3s2.3p3.(2D*).3d  3F*  4

   Type Desired Sjk %Err Sjk Initial Sjk  % Diff  Final Sjk   % Diff Init. Conf.   Final Conf. Termi   Termf Ji     Jf

    E2   3.467E-10   25.00   4.598E-10  32.6317  4.289E-10  23.7348   3s2.3p4 --> 3s2.3p4    3P --> 3P   0 --> 2
    M1   3.336E-05   10.00   3.323E-05   0.3778  3.322E-05   0.4033   3s2.3p4 --> 3s2.3p4    3P --> 3P   1 --> 2
    M1   2.665E-05    3.00   2.654E-05   0.4131  2.652E-05   0.4571   3s2.3p4 --> 3s2.3p4    3P --> 3P   0 --> 1

   Lamda Values

  1.000719086989  1.010407688264  1.114058671166  1.073524697425  1.072823633702  1.052246571156
  1.093407275170  0.953711089497  1.108445718000  0.999957551797  0.998566605423

                                                     Page 1
```

Figure 3.4: LAMDA code output file for the Ar^{2+} ion.

The program starts by running the AUTOSTRUCTURE code for all the scale factors λs set up to one (or to any set of initial values). AUTOSTRUCTURE generates output files that give us the computed energy for each level (or term), and the line strengths. From there we compare our results with those values found in the NIST files, and compute the least square χ^2.

This value for the χ^2, is the one we use as a reference point for comparison (100%), and its value is displayed on the first row of the first iteration of the program as shown in figure 3.4. From that point on, the program starts computing corrections by using the SVD method for each individual orbital, and recomputing the energies and line strengths by rerunning the AUTOSTRUCTURE code. Then the code computes corrections for all the orbitals at once and chooses the correction values that give the minimum χ^2. In the case of Ar^{2+}, we see that the best χ^2 value was given by including all the orbitals variations at once. The code then displays the results of the energy optimizations by displaying the "Desired Energy" (NIST Energies), and the energy values before and after the optimization with their respective % differences from those given by NIST. The code does the same for the line strengths by displaying the type of transition; Electric Dipole (E1), Electric Quadrupole (E2), Magnetic Dipole (M1), and Magnetic Quadrupole (M2). It shows also the "Desired Value" and its respective % error from those given by NIST. The initial and final computed values before and after the optimization are then shown in the next rows, which also give the % differences compared from those in NIST. Finally the code prints out the values of the optimized scale factors λs which we can use to compute our optimal structure.

CHAPTER 4

ATOMIC COLLISION DATA

4.1 Introduction

The accuracy of collision cross-section calculations play a key role in collisional-radiative modeling. Our collisional-radiative model can only be as good as the underlying atomic data we use. Many methods and approximations have been developed to solve the problem of scattering of an electron by an atom or ion. In this chapter we give a general overview of some of the most widely use methods. We begin in section 4.2 with an explanation of the Plane Wave $Born$ approximation, where we model the incoming electron by a plane wave and the target as a potential. Plane Wave $Born$ atomic data will be used for some of our neon modeling in chapter 8. In section 4.3 we will outline Distorted Wave theory in which we allow the incoming wave to be affected by the potential and therefore distorted. Distorted Wave data for electron-impact ionization cross-sections is used for argon in chapter 6. Finally we introduce R-Matrix theory in section 4.5, and also an extension of this method called R-Matrix with Pseudo-States (RMPS), which is used to describe electron scattering in the intermediate energy range above the ionization limit. Section 4.5 gives a quick overview on $Maxwellian$ effective collision strengths calculations.

In scattering problems there are perturbative methods such as the Plane Wave $Born$ and Distorted Wave. These methods are good for highly charged systems, but for near neutral systems the R-Matrix and RMPS methods in particular, result in more accurate cross-sections. R-Matrix and RMPS data for Ar^+ excitation is used in chapter 6. In chapter 7 we will present the results of a R-Matrix calculation for Ar^{2+} excitation, and in chapter 8 we use R-Matrix and RMPS data for emission of modeling from neutral neon.

4.2 Plane Wave *Born*

4.2.1 Classical Scattering Theory
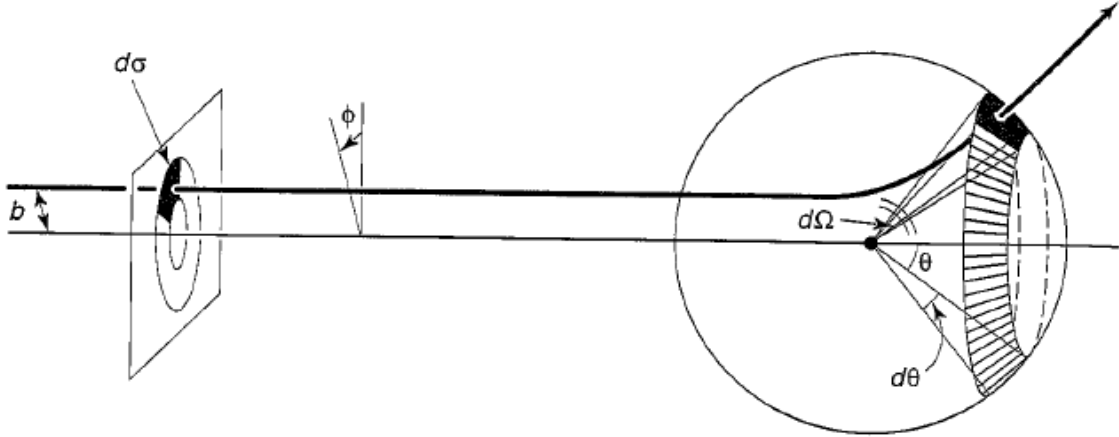
Figure 4.1: Scattering of a light particle by a heavy ion.

In terms of classical scattering theory, having a light particle incident on some heavy nucleus with an incoming energy E, and impact parameter b, the light particle will emerge at some scattered angle θ as shown by figure 4.1. By assuming for simplicity that the potential is azimuthally symmetric (no dependence in ϕ) therefore we constrain the problem to a single plane. The problem in scattering theory is reduced to determining the scattering angle θ, from the knowledge of the impact parameter b, and the energy of the incident particle E. In general, having a particle incident within an infinitesimal cross-sectional area $d\sigma$, will scatter into a corresponding infinitesimal solid angle $d\Omega$. The larger $d\sigma$ is, the bigger $d\Omega$ becomes. The proportionality factor will be called D, which represents the differential scattering cross-section $D = \frac{d\sigma}{d\Omega}$. In terms of the impact parameter b and the azimuthal angle ϕ, $d\sigma = b\,db\,d\phi$ and $d\Omega = sin(\theta)d\theta d\phi$,

therefore

$$D(\theta) = \frac{b}{sin(\theta)}\left|\frac{db}{d\theta}\right| \qquad (4.1)$$

By obtaining the differential cross-section $D(\theta)$, as a function of the angle θ, we can compute the total cross-section by integrating the differential cross-section with respect to the solid angle $d\Omega$.

$$\sigma = \int D(\theta)d\Omega \qquad (4.2)$$

4.2.2 Plane Wave Scattering
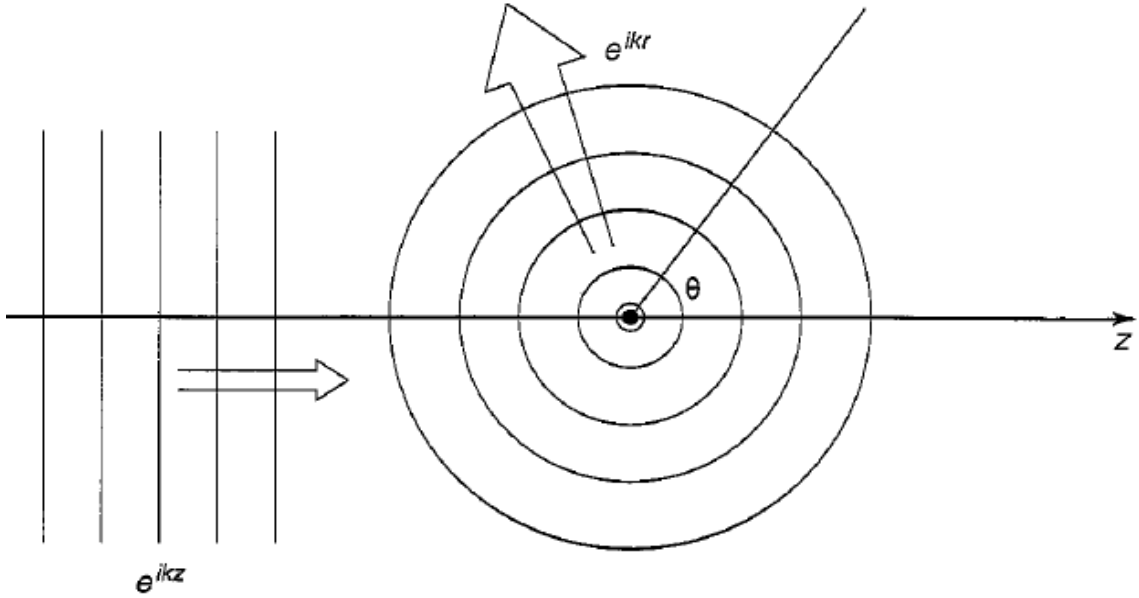
Figure 4.2: Scattering of an incident plane wave.

In this case we model the incident "light" particle as a plane wave $\psi(z) = Ae^{ikz}$, traveling in the z direction. When the plane wave interacts with the potential described by the target, it will produce an outgoing spherical wave as shown in figure 4.2. Therefore for values of r far away from the target we expect solutions to the $Schr\ddot{o}dinger$ equation in the general form

$$\psi(r,\theta) \approx A\left\{e^{ikz} + f(\theta)\frac{e^{ikr}}{r}\right\} \tag{4.3}$$

The spherical wave carries a factor of $1/r$ because $|\psi|^2$ must go like $1/r^2$ to conserve probability. The wave number k is defined in the usual way

$$k = \frac{\sqrt{2mE}}{\hbar} \tag{4.4}$$

43

It can be shown [24, 25] that the differential cross-section $D(\theta)$ is related to the scattering amplitude $f(\theta)$ by

$$D(\theta) = \frac{d\sigma}{d\Omega} = |f(\theta)|^2 \tag{4.5}$$

Therefore the whole problem of determining the cross-section is related to finding the scattering amplitude $f(\theta)$. We can see from equation (4.5) that the differential cross-section (which is the quantity of interest to the experimentalist) is given by the absolute square of the scattering amplitude.

4.2.3 The *Born* Approximation

The time-independent *Schrödinger* equation for a given potential V is given by

$$-\frac{\hbar}{2m}\vec{\nabla}^2\psi + V\psi = E\psi \tag{4.6}$$

which can be rewritten in the form

$$(\vec{\nabla}^2 + k^2)\psi = Q \tag{4.7}$$

where k and $Q(\psi)$ are defined by

$$k = \frac{\sqrt{2mE}}{\hbar} \quad and \quad Q = \frac{2m}{\hbar^2}V\psi \tag{4.8}$$

As we can see, equation (4.7) has the form of the non-homogeneous $Helmholtz$ equation. We seek a solution by using $Green$'s functions to find a solution in the integral form

$$\psi(\vec{r}) = \int G(\vec{r} - \vec{r}_o)Q(\vec{r}_o)d^3\vec{r}_o \tag{4.9}$$

as shown in appendix A, the final solution of the $Green$'s function is given by

$$G(\vec{r}) = -\frac{e^{ik\vec{r}}}{4\pi r} \tag{4.10}$$

by inserting this solution back into equation (4.9) we get

$$\psi(\vec{r}) = \psi_o(\vec{r}) - \frac{m}{2\pi\hbar^2}\int \frac{e^{ik|\vec{r}-\vec{r}_o|}}{|\vec{r}-\vec{r}_o|}V(\vec{r}_o)\psi(\vec{r}_o)d^3\vec{r}_o \tag{4.11}$$

where ψ_o satisfies the free-particle $Schr\ddot{o}dinger$ equation

$$(\vec{\nabla}^2 + k^2)\psi_o = 0 \tag{4.12}$$

Now, for the first $Born$ approximation, let us suppose that $V(\vec{r}_o)$ is localized at $\vec{r}_o = 0$, and that the potential drops to zero outside some finite region. We are interested in calculating $\psi(\vec{r})$ at points far away from the scattering center. Then $|\vec{r}| \gg |\vec{r}_o|$ for all points that contribute to the integral equation (4.11) we approximate

$$|\vec{r} - \vec{r}_o|^2 = r^2 + r_o^2 - 2\vec{r}\cdot\vec{r}_o \approx r^2\left(1 - 2\frac{\vec{r}\cdot\vec{r}_o}{r^2}\right) \tag{4.13}$$

45

therefore

$$|\vec{r} - \vec{r}_o| \approx r - \hat{r} \cdot \vec{r}_o \tag{4.14}$$

Let $\vec{k} = k\hat{r}$, and keeping the lowest order for the denominator we can approximate $|\vec{r} - \vec{r}_o| \approx r$, so we get

$$\frac{e^{ik|\vec{r} - \vec{r}_o|}}{|\vec{r} - \vec{r}_o|} \approx \frac{e^{ikr}}{r} e^{-i\vec{k} \cdot \vec{r}_o} \tag{4.15}$$

For the scattering problem we approximate the incident particle to a plane wave, therefore for an incident plane wave traveling on the z axis we have

$$\psi_o(\vec{r}) = Ae^{ikz} \tag{4.16}$$

So, by inserting in the large r approximation and the incident plane wave into equation (4.11) we get

$$\psi(\vec{r}) \approx Ae^{ikz} - \frac{m}{2\pi\hbar^2} \frac{e^{ikr}}{r} \int e^{-i\vec{k} \cdot \vec{r}_o} V(\vec{r}_o)\psi(\vec{r}_o) d^3\vec{r}_o \tag{4.17}$$

Which is in the same form of equation (4.3). From it we recognize the scattering amplitude

$$f(\theta, \phi) = -\frac{m}{2\pi\hbar^2 A} \int e^{-i\vec{k} \cdot \vec{r}_o} V(\vec{r}_o)\psi(\vec{r}_o) d^3\vec{r}_o \tag{4.18}$$

We now apply the $Born$ approximation, we suppose the incoming plane wave is not modified by the potential, therefore we approximate

$$\psi(\vec{r}_o) \approx \psi_o(\vec{r}_o) = Ae^{ikz_o} = Ae^{i\vec{k'}\cdot\vec{r}_o} \qquad (4.19)$$

where $\vec{k'} = k\hat{z}$, this wave function would be exact if the potential $V = 0$ which is the $Born$ approximation. Plugging this wavefunction inside the integral equation (4.18) we get

$$f(\theta, \phi) \approx -\frac{m}{2\pi\hbar^2} \int e^{i(\vec{k'}-\vec{k})\cdot\vec{r}_o} V(\vec{r}_o)d^3\vec{r}_o \qquad (4.20)$$

where $\vec{k}$ and $\vec{k'}$ have the same magnitude. Notice that the first $Born$ approximation is just the $Fourier$ transform of the potential $V(\vec{r}_o)$. Since $\vec{k'} = k\hat{z}$ for the incident wave, and $\vec{k} = k\hat{r}$ for the scattered wave therefore $\hbar(\vec{k} - \vec{k'})$ is the momentum transferred in the process. From this point we can get the differential cross-section D by means of equation (4.5), and our total cross-section from equation (4.2). In particular for low energy scattering (long wavelength) $(\vec{k} - \vec{k'}) \approx 0$ therefore we get

$$f(\theta, \phi) \approx -\frac{m}{2\pi\hbar^2} \int V(\vec{r})d^3\vec{r} \qquad (4.21)$$

Let us now consider a collision of an electron with a hydrogen atom initially at ground state. Again, the electron is being considered a light particle by assuming the nucleus to have infinite mass thus, neglecting the motion of the proton in the collision. The wave equation for the system of incident electron and hydrogen atom is given by

$$\left[\frac{\hbar^2}{2m}(\nabla_1^2 + \nabla_2^2) + E + \frac{e^2}{r_1} + \frac{e^2}{r_2} - \frac{e^2}{r_{12}}\right]\Psi(\vec{r}_1, \vec{r}_2) = 0 \qquad (4.22)$$

where the subscript **1** is used for the incident electron and **2** for the atomic electron. The total classical energy of the system is given by the sum of the kinetic energy of the incident electron plus the energy of the atomic electron in the ground state (E_0)

$$E = \frac{1}{2}mv^2 + E_0 \qquad (4.23)$$

We might guess a solution for equation (4.22) as

$$\Psi(\vec{r}_1, \vec{r}_2) = \psi_n(\vec{r}_2)F_n(\vec{r}_1) \qquad (4.24)$$

The functions $\psi_n(\vec{r}_2)$ are the solutions for the hydrogen atom, which satisfy the equation

$$\left(\frac{\hbar^2}{2m}\nabla_2^2 + E_n + \frac{e^2}{r_2}\right)\psi_n(\vec{r}_2) = 0 \qquad (4.25)$$

48

Substituting equation (4.24) into equation (4.22) and using the solution given by equation (4.25) we get

$$
\left(\frac{\hbar^2}{2m} \nabla_1^2 + E + \frac{e^2}{r_1} - \frac{e^2}{r_{12}} \right) \psi_n(\vec{r}_2) F_n(\vec{r}_1) + \left(\frac{\hbar^2}{2m} \nabla_2^2 + \frac{e^2}{r_2} \right) \psi_n(\vec{r}_2) F_n(\vec{r}_1) = 0
$$
$$
\left(\frac{\hbar^2}{2m} \nabla_1^2 + E + \frac{e^2}{r_1} - \frac{e^2}{r_{12}} \right) \psi_n(\vec{r}_2) F_n(\vec{r}_1) - E_n \psi_n(\vec{r}_2) F_n(\vec{r}_1) = 0
$$
$$
\left(\frac{\hbar^2}{2m} \nabla_1^2 + E - E_n \right) \psi_n(\vec{r}_2) F_n(\vec{r}_1) = \left(\frac{e^2}{r_{12}} - \frac{e^2}{r_1} \right) \psi_n(\vec{r}_2) F_n(\vec{r}_1)
$$

$$(4.26)$$

The hydrogenic wave functions form an orthonormal set

$$
\int \psi_n^*(\vec{r}_2) \psi_{n'}(\vec{r}_2) d\vec{r}_2 = \delta_{nn'}
$$

$$(4.27)$$

By multiplying equation (4.26) by $\psi_n^*(\vec{r}_2)$, and integrating with respect to $d\vec{r}_2$ we get

$$
\left(\frac{\hbar^2}{2m} \nabla_1^2 + E - E_n \right) F_n(\vec{r}_1) = \int \left(\frac{e^2}{r_{12}} - \frac{e^2}{r_1} \right) \Psi(\vec{r}_1, \vec{r}_2) \psi_n^*(\vec{r}_2) d\vec{r}_2
$$

$$(4.28)$$

In the case of $r_1 \rightarrow \infty$ the right hand vanishes, and F_n satisfies the wave equation

$$
\left(\nabla_1^2 + \frac{2m}{\hbar^2} (E - E_n) \right) F_n(\vec{r}_1) = 0
$$

$$(4.29)$$

49

which is the wave equation for a free particle with energy $E - E_n$. Here we are making the assumption that the incident electron has enough energy to excite the nth state of the atom or $E > E_n$. Let $k_n^2 = \frac{2m(E-E_n)}{\hbar^2}$, therefore

$$(\nabla_1^2 + k_n^2)F_n(\vec{r}_1) = 0 \tag{4.30}$$

and its solution must have the asymptotic form given by equation (4.3). Since we are only interested in high energy impact, the perturbation of the incident particle by the interaction with the atom is small. Applying the first order $Born$ approximation to $F(\vec{r}_1)$ as a plane wave for $\Psi(\vec{r}_1, \vec{r}_2)$ we get

$$\Psi(\vec{r}_1, \vec{r}_2) = e^{i\vec{k}\cdot\vec{r}_1}\psi(\vec{r}_2) \tag{4.31}$$

Substituting this solution into equation (4.30) we obtain

$$(\nabla_1^2 + k_n^2)F_n(\vec{r}_1) = \frac{2m}{\hbar^2}\int\left(\frac{e^2}{r_{12}} - \frac{e^2}{r_1}\right)e^{i\vec{k}\cdot\vec{r}_1}\psi(\vec{r}_2)\psi_n^*(\vec{r}_2)d\vec{r}_2 \tag{4.32}$$

which is in the same form of equation (4.7) and has an integral solution given by equation (4.9). The $Green$'s function is given by equation (4.6), therefore we get

$$F_n(\vec{r}) = \frac{m}{2\pi\hbar^2}\int\int\frac{e^{ik_n|\vec{r}-\vec{r}_1|}}{|\vec{r}-\vec{r}_1|}e^{i\vec{k}\cdot\vec{r}_1}\left(\frac{e^2}{r_1} - \frac{e^2}{r_{12}}\right)\psi(\vec{r}_2)\psi_n^*(\vec{r}_2)d\vec{r}_1 d\vec{r}_2 \tag{4.33}$$

50

Approximating by using equation (4.15) we obtain

$$F_n(\vec{r}) \approx \frac{m}{2\pi\hbar^2} \frac{e^{ikr}}{r} \int \int e^{i(\vec{k}-\vec{k}_n)\cdot\vec{r}_1} \left(\frac{e^2}{r_1} - \frac{e^2}{r_{12}} \right) \psi(\vec{r}_2)\psi_n^*(\vec{r}_2) d\vec{r}_1 d\vec{r}_2 \qquad (4.34)$$

By comparing this result with equation (4.3) we recognize that the scattering amplitude $f_n(\theta)$ is given by

$$f_n(\theta) = \frac{m}{2\pi\hbar^2} \int \int e^{i(\vec{k}-\vec{k}_n)\cdot\vec{r}_1} \left(\frac{e^2}{r_1} - \frac{e^2}{r_{12}} \right) \psi(\vec{r}_2)\psi_n^*(\vec{r}_2) d\vec{r}_1 d\vec{r}_2 \qquad (4.35)$$

and therefore by the definition given by equation (4.5), we obtain the differential cross-section

$$D_n(\theta) = \frac{k_n}{k} \frac{m^2}{4\pi^2\hbar^4} \left| \int \int e^{i(\vec{k}-\vec{k}_n)\cdot\vec{r}_1} \left(\frac{e^2}{r_1} - \frac{e^2}{r_{12}} \right) \psi(\vec{r}_2)\psi_n^*(\vec{r}_2) d\vec{r}_1 d\vec{r}_2 \right|^2 \qquad (4.36)$$

We notice that the interaction of an electron with a hydrogen atom is described by the potential $V(\vec{r}_1, \vec{r}_2) = \frac{e^2}{r_1} - \frac{e^2}{r_{12}}$. The differential cross-section may be written in the more compact form

$$D_n(\theta) = \frac{k_n}{k} \frac{m^2}{4\pi^2\hbar^4} |\langle \vec{k}_n n | V | \vec{k} 0 \rangle|^2 \qquad (4.37)$$

In the case of inelastic collisions, we consider the *Coulomb* collision of an electron with an atom in which, the atom is raised from the state n_i to state n_f by the impact. If E_{n_i} and E_{n_f} are the energies of the two atomic states and $\vec{k}_i$, and $\vec{k}_f$ are the initial and final momentum vectors of the colliding electron, the conservation of energy gives

$$\frac{1}{2}m(v_i^2 - v_f^2) = E_{n_f} - E_{n_i} \tag{4.38}$$

where $\vec{v} = \frac{\hbar\vec{k}}{m}$. Within the range of validity of the first *Born* approximation, the differential cross-section describing the collision is given by

$$D(\theta) = \frac{k_f}{k_i}\frac{m^2}{4\pi^2\hbar^4}|\langle\vec{k}_f n_f|V|\vec{k}_i n_i\rangle|^2 \tag{4.39}$$

where the *Coulomb* potential is given by

$$V(\vec{r}) = \frac{e^2}{|\vec{r} - \vec{R}|} \tag{4.40}$$

The expression given by equation (4.39), is the differential cross-section under the first *Born* approximation, and is useful in the case of high energy incident electrons. For high incident energy, contributions to the cross-section for a wide range of momentum become important. We will use Plain Wave *Born* electron-impact excitation for neutral neon in chapter 8.

4.3 Distorted Wave

It was shown in the previous section that the differential cross-section for scattering may be obtained from

$$D(\theta) = \frac{k_f}{k_i} \frac{m^2}{4\pi^2\hbar^4} |\langle \vec{k}_f n_f | V | \vec{k}_i n_i \rangle|^2 \tag{4.41}$$

where the potential V (for a neutral system) is given by

$$V(\vec{r}, \vec{r}_j) = \sum_{j=1}^{N} \frac{e^2}{|\vec{r}_j - \vec{r}|} \tag{4.42}$$

and describes the **Coulomb** interaction between the incident electron at position $\vec{r}$ and the target electrons at positions $\vec{r}_j$. N is the number of electrons at the target atom. We express the **Coulomb** potential in terms of the **Fourier** integral transform

$$V(\vec{r}, \vec{r}_j) = \frac{e^2}{2\pi^2} \sum_{j=1}^{N} \int \frac{e^{-i\vec{q}\cdot(\vec{r}_j - \vec{r})}}{q^2} d^3\vec{q} \tag{4.43}$$

where the integration is over all the space and we represent $\vec{q}$ in spherical coordinates (q, θ, ϕ). By letting $\vec{R}_j = \vec{r} - \vec{r}_j$, and orienting $\vec{R}_j$ along the z axis, the **Fourier** integral becomes

$$\begin{aligned}
&\frac{e^2}{2\pi^2} \int \frac{e^{-i\vec{q}\cdot(\vec{r}_j - \vec{r})}}{q^2} d^3\vec{q} \\
&= \frac{e^2}{2\pi^2} \int_0^\infty dq \int_0^\pi d\theta \int_o^{2\pi} d\phi \sin(\theta) e^{-iqR_j\cos(\theta)} \\
&= \frac{e^2}{2\pi^2} \frac{4\pi}{R_j} \int_0^\infty \frac{\sin(qR_j)}{q} dq
\end{aligned} \tag{4.44}$$

and by using the identity

$$\int_0^\infty \frac{sin(ax)}{x} dx = \frac{\pi}{2} sgn(a) \tag{4.45}$$

Therefore we get $\int_0^\infty \frac{sin(qR_j)}{q} dq = \frac{\pi}{2} sgn(R_j)$, since $\vec{R}_j = \vec{r} - \vec{r}_j > 0$, then $sgn(R_j) = 1$, and equation (4.44) becomes

$$\sum_{j=1}^N \frac{e^2}{R_j} \tag{4.46}$$

which is the **_Coulomb_** potential **_V_**. Expanding the exponential factor in the **_Fourier_** integral, the differential cross-section in equation (4.41) may be written as

$$D(\theta) = \frac{k_f}{k_i} \frac{m^2}{4\pi^2\hbar^4} \left| \frac{e^2}{2\pi^2} \int d^3\vec{q} \frac{1}{q^2} \langle \vec{k}_f | e^{-i\vec{q}\cdot\vec{r}} | \vec{k}_i \rangle \langle n_f | \sum_{j=1}^N e^{i\vec{q}\cdot\vec{r}_j} | n_i \rangle \right|^2 \tag{4.47}$$

This expression divides neatly into two factors

- The first matrix element deals only with incident electron momentum parameters which are independent of the state transition involved within the target atom.

- The second matrix element involves the atomic parameters.

54

The expansion of the matrix element in equation (4.41), into two matrix element factors in equation (4.47) is due to the fact that the solution of the $Schrödinger$ equation describing the system is a product of a function of only incident electron coordinates and a function of atomic electrons' coordinates as described at the end of section 4.2.3. We use the distorted $Coulomb$ wavefunction to calculate the first matrix element

$$\langle \vec{k}_f | e^{-i\vec{q}\cdot\vec{r}} | \vec{k}_i \rangle \tag{4.48}$$

and the second matrix element is in the form factor which is taken between the target states [26]

$$F_{if}(\vec{q}) = \langle n_f | \sum_{j=1}^{N} e^{i\vec{q}\cdot\vec{r}_j} | n_i \rangle \tag{4.49}$$

We call this method Distorted Wave Approximation (DWA). We make use of Distorted Wave electron-impact ionization data for argon in chapter 6.

4.4 *R*-Matrix Theory
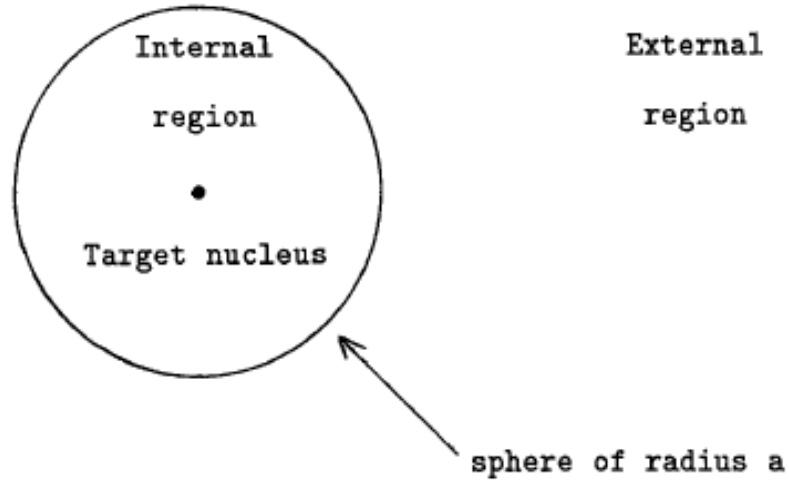
Figure 4.3: Partitioning of configuration space R-Matrix theory.

R-Matrix theory was first introduced in nuclear physics by Wigner and Eisenbud [27] in 1947 in a study of resonance reactions. In the case of electron-atom collisions, the non-perturbative R-Matrix theory partitions the configuration space into two regions named the internal region, and the external region as shown in figure 4.3. The internal region $r \leq a$, where r is the coordinate of the scattered electron relative to the target nucleus, and a is chosen to encompass the charge cloud of the atom/ion. In this region, the wavefuctions of the scattered electron and the atom or ion overlap. Therefore electron exchange and correlation between the scattered electron and the N-electron target atom or ion are important, and the $(N + 1)$-electron collision complex behaves in a similar way to a bound state.

In this chapter we do not intend to cover the whole development of R-Matrix theory, but simply to emphasize the advantages that this non-perturbative method has when calculating electron-impact excitation data, and its applications in emission modeling in plasmas. For a more comprehensive description on the R-Matrix theory refer to Burke et al. [28], or Burke and Berrington [29].

56

For the internal region $r \leq a$, the wave function for the electron-atom collision process is defined by

$$\Psi_k(x_1,\ldots,x_{N+1}) = \mathcal{A} \sum_{ij} c_{ijk}\bar{\bar{\Phi}}_i(x_1,\ldots,x_N,\hat{r}_{N+1}\sigma_{N+1})u_{ij}(\vec{r}_{N+1})$$

$$+ \sum_j d_{jk}\phi_j(x_1,\ldots,x_{N+1}) \tag{4.50}$$

where the functions $\bar{\bar{\Phi}}_i$ are formed by coupling the multi-configurational functions Φ_i. The u_{ij} are the basis orbitals for the scattered electron. The operator $\mathcal{A}$ antisymmetrizes the scattered electron coordinate with the N atomic electron coordinates. The functions ϕ_j are $(N+1)$-electron configurations formed from the atomic orbitals $P_{nl}(r)$, and are analogous to the N-electron configurations. Finally, c_{ijk} and d_{jk} are expansion coefficients determined by diagonalizing the $(N+1)$-electron $Hamilonian$. The coefficients c_{ijk} and d_{jk} in equation (4.50) are determined by diagonalizing

$$(\Psi_k|H_{N+1}|\Psi_{k'}) = E_k^{N+1}\delta_{kk'} \tag{4.51}$$

where H_{N+1} is the $(N+1)$-electron $Hamiltonian$ operator which is projected onto the space functions Ψ_k. The R-Matrix is given in the form

$$R_{ij} = \frac{1}{2a} \sum_k \frac{w_{ik}(a)w_{jk}(a)}{E_k^{N+1} - E} \tag{4.52}$$

where w_{ik} are defined as

$$w_{ik}(r) = \sum_j c_{ijk}u_{ij}(r) \tag{4.53}$$

The surface amplitudes $w_{ik}(a)$ and the poles E_k^{N+1} of the R-Matrix are obtained directly from the eigenvectors and eigenvalues of the $Hamiltonian$ matrix defined by equation (4.51). The most important source of error in this method is the truncation of the expansion in equation (4.52) to a finite number of terms.

The R-Matrix acts as an interface between the inner region and the outside region.

In the external region, $r > a$, electron exchange between the scattered electron and the target can be neglected. The scattered electron then moves in the long-range multipole coulomb potential of the target. Outside the R-Matrix box, the total wavefunction for a given (LS) symmetry is expanded in basis states given by

$$\Psi_k^{N+1} = \sum_i \psi_i^{N+1} \frac{v_i(r_{N+1})}{r_{N+1}} \tag{4.54}$$

where $v_i(r)$ are radial continuum functions obtained by solution of radial asymptotic coupled differential equations. The inner and outer solutions are matched at the edge of the R-Matrix box to extract collision strengths.

The R-Matrix method also is able to calculate electron-impact ionization data by introducing pseudo-states in our atomic structure to represent the high **Rydberg** and continuum states as shown by figure 4.4.
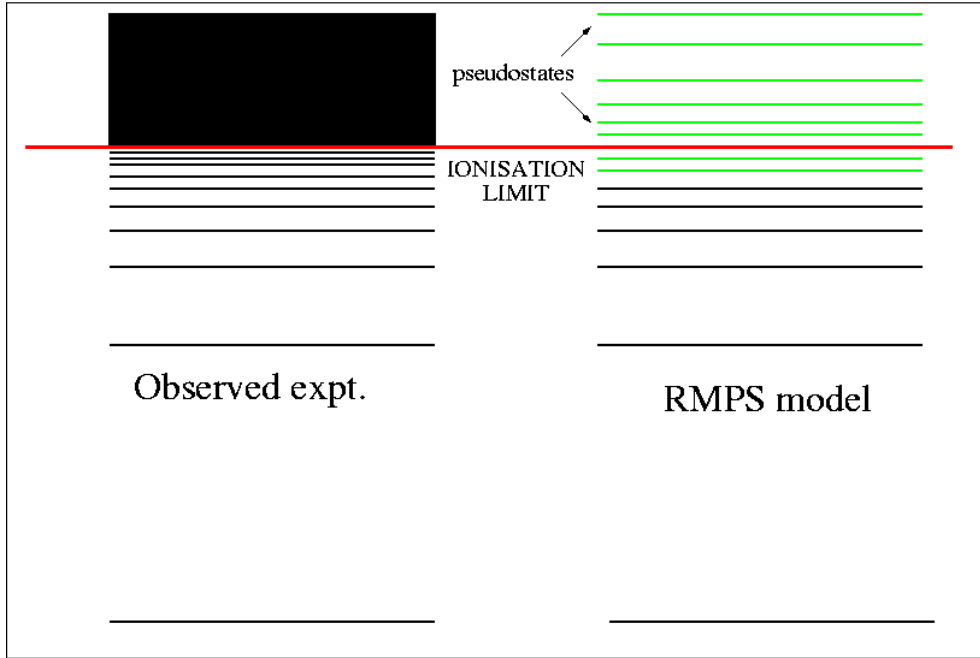
Figure 4.4: Representation of the continuum by the introduction of pseudo-states.

As we show in chapter 6 and later in chapter 8, these pseudo-states make a significant difference in the electron-impact excitation cross-sections [6] between standard R-Matrix, and R-Matrix with Pseudo-States (RMPS). These differences are due to the continuum coupling effects and also significantly improvement of our atomic structure. The advantage of R-Matrix is that it is a non-perturbative method. Its limitations are mainly computational. The accuracy of the method depends on the quality of our atomic structure and the calculation can grow significantly with the addition of configurations. This limitation is overcome by the paralellization of the method. Therefore the use of small parallel computer clusters and massively parallel supercomputers when running large calculations is essential.

We make use of R-Matrix and RMPS data for Ar$^+$ in chapter 6. In chapter 7 we present a new R-Matrix calculation for electron-impact excitation of Ar^{2+}, and in chapter 8 we use R-Matrix and RMPS excitation data for neutral neon modeling.

4.5   Effective Collision Strengths

As shown in the previous section, the calculation of accurate collision cross-section calculations play a very important role in our emission modeling in plasmas. The format in which this data is made available is also important since it has to be presented to the user in a simple and compact form. It should also be consistent with no significant error in accuracy. Electron-impact excitation cross-sections as well as electron-impact ionization cross-sections have a strong dependence with respect to the energy of the incident electron. By using suitable scaling procedures it is possible to remove the main asymptotic energy (or temperature) dependence for the given data. The energy (temperature) is also scaled so as to become a dimensionless variable which ranges from 0 at threshold energy (zero temperature) to 1 at infinite energy (temperature). In this way the whole variation of a collision strength can be exhibited in a single graph since the energy is mapped onto the interval (0,1). An introduction of the Burgess-Tully plots is also given by Burgess et al. [5].

4.5.1 Collision Strength

In the previous sections we have discussed several methods to calculate electron-impact excitation and ionization cross-sections. For example let us consider the reaction

$$X_i^{+z}(E_i) + e(\varepsilon_i) \rightarrow X_j^{+z}(E_j) + e(\varepsilon_j) \tag{4.55}$$
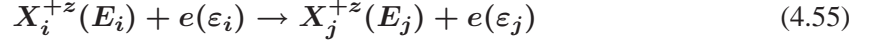
with

$$\varepsilon_i + E_i = \varepsilon_j + E_j \tag{4.56}$$

Where E_i is the energy of the initial level of the ion X^{+Z}, and E_j is the energy of the excited level. The energy of the incident (scattered) electron is given by ε_i (ε_i). The reaction is described as a cross-section as a function of the incident electron energy by $\sigma_{i \rightarrow j}(\varepsilon_i)$. By energy concepts the electron-impact excitation can only occur if the incident electron energy is $\varepsilon_i \geq \Delta E_{ij} = E_j - E_i$. It is convenient to introduce the threshold parameter $X = \varepsilon_i/\Delta E_{ij}$, with $X \in [1, \infty]$. The cross-section can therefore be expressed in terms of the incident electron energy ε_i, the scattered electron energy ε_j, or the threshold parameter X. In the literature, in preference to the cross-section $\sigma_{i \rightarrow j}(\varepsilon_i)$ it is usual to give the collision strength Ω_{ij} since is a dimension-less quantity, and is also symmetrical between the initial and final states i, j. It is also a slowly varying quantity with respect to the incident electron energy. The excitation cross-section $\sigma_{i \rightarrow j}(\varepsilon_i)$, de-excitation cross-section $\sigma_{j \rightarrow i}(\varepsilon_i)$, and collision strength Ω_{ij}, are connected by the following relations

$$\Omega_{ij} = \omega_i \frac{(\varepsilon_i - E_i)}{I_H} \frac{\sigma_{i \rightarrow j}(\varepsilon_i - E_i)}{\pi a_o^2} = \omega_j \frac{(\varepsilon_i - E_j)}{I_H} \frac{\sigma_{j \rightarrow i}(\varepsilon_i - E_j)}{\pi a_o^2} = \Omega_{ji} \tag{4.57}$$

The atomic unit of cross-section is $\pi a_o^2 = 8.7972 \times 10^{-17}$ cm^2. ω_i and ω_j are the statistical weights of the initial and final levels, and $I_H = 13.6058$ eV.

It is shown by Burgess et al. [5] that the collision strengths behave like

Type-1	Electric Dipole (ED)	$\Omega_{ij} \sim$ const. $\ln(\varepsilon_i)$
Type-2	Non-ED, No Spin Change	$\Omega_{ij} \sim$ const.
Type-3	Spin Change	$\Omega_{ij} \sim$ const. ε_i^{-2}

4.5.2 Effective Collision Strength

As seen in section 2.2, for our collisional-radiative model we make use of the electronic colli-sional excitation/de-excitation $(q_{i\rightarrow j}^e / q_{j\rightarrow i}^e)$ rate coefficients, which by assuming a $Maxwellian$ electron distribution are given by

$$q_{i\rightarrow j}^e(T_e) = 4\pi \left(\frac{m_e}{2\pi kT_e} \right)^{3/2} \int_0^\infty v_i \exp\left(-\frac{\varepsilon_i}{kT_e} \right) \sigma_{i\rightarrow j}(\varepsilon_i) v_i^2 dv_i \qquad (4.58)$$

The relation between the excitation/de-excitation rate coefficients is given by

$$q_{i\rightarrow j}^e = q_{j\rightarrow i}^e \left(\frac{\omega_j}{\omega_i} \right) \exp\left(-\frac{\Delta E_{ij}}{kT_e} \right) \qquad (4.59)$$

We now transform from v_i to ε_j, where ε_j is the colliding electron kinetic energy after excita-tion has occurred, and rewrite equation (4.58) as follows

$$q_{i\rightarrow j}^e(T_e) = 2\sqrt{\pi} \frac{a_o\hbar}{m_e\omega_i} \left(\frac{I_H}{kT_e} \right)^{1/2} \exp\left(-\frac{\Delta E_{ij}}{kT_e} \right) \Upsilon_{ij} \qquad (4.60)$$

where Υ_{ij} is the effective collision strengths which is defined as

$$\Upsilon_{ij} = \int_0^\infty \Omega_{ij} \exp\left(-\frac{\varepsilon_j}{kT_e}\right) d\left(\frac{\varepsilon_j}{kT_e}\right) \tag{4.61}$$

The advantage of using effective collision strengths over rate coefficients is that they vary very slowly with respect to electron temperature. This simplifies our need of having a lot of data stored since we only need a few points and the rest can be interpolated.

$$
\begin{aligned}
\text{Type-1} \quad & \Upsilon_{ij} \sim \text{const. } \ln(T_e) \\
\text{Type-2} \quad & \Upsilon_{ij} \sim \text{const.} \\
\text{Type-3} \quad & \Upsilon_{ij} \sim \text{const. } T_e^{-1}
\end{aligned}
$$

ADAS [11] computes effective collision strengths from our R-Matrix collision strength data via convolution with a $Maxwellian$ electron distribution. The data is stored in a default temperature grid in an adf04 file. In order to show the effective collision strengths from threshold to the infinite energy point on a single plot, we make use of the Burgess-Tully plots [5]. The transformations introduce an adjustable parameter C. Again the x is defined to be zero when $T_e = 0$, and unity when $T_e = \infty$.

These transformations are defined as

For Type 1

$$x = 1 - \frac{\ln(C)}{\ln\left(\frac{kT_e}{\Delta E_{ij}} + C\right)}$$

$$y(x) = \frac{\Upsilon_{ij}}{\ln\left(\frac{kT_e}{\Delta E_{ij}} + C\right)} \tag{4.62}$$

For Type 2

$$x = \frac{\left(\frac{kT_e}{\Delta E_{ij}}\right)}{\left(\frac{kT_e}{\Delta E_{ij}} + C\right)}$$

$$y(x) = \Upsilon_{ij} \tag{4.63}$$

For Type 3

$$x = \frac{\left(\frac{kT_e}{\Delta E_{ij}}\right)}{\left(\frac{kT_e}{\Delta E_{ij}} + C\right)}$$

$$y(x) = \left(\frac{kT_e}{\Delta E_{ij}} + 1\right)\Upsilon_{ij} \tag{4.64}$$

5.1 Introduction

The **A**uburn **S**teady s**T**ate **R**esearch f**A**ci**L**ity ASTRAL is a helicon device that can generate intense Ar and Ne plasma columns. It has also been used with He and CO_2. ASTRAL Ar and Ne typical plasma parameters are

- $N_e = 10^{11}$ - 10^{13} cm^{-3}

- $T_e = 2$ - 15 eV

- $B_{field} = 200$ - 1300 Gauss

- RF$_{power} \lesssim 2$ kWatt

The helicon plasma source is a very efficient method for generating high density plasmas using radio waves. Helicon sources can be very useful for basic plasma studies because there is no large electric current running through the plasma that can disturb the phenomenon we are trying to study, and also the antenna is outside the plasma, thus avoiding further contamination to the plasma and damage to the antenna by sputtering.

Figure 5.1: The ASTRAL helicon plasma source.

Figure 5.1 shows the ASTRAL laboratory. In the ASTRAL experiment at Auburn University we carry on experiments with a main focus on measurements of spectral-line emission of plasmas at different conditions. We measure plasma densities and temperatures with the use of two RF compensated $Langmuir$ probes. These measurements form the benchmark in which we compare our collisional-radiative model in order to generate reliable non-invasive methods for plasma diagnostic based on spectral emission.

ASTRAL generates intense Ar (see figure 5.2), and Ne (see figure 5.3) plasmas.
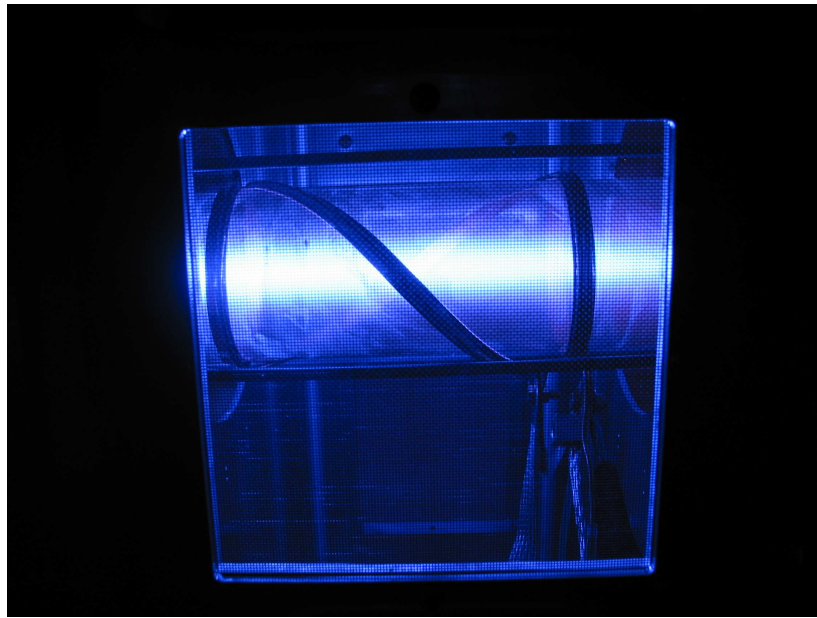
Figure 5.2: Ar plasma in ASTRAL (Blue core with purple edge).
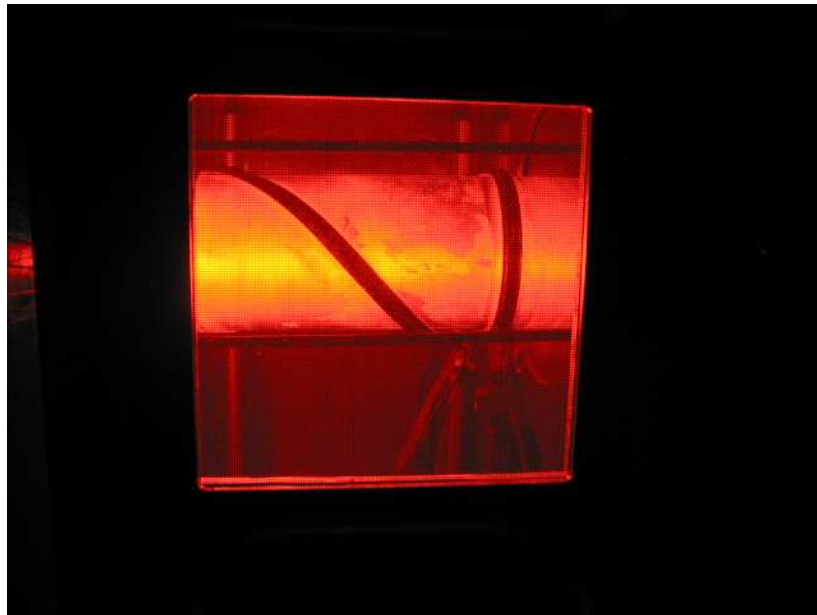
Figure 5.3: Ne plasma in ASTRAL (Yellow core with red/orange edge).

5.2 Experimental Setup
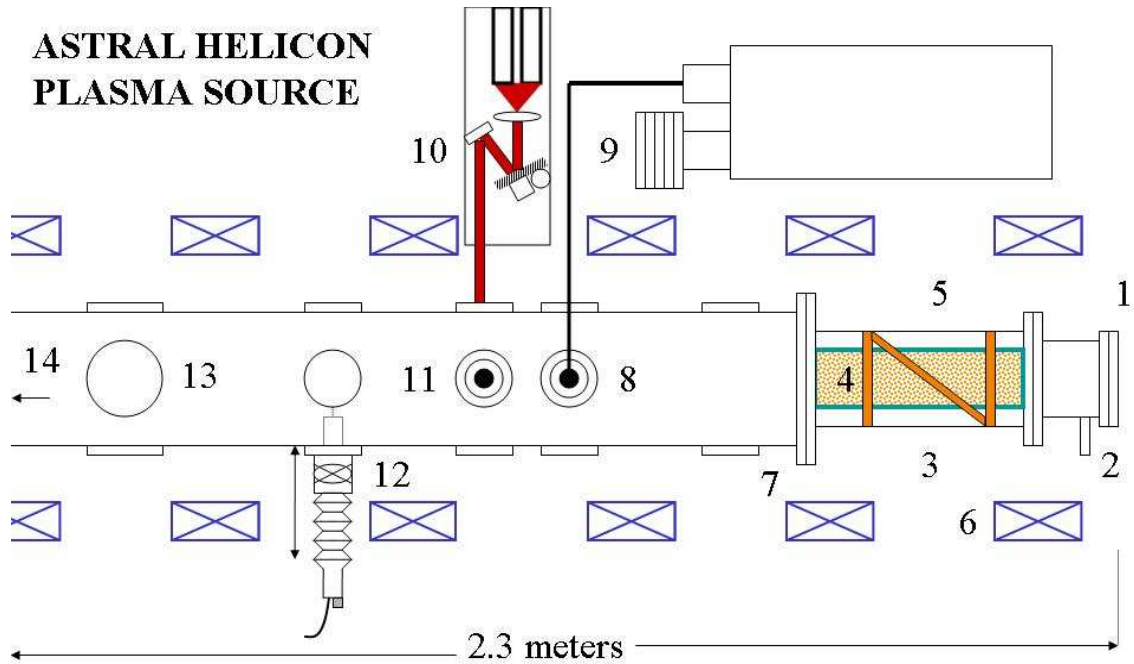
Figure 5.4: Schematic upper view of the ASTRAL helicon plasma source (not to scale).

Figure 5.4 shows the ASTRAL experimental setup, where 1. End viewport, 2. Gas Inlet, 3. Glass section (Vacuum Chamber), 4. Plasma column, 5. Fractional helix antenna, 6. Magnetic field coils, 7. SS section (Vacuum Chamber), 8. Light collection optics (LIF and spectrometer), 9. Spectrometer (Monochromator and CCD camera), 10. Diode Laser LIF system, 11. Top viewport, 12. Retractable RF compensated *Langmuir* Probe, 13. Large viewport, 14. Toward the pumping station.

ASTRAL is a 2.5 m long helicon plasma source divided by a 0.6 m long glass section, which has the water cooled helix copper antenna wrapped around to couple RF radiation into the plasma, and a metal section with ports distributed along its length for diagnostics. The vacuum system consists of a turbo-molecular drag pump with a pumping speed of 400 l/s. The base pressure in the system is 5.0×10^{-8} Torr. We introduce gas into the vacuum chamber by means of two flow controllers mounted in a flange at one of the ends of the device. These flow controllers also allow us to experiment with controlled gas mixtures. The operating gas pressure ranges from 0.5 to 50.0 mTorr. The steady-state axial magnetic field ranges from 0 to 1300 Gauss, and is generated by seven magnetic coils. The power amplifier can supply up to 2 kW of RF power to the plasma and is coupled to the antenna through a capacitance matching circuit. The RF signal is provided by a function generator with a 3 to 30 MHz frequency range. We have chosen to tune up the RF frequency to 11.5 MHz since the RF power amplifier obtains a good performance around that frequency. The plasma parameters of density and temperature can be changed by varying the RF power, gas pressure, magnetic field intensity, and RF frequency. ASTRAL counts with a number of diagnostics. These computerized diagnostics include: Optical Emission Spectroscopy, two radially scanning RF compensated $Langmuir$ Probes, and a Laser Induced Fluorescence diagnostic. In this chapter we will focus in the spectrometer system and the $Langmuir$ probes.

5.3 *Langmuir* **Probe Settings**

RF compensated Langmuir Probe with manual linear motion

1) Vacuum chamber, 2) Plasma, 3) Probe tip (W), 4) Compresed Bellows, 5) Cross, 6) 6" linear motion, 7) BNC electrical feedthrough, 8) Keithley 2400 Sourcemeter, 9) GPIB card, 10) Computer, 11) Dummy tip, 12) Capacitor (5 nF), 13) Ceramic cover, 14) 5 inductors ($10\,\mu H < L < 270\,\mu H$).
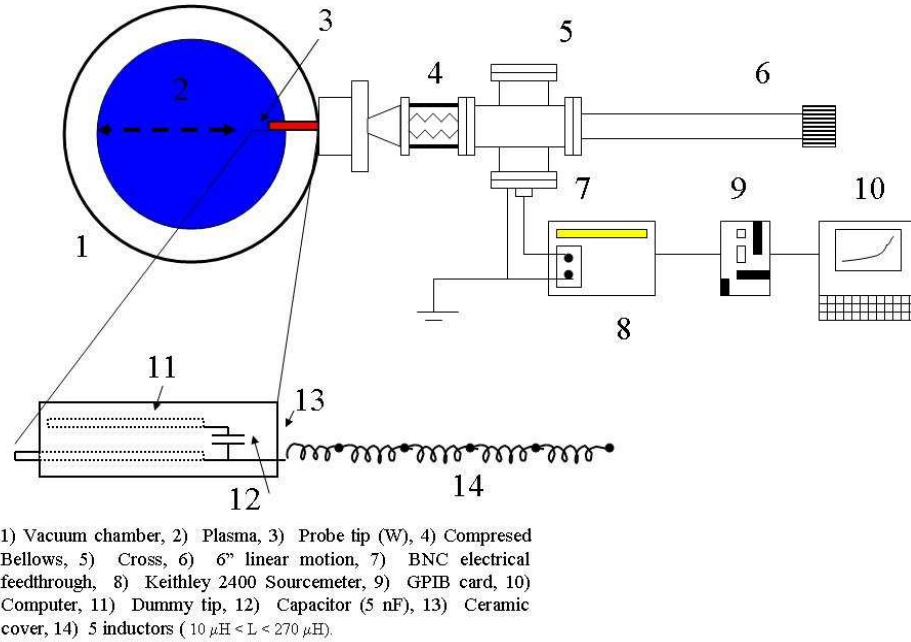
Figure 5.5: *Langmuir* probe settings in ASTRAL.

Figure 5.5 shows the schematic diagram of the two RF compensated *Langmuir* probes as setup in ASTRAL. Each of the probes consists on two tips. A tip that is exposed to the plasma to perform the measurements, and a dummy tip that is used for RF compensation inside of the ceramic cover. Each one of them also includes a manual linear motion system to adjust the position of the probes. This motion capability enable us to make measurements of temperatures and densities at different locations along the inner diameter of the vacuum chamber. This help us to map the temperature and density profiles which, as we will show in chapter 6, are necessary for a successful spectral emission modeling.

Figure 5.6 shows a picture of the *Langmuir* probe inside the vacuum chamber (small tip at 3:00 o'clock) during an Ar plasma run.
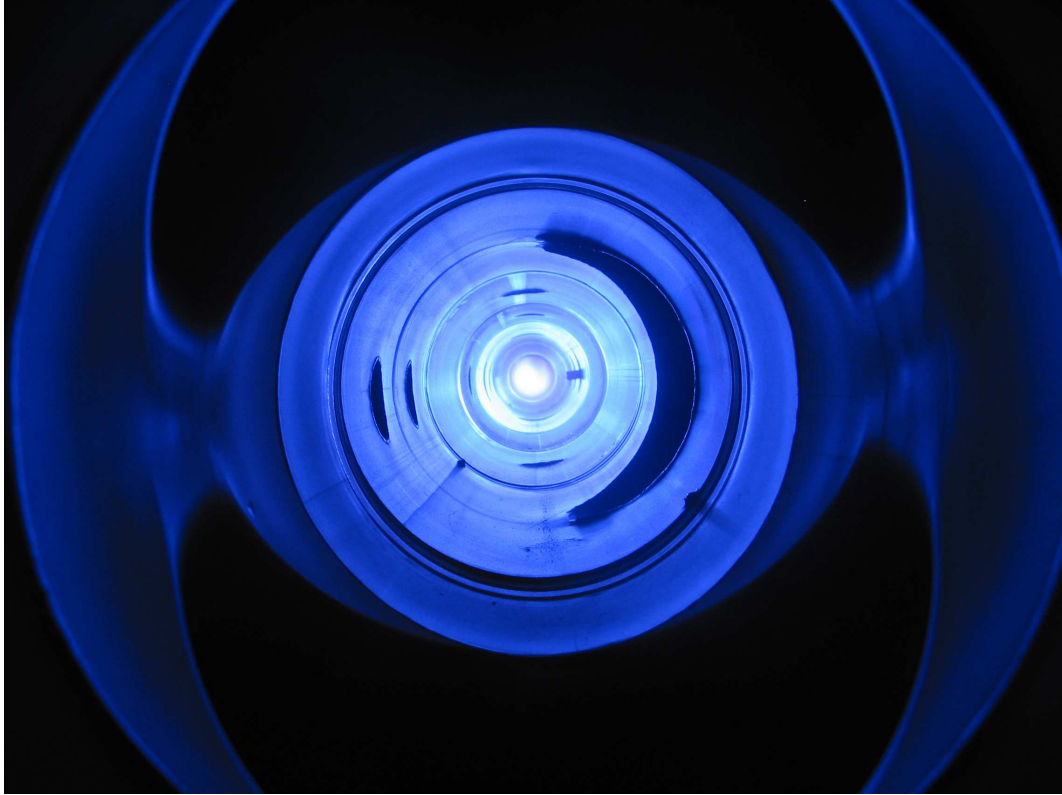
Figure 5.6: *Langmuir* probe inside of ASTRAL (Ar plasma run).

Of all the different plasma diagnostics, the *Langmuir* probe is probably the simplest, since it consists of sticking a wire into the plasma and measuring the current to it at various applied voltages. However, it is an intrusive method which could affect our plasma conditions to a certain extent. The probe tip must be carefully designed to not interfere much with the plasma, nor to be destroyed by it. For this reason we use tungsten in order to withstand the heat and to reduce sputtering created by the ion collisions against the material. The interpretation of the current-voltage curves could be difficult. In this section we give a basic overview of the *Langmuir* probe theory applied to plasma diagnostics.

The *Langmuir* probe is inserted into the plasma and biased with a voltage V, and the current I is then measured as a function of the biased voltage. When the measured current in the probe goes to zero at a certain value of the potential, we name it the floating potential V_f. Typically the floating potential has a negative value (see figure 5.7) caused by the differences between the mobility of electrons and ions. Let the plasma potential be V_p, when $V > V_p$, an electron current I_e is collected, and the probe current is negative. When $V \gg V_p$ we then reach the electron saturation current value I_{es}. When $V < V_p$, and ion current I_i is collected, and the probe current is positive. When $V \ll V_p$ we then reach the ion saturation current I_{is}. It is customary to plot I vs V curves with I_{es} positive and I_{is} negative. Figure 5.7 shows such plot.
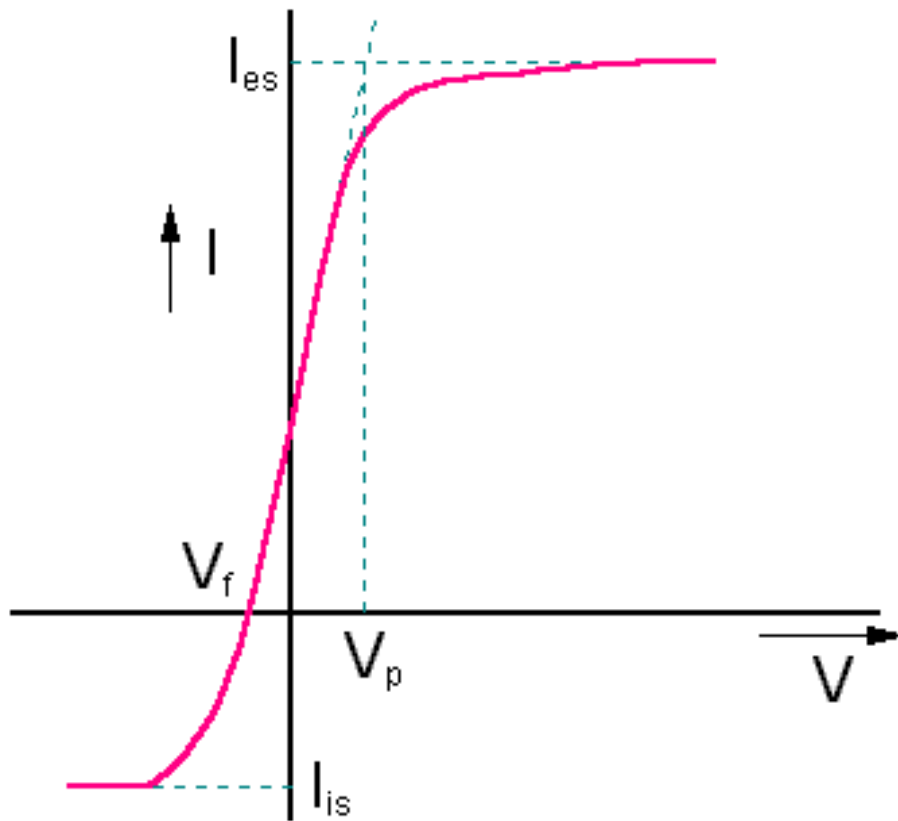
Figure 5.7: Typical I vs V plot in a *Langmuir* probe.

As shown in figure 5.7, at the far left where all the electrons have been repelled we have the ion-saturation current I_{is}, this is the region where the probe is most exposed to ion bombardment. In order to minimize sputtering damage into the probe we make use of a tungsten tip, this will increase the lifetime of the probe and also will reduce the amount of contaminants introduced into the plasma caused by sputtering. The floating potential V_f is where the ions and electron currents are equal and the net current is zero. When we introduce a highly positive voltage all the ions are repelled and we get the electron saturation current I_{es}. This region is very dangerous to the probe since even though we use a tip made of tungsten, these high currents could melt the already hot probe exposed to the plasma. In the transition region, the ion current is negligible and the electrons are partially repelled by the negative potential $V - V_p$. When V reaches V_p all the random flux of electrons is collected. From the I vs V curve, the electron density n_e, electron temperature T_e, and plasma potential V_p can be determined [30]. The exponential part of the I vs V curve, when plotted semi-logarithmically it should be a straight line if the electrons are $Maxwellian$ [30]

$$I_e = I_{es} \exp[e(V - V_p)/KT_e] \tag{5.1}$$

where

$$I_{es} = en_e A_p \frac{\bar{v}}{4} = en_e A_p \left(\frac{KT_e}{2\pi m_e} \right)^{1/2} \tag{5.2}$$

A_p is the exposed area of the probe tip. Here I_{es} is the electron-saturation current, or random thermal current to a surface at V_p. Equation (5.1) shows the slope of $\ln I$ vs V curve is exactly $1/KT_e$ and is a good measure of the electron temperature.

As long as the electrons are $Maxwellian$, the electron energy distribution function (EEDF) at a potential $V < 0$ is proportional to

$$f(v) \propto e^{-(1/2mv^2 + eV)/KT_e} = e^{-e|V|/KT_e} e^{-(mv^2/2KT_e)} \tag{5.3}$$

We see that $f(v)$ is still $Maxwellian$ at the same T_e, only the density is decreased by $\exp(-e|V|/KT_e)$. Thus, the slope of the semi-log curve is independent of the probe area or shape, and independent of collisions, since these merely preserve the $Maxwellian$ distribution. By assuming a $Maxwellian$ distribution of the plasma [31], the current in the probe for the transition region is given by

$$I(V) = n_{e\infty} e A_p \left(\frac{KT_e}{m_i} \right)^{1/2} \left[\left(\frac{m_i}{2\pi m_e} \right)^{1/2} \exp \left(\frac{eV}{KT_e} \right) - \frac{A_s}{A_p} \exp \left(-\frac{1}{2} \right) \right] \tag{5.4}$$

where V is the applied voltage, $n_{e\infty}$ is the electron density far away from the probe (which we want to determine), e is the electron charge, T_e is the electron temperature (which we also want to determine), A_p is the surface area of the probe, and A_s is the area of the sheath formed around the probe. The sheath is formed by ions that $Debye$ shield the potential applied to the plasma, and it is usually a few $Debye$ lengths tick. Since we can measure the slope of the experimental I vs V curve (see figure 5.7), we can linearize equation (5.4) by using $\exp(x) \approx 1 + x$ which is valid for $V_f \lesssim V \lesssim V_p$. Therefore we get

$$I(V) \approx n_{e\infty} e A_p \left(\frac{KT_e}{m_i} \right)^{1/2} \left\{ \left(\frac{m_i}{2\pi m_e} \right)^{1/2} \left[1 + \frac{eV}{KT_e} \right] - \frac{A_s}{A_p} \exp \left(-\frac{1}{2} \right) \right\} \tag{5.5}$$

by using equation (5.2) we rewrite equation (5.5) in its final linear form

$$I(V) \approx I_{es}\left(\frac{e}{KT_e}\right)V + I_{es}\left[1 - \left(\frac{m_i}{2\pi m_e}\right)^{-1/2}\frac{A_s}{A_p}\exp\left(-\frac{1}{2}\right)\right] \qquad (5.6)$$

With this linearization we can identify the value of the slope of the line, therefore by making it equal to our experimental value obtained from the V vs I plot (see figure 5.7) we get

$$\frac{dI(V)}{dV} \approx \frac{eI_{es}}{KT_e} \qquad (5.7)$$

By solving equation (5.7) we can now obtain the electron temperature which is given by

$$T_e \approx \frac{eI_{es}}{K\left(\frac{dI}{dV}\right)} \qquad (5.8)$$

As we can see the temperature is obtained by the experimental measurements of the slope of the V vs I curve in the linear region, and the electron saturation current I_{es}. Even though this method seems to be simple, it presents some practical problems. As we pointed out early, the electron saturation current is typically higher than the ion saturation current I_{is} [32]. Since the helicon device generates dense plasmas we run the risk of reducing the lifetime or destroying the probe by exposing it to higher currents and melting it. Therefore we use another approach [31] to obtain the electron temperature by measuring the ion saturation current I_{is}, instead of the electron saturation current I_{es}, since the tip can handle better the ion bombardment than the high electron current.

The approach given by Hutchinson [31], consists in using the derivative of the current with respect to the voltage which is given by

$$\frac{dI}{dV} = \frac{e}{KT_e}(I - I_{is}) + \frac{dI_{is}}{dV} \tag{5.9}$$

where

$$I_{is} = 0.61 e n_{e\infty} A_p \left(\frac{KT_e}{m_i}\right)^{1/2} \tag{5.10}$$

and dI_{is}/dV has arise from dA_s/dV [31]. By getting the experimental measurements from the V vs I plot for the ion saturation current I_{is} in a region where $dI_{is}/dV \approx 0$ we get

$$T_e \approx \frac{e(I - I_{is})}{K\left(\frac{dI}{dV}\right)} \tag{5.11}$$

Having found the value for the electron temperature T_e, we now use equation (5.10) to solve for the electron density n_e. Therefore we get

$$n_e = \frac{I_{is}}{0.61 e A_p}\left(\frac{KT_e}{m_i}\right)^{-1/2} \tag{5.12}$$

As we can see, the success of the determination of the electron temperatures and densities by $Langmuir$ probe measurements rely on the measurement of the slope in the linear region that we have undertaken. In order for this approximation to be valid we have assumed that the velocity distribution of the electrons is $Maxwellian$. Most important of all is the quality of our measurements for different plasma conditions.

We have found that for most of our measurements we have had a stable plasma that give us a well behaved linear measurement of the V vs I plots, making this approximation valid for our purposes. By changing the plasma parameters we can generate certain unstable and undesirable conditions which we want to avoid. This can be fix by adjusting several parameters like the magnetic field, the gas pressure, or the RF power. The V vs I plot given by the $Langmuir$ probe gives a good measurement of the stability of the plasma conditions, if the plasma is unstable we will get a noisy curve as a result. We then disregard the measurement, and proceed to adjust the plasma conditions to obtain a smooth V vs I plot, giving as a result a reliable T_e and n_e measurements.

5.4   Spectrometer

In this section we present a general overview of the spectroscopy system in ASTRAL. A comprehensive view of the whole system is given by Boivin [33].

Figure 5.8: McPherson Model 218 Spectrometer.

The spectrometer on ASTRAL consists on a McPherson [34] Model 218 (see figure 5.8), **0.3 Meter**, Plane Grating Scanning Monochromator, and a CCD camera with a wavelength range from 250 nm to 1100 nm. Table 5.1 gives the parameters for the McPherson Model 218 Spectrometer.

n(grating groove density)	1200 gr/mm	given
F(focal length)	300 nm (**385** with camera)	given
f-number	5.3 (small grating)	given
D(dispersion)	2.6 nm/mm	given
G_A(grating area)	50×50 mm^2	given
h(slit height)	4.0 mm	chosen
Δx(slit width)	0.01 nm	chosen
Ω(solid angle)	2.77×10^{-2} str	calculated

Table 5.1: Specifications for the McPherson scanning monochromator model 218.

The wavelength in the monochromator is selected electronically by means of a McPherson Model 789A-3 Digital Scan Control and Motor Driver (see figure 5.9), which controls a stepping motor with a close-loop feedback by means of an optical encoder.

Figure 5.9: McPherson Model 789A-3 Digital Scan Control.

The monochromator system for the Model 218 consists on a patented $Criss - Cross$ (U.S. Pat. 3433557) optical design as shown by figure 5.10.
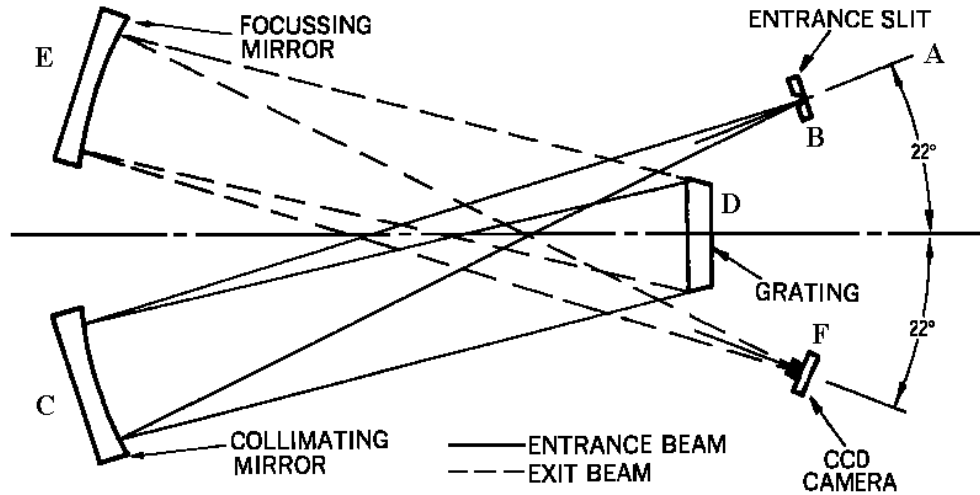
Figure 5.10: Monochromator optical set-up.

The illumination source (A), is aimed at an entrance slit (B). The amount of energy available for use depends on the intensity of the source in the slit. The slit is placed at the effective focus of the parabolic mirror (the collimator C), so that the light from the slit reflected from the mirror is collimated. The collimated light is then refracted by the grating (D), and then is collected by another mirror (focusing mirror E) which refocuses the light (now dispersed) on to the the CCD camera (F). The spectroscopy system in ASTRAL measures number of counts with respect to wavelength. Therefore we must compensate for wavelength since the whole system includes the optics, fiver optics, monochromator, and CCD camera. The detailed compensations (wavelength and intensity) is given by Boivin [33].

A simple procedure that we have used for the wavelength calibration and compensation is found in appendix B.

5.5 Data Processing

The spectroscopy data is acquired by a CCD camera model SPH5P with 1024 pixels, giving a 1024 pixel per spectral window resolution. Each window has a width between 37.4 and 49.5 nm (depending on the spectral region), giving a resolution of 0.0365 to 0.0483 nm per pixel. The monochromator and camera are controlled by the KestrelSpec software [35], and by the McPherson 789A-3 control interface. KestrelSpec has the capability of analyzing the acquired spectral data by integrating the area under the curve for each spectral pick, thus giving us the integrated line intensity. Figure 5.11 shows an example of the 650 nm spectral region as visualized by the KestrelSpec software [35] taken from a Ne plasma run.
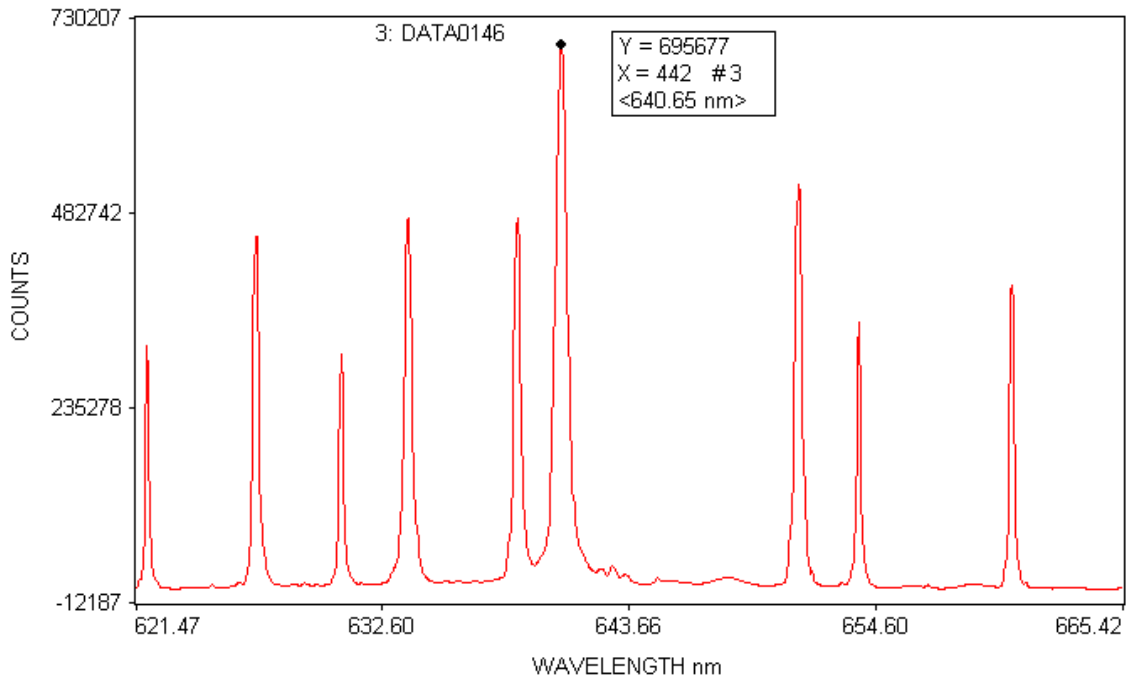
Figure 5.11: Measured spectrum of Ne on the 650 nm region.

In order to analyze the whole data, it is necessary to calculate the line intensity by integrating under each spectral pick. Also we get a different spectral intensity every time we change the plasma conditions. The KestrelSpec [35] software manually allow us to perform these integrals and also to subtract the noise level. We would also have to sort all this data manually as a function of density and temperature. The problem of performing all these tasks manually, is that first we have to give the limits of integration for each spectral pick to the KestrelSpec software, and then perform the integrals and noise subtraction. We have hundreds or thousands of picks to be analyzed for different spectral windows, therefore this process could take considerable amount of time. We would also have to manually compensate each spectral pick with its respective wavelength (as shown in appendix B), thus making the process of analysis even more time consuming. In order to make this process more efficient, we have developed two different fortran codes. The SPECTRUM code performs the process of wavelength compensation, integration, and noise subtraction for each specified spectral pick. The DENS program sorts the processed data from the SPECTRUM code as function of densities and temperatures, and returns output files containing the line intensity integrals for each spectral pick on the same temperature grid. This enable us to get experimental intensity line ratios between different spectral picks. The SPECTRUM program performs the wavelength calibration by using a fit for equation (B.5), and performs the integration process by the use of a simple $Simpson$'s rule of integration. The limits of integration for each spectral pick are determined by the program by finding minimums using the values of the derivatives at the edge of each picks. The program uses those same values to perform the noise subtraction.

In order to run the SPECTRUM program we need to create a namelist input file for the code which contains relevant information about each experimental shot. Figure 5.12 shows an example of the namelist input file for the SPECTRUM program.

```
 File   Edit   Search   Preferences   Shell   Macro   Windows              Help

&in
nwindows = 2
npixels = 1024
npicks = 5
nTe = 10
exptime = 10.0
int = 'calibrated'
noise = 'on'
xpos = 60.0 60.0 60.0 60.0 60.0
       60.0 60.0 60.0 60.0 60.0
Bfield = 0.4 0.4 0.4 0.4 0.4
         0.4 0.4 0.4 0.4 0.4
Ne = 1.306478e+13 9.396779e+12 8.691441e+12 8.509226e+12 6.795197e+12
     3.756800e+12 3.978905e+12 4.421082e+12 4.654343e+12 4.745077e+12
Te = 2.846696 2.825159 2.819939 2.903187 3.129861
     2.893870 3.133502 3.445295 3.372218 3.387873
picks = 854.96 857.59 859.60 864.05 866.04
filepath = ''
filenamein(1,1) = '875a.txt'
filenamein(2,1) = '875b.txt'
filenamein(3,1) = '875c.txt'
filenamein(4,1) = '875d.txt'
filenamein(5,1) = '875e.txt'
filenamein(6,1) = '875f.txt'
filenamein(7,1) = '875g.txt'
filenamein(8,1) = '875h.txt'
filenamein(9,1) = '875i.txt'
filenamein(10,1) = '875j.txt'
filenamein(1,2) = '925a.txt'
filenamein(2,2) = '925b.txt'
filenamein(3,2) = '925c.txt'
filenamein(4,2) = '925d.txt'
filenamein(5,2) = '925e.txt'
filenamein(6,2) = '925f.txt'
filenamein(7,2) = '925g.txt'
filenamein(8,2) = '925h.txt'
filenamein(9,2) = '925i.txt'
filenamein(10,2) = '925j.txt'
&end
```

Figure 5.12: Namelist input file (spectrum.in) for the program spectrum.x.
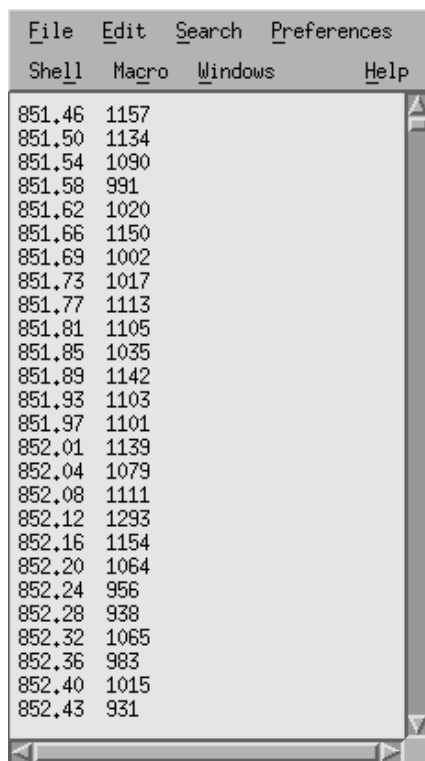
As shown in figure 5.12 we need a good number of input variables in order to run the program, the good news is that we have to create only one file, and all the others are pretty much the same except for a few different namelist input variables like temperatures, densities, and so on. Table 5.2 gives a description of the different namelist input variables the program needs.

nwindows	Number of spectral windows.
npixels	Number of pixels.
npicks	Number of picks to be integrated.
nTe	Number of temperatures and densities.
exptime	Exposure time of the monochromator (sec).
int	Integration wavelength calibration (calibrated/uncalibrated).
noise	Noise subtraction (on/off).
xpos	Position of the $Langmuir$ probe.
Bfield	Magnetic field current (ASTRAL ammeter).
Ne	Electron density (cm^{-3}).
Te	Electron temperature (eV).
picks	Wavelengths of the picks to be integrated.
filepath	File path location of the spectroscopy data files.
filenamein	Names of the spectroscopy data files.

Table 5.2: Description of the namelist input file for the SPECTRUM program.

We see that the SPECTRUM program also reads the text files that contain all the spectroscopy data with their respective wavelengths. The program KestrelSpec [35] allows us to export the spectroscopy data for any spectral window into a text file format. The data file simply contains the wavelengths (or pixel number) on the first column, and the number of counts in the second column.

In our example given by figure 5.12, we have named our files 875a.txt, 875b.txt, and so on in order to be more descriptive. The 875a.txt file contains the spectroscopy data for the spectral window centered at 875.00 nm, the letter that follows represents the temperature and density measured for that specific file. 875a.txt corresponds to the first temperature and density set, 875b.txt corresponds to the second one, and so on. Figure 5.13 shows an example of the spectroscopy data file 875a.txt that KestrelSpec gives.

Figure 5.13: Input data file (in this case 875a.txt) for the program spectrum.x.

Having all our spectroscopy data and our namelist input files, we are ready to run the program.

The SPECTRUM program exits the processed data in an output file (intensity.out), this file contains the temperatures, densities, and the line intensity integrals for the specified spectral picks given in the namelist input file. Figure 5.14 shows an example of the intensity.out file.

File   Edit   Search   Preferences   Shell   Macro   Windows   Help

#Ne Ave = 6.801533E+12 (cm^-3) nTe = 10 int = calibrated					
#Ne(cm^-3)	Te(eV)	854.96	857.59	859.60	864.05	866.04
1.306478E+13	2.846696	0.012231	0.023826	0.293397	0.241874	0.584334
9.396779E+12	2.825159	0.007570	0.014494	0.220767	0.174560	0.436161
8.691441E+12	2.819939	0.002595	0.002919	0.210524	0.162646	0.415755
8.509226E+12	2.903187	0.007354	0.016669	0.233589	0.190468	0.442022
6.795197E+12	3.129861	0.000267	0.006394	0.176903	0.149494	0.350548
3.756800E+12	2.893870	0.010967	0.016471	0.261474	0.272786	0.517247
3.978905E+12	3.133502	0.003113	0.012580	0.228131	0.224006	0.446519
4.421082E+12	3.445295	0.003799	0.006578	0.155246	0.138762	0.305106
4.654343E+12	3.372218	0.004436	0.015421	0.138527	0.127971	0.271909

Figure 5.14: Output file (intensity.out) from the program spectrum.x.

As shown in figure 5.14, the intensity.out file contains the different densities on the first column, the temperatures on the second column, and the intensity line integrals for each spectral pick wavelength with their respective density and temperature. The file also gives on the first row the average density and the number of temperatures in the file. We could already use this data and make a plot of temperature versus integrated line intensity. The only limitation with this data file is that it only contains the data from the specified experimental run. It is desired to obtain a file that contains the sorted data for all the experimental runs. For this purpose we developed the DENS code that takes care of sorting all the processed data automatically, giving us this way several output files containing different averaged densities.

The DENS code also requires a namelist input file (dens.in) that specifies the number and path locations for the different intensity.out files (see figure 5.14) to be read and sort. It also contains the percent difference limit for sorting the different densities. Figure 5.15 shows an example of the dens.in namelist input file.


```
 File   Edit   Search   Preferences   Shell   Macro   Windows          Help

&in
ndir = 12
dirname = '../1Ne012108' '../1Ne012508' '../1Ne020108' '../1Ne020408'
          '../1Ne020608' '../1Ne020808' '../1Ne021308' '../1Ne021808'
          '../1Ne022008' '../1Ne022308' '../1Ne022708' '../1Ne022908'
densp = 0.12
&end
```

Figure 5.15: Namelist input file (dens.in) for the program dens.x.

Table 5.3 gives the description of the namelist input file for the DENS program.

ndir	Number of directories that contain the intensity.out files.
dirname	Path locations of the intensity.out files.
densp	Density percentage difference for sorting the data.

Table 5.3: Description of the namelist input file for the DENS program.

In the example given in figure 5.15, we have a total of twelve directories where the DENS program will locate and read the intensity.out files given by the SPECTRUM program. We have named the directories by the date the experiment was performed, and we have also set the value of the percentage of the densities to **12%**. The DENS program gives several output files named by the average density of the data contained in each file.

Figure 5.16 shows the output file Ne8.47E12.dat, which means that the density is centered to the average value of 8.47×10^{12} cm^{-3}, and the data that is contained is within $\pm 12\%$ of that density.


```
File   Edit   Search   Preferences   Shell   Macro   Windows                              Help

#Ne(cm^-3)        Te(eV)       854.96       857.59       859.60       864.05       866.04
9.396779E+12    2.825159    0.007570    0.014494    0.220767    0.174560    0.436161
8.691441E+12    2.819939    0.002595    0.002919    0.210524    0.162646    0.415755
8.509226E+12    2.903187    0.007354    0.016669    0.233589    0.190468    0.442022
8.814332E+12    2.844946    0.009510    0.026216    0.302408    0.231451    0.594371
7.835027E+12    2.890977    0.009441    0.025279    0.293970    0.236184    0.562440
7.818341E+12    2.654243    0.000812    0.002633    0.123484    0.101969    0.226988
7.776605E+12    2.614343    0.001696    0.006295    0.109992    0.086359    0.218907
9.528866E+12    3.291699    0.010289    0.006380    0.257068    0.204094    0.477681
7.892724E+12    2.861424    0.000000    0.016725    0.203825    0.169833    0.418342
7.460198E+12    2.913388    0.000000    0.009166    0.196932    0.167404    0.391827
8.470932E+12
```

Figure 5.16: Output file (in this case Ne8.47E12.dat) for the program dens.x.

As we see in the example given in figure 5.16, the output file for the DENS code gives simply a column for the densities, a column for the temperatures, and several columns for the sorted line intensity integrals for different spectral picks. This format allow us to graph and analyze the data in excell or in any other package of our choice. We have used these programs in the analysis of some of the Ar data given in chapter 6, and the Ne data given in chapter 8.

CHAPTER 6

AR$^+$ MODELING AND EXPERIMENT

6.1 Introduction

Argon is of current interest in fusion TOKAMAK studies as a species useful for radiative cooling of the divertor region and for disruption mitigation [36]. It has also proven useful as a spectral diagnostic [37, 10]. The aim of this chapter is to model Ar II emission from ASTRAL. The accuracy of the modeling depends strongly on the quality of the underlying atomic data. A secondary aim is to determine if the Ar emission from ASTRAL can be used to test the atomic physics data in our collisional-radiative model. In particular, it would be useful to test recent DR data for the low charge states of argon. Loch et al. [38] found that when new ionization and recombination data was used for the near neutral argon ion stages there was a shift in the temperature at which Ar$^+$ was expected to be seen. It should be possible to see this experimentally. Griffin et al. [6] found significant differences in Ar$^+$ excitation cross-sections when continuum coupling effects were included. If this could be verified indirectly through spectral measurements it would be the first experimental observation of continuum coupling effects.

Helicon sources have been used to study high density plasma sources [39, 40], as well as applications in space plasma propulsion [41], and in many other applications in studies of basic plasma physics and plasma wall interactions [42]. Argon spectra have been used with some success as spectral diagnostics. For high temperature plasmas, the He-like lines have been used as electron temperature and density diagnostics [10]. Ar III forbidden line spectra have been used as electron temperature and density diagnostics of planetary nebula [10].

Much work has been done improving the atomic data available for argon. The Dielectronic Recombination project (DR project [43]) has calculated DR for all ion stages from Na-like Ar through to H-like Ar [43]. Much DR work has also been done by Gu [44] for the same ion stages. Loch et al. [38] calculated Configuration Average Distorted Wave (CADW) DR data for the lower ion stages of Ar. This data was found to effect the temperatures at which these low charge states were abundant. Distorted Wave ionization data has been calculated for Ar^+ through to Ar^{17+} [38] obtaining reasonable agreement with experimental ionization cross-sections. For the neutral ion stage RMPS excitation data was calculated by Griffin et al. [45], and found to be in good agreement with experiment. For Ar^+ the non-pseudo-states R-Matrix excitation data of Griffin et al. [47] was recently updated with RMPS excitation data [6]. Thus, we seek to test the new low charge state DR data of Loch et al. [38], and the new excitation data of Griffin [6].

6.2 Atomic Data

The atomic data used in our modeling work came from a variety of sources. The electron impact ionization and recombination data is taken from Loch et al. [38]. Ionization of neutral argon consists of RMPS data [45]. Data for the higher ion stages comes from Distorted Wave calculations. The radiative-recombination data was taken from the work of Badnell [46]. For Ar^{6+} through to Ar^{17+} the DR data was taken from the work of the DR project [43]. For DR data of neutral Ar through to Ar^{5+} Configuration Average Distorted Wave (CADW) DR data was used from Loch et al. [38]. We will compare the results of our new data set with those using the existing data in the ADAS [11] database. Table 6.1 gives a summary of our atomic data for the first three ion stages of argon.

Process	Old Data	New Data
Dielectronic Recombination	Semi-empirical $\geqslant Ar^{6+}$ DW $\geqslant Ar^{6+}$	CADW $\geqslant Ar^{6+}$ DW $\geqslant Ar^{6+}$
Ionization	Distorted Wave for all	RMPS for Ar [2]
Excitation of Ar^+ Excitation of Ar^{2+}	R-Matrix [5] PWB	RMPS [4] R-Matrix [6]

Table 6.1: Overview of atomic data.

The electron-impact excitation data for Ar^+ consists of the recent RMPS data of Griffin et al. [6]. This replaces the previous non-pseudo-states $\boldsymbol{R}$-Matrix calculations of Griffin et al. [47]. The continuum coupling effects associated with pseudo-state $\boldsymbol{R}$-Matrix calculations was found to be significant for Ar^+ (up to a 30% effect), and should have an effect on the Ar II spectral emission. To the best of our knowledge these effects on excitation cross-sections have never been verified experimentally. One of the aims of this chapter is to see if the continuum coupling effects can be tested using the spectral measurements from the ASTRAL plasma source.

6.3 Collisional-Radiative Modeling and Ionization Balance

To produce a modeled spectrum one needs to use the aforementioned data in a collisional-radiative model. Our application of collisional-radiative theory to the calculation of excited populations is based on the atomic data and analysis structure (ADAS) package [11], and is described in chapter 2. Using the quasi-stable approximation we split the calculation of the excited populations into two points; an ionization balance calculation to work out the ground and metastable populations of each ion stage, and an excited level population calculation for the levels within a given ion stage. To calculate the fractional abundance of the ground and metastables within each ion stage we solve equation (2.20).

Figure 6.1 shows the fractional abundances of Ar, Ar^+, and Ar^{2+} using the data currently in ADAS [11] and our new atomic data set.
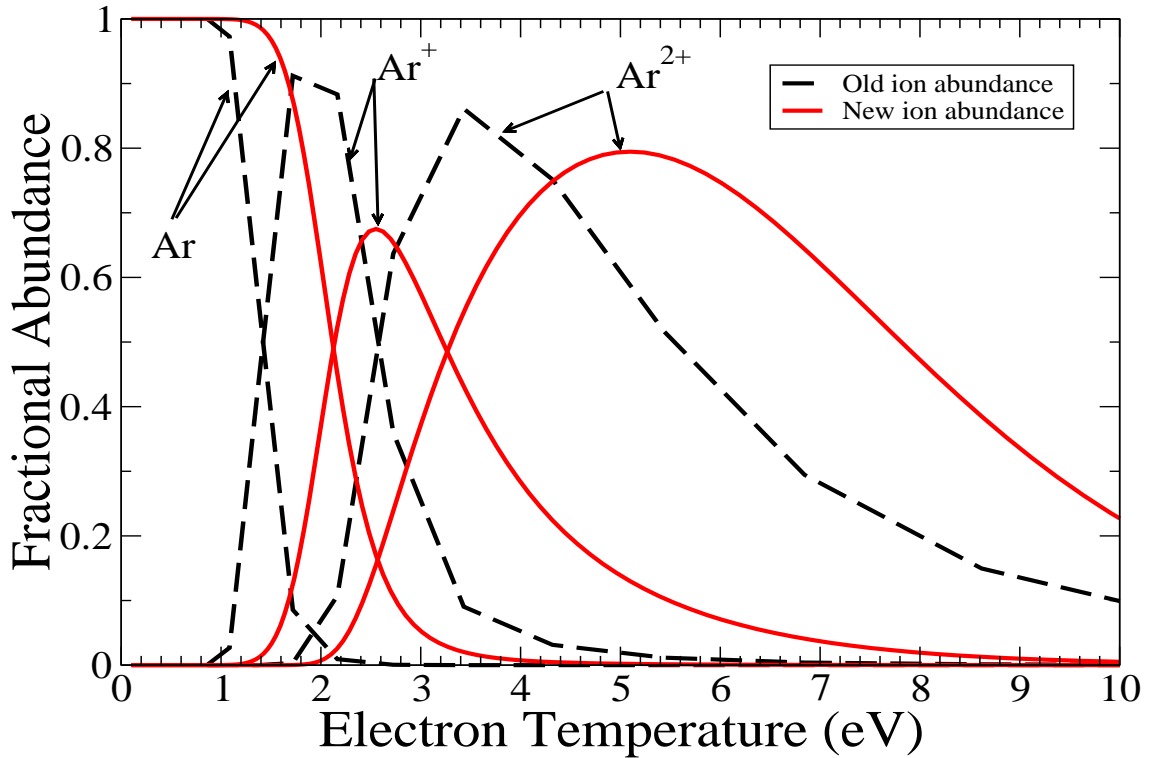
Figure 6.1: The solid line shows our fractional abundance results using the new ionization and recombination data.

The differences in the dielectronic recombination data is the main cause for the shift in the expected abundances. The CADW DR rate coefficients of Loch et al. [38] are lower than the semi-empirical data currently used in ADAS. The new RMPS ionization data for neutral Ar also contributes to the differences.

Thus, the new atomic data predicts that Ar$^+$ should have a peak abundance close to 2 eV with the old data has it peaking at 2.5 eV. This should be observable in our helicon plasma experiment via the temperature onset of the Ar II spectral emission lines. This would be a very useful test of the atomic data as no experimental measurement exist for DR for the open p-shell low charged states of argon.

6.4 Emission Modeling

In order to accurately model the emission of Ar II, we need to calculate the intensity of each spectral line which is given by

$$I_{i \to j} = \int \frac{N^{Ar+}}{N_{tot}}(x) \frac{N_i^{Ar+}}{N^{Ar+}}(x) A_{i \to j} dx \qquad (6.1)$$

where x is the position along the line of sight and the fractional abundance and excited population fraction are functions of the line of sight through their temperature and density dependence. We can also see that we need to have an accurate value for the $Einstein$'s A_{jk} coefficients that we use. We rely on the $Einstein$'s A_{jk} coefficients calculated by Griffin et al. [45] as part of their RMPS calculation, and supplement these with NIST values [22] for a number of transitions. We are aware that much of the NIST $Einstein$'s A_{jk} coefficients of Ar II have large uncertainties with relative errors that can vary from 3% up to 75%, 100%, or more. We are just including those values around 10% uncertainty in our calculation to ensure the accuracy of our model. Another very important factor that plays a key role in our modeling is the knowledge of the plasma density and temperature profiles along the line of sight. As we see in equation (6.1), knowledge of these profiles is necessary for an accurate computation of the intensity. Figures 6.2 and 6.3 show the measured electron temperature and density distributions in the helicon plasma for conditions typical of our Ar experiments as measured by a $Langmuir$ probe. The results have been normalized to allow a general $Gaussian$ distribution functions to be fitted that can then be used for any T_e and N_e conditions.
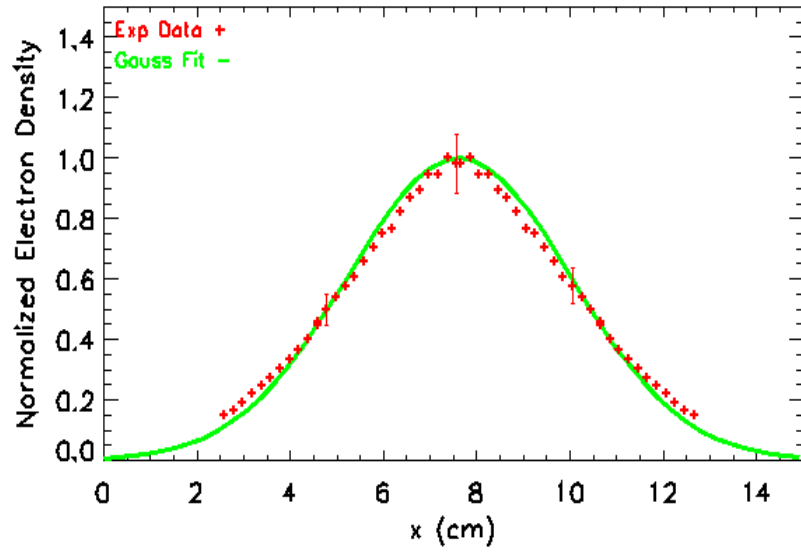
Figure 6.2: Normalized electron density distribution along the diameter of the vacuum chamber in ASTRAL .
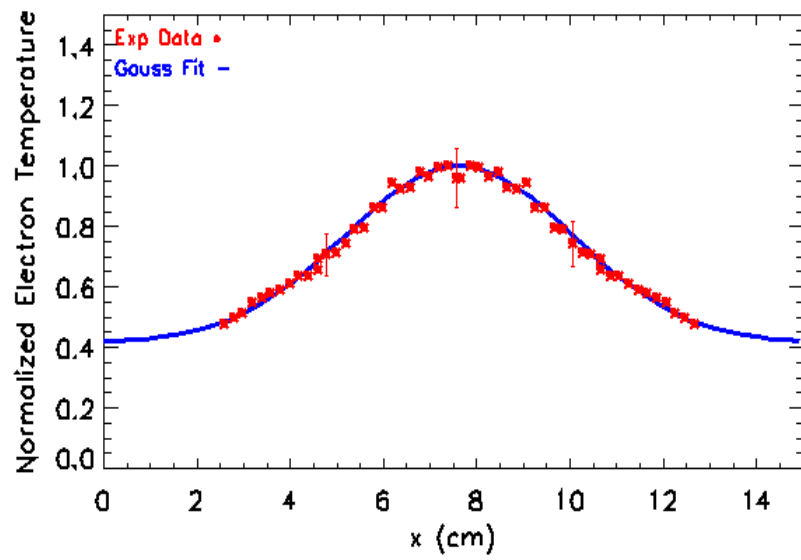
Figure 6.3: Normalized electron temperature distribution along the diameter of the vacuum chamber in ASTRAL.

93

It was found that a *Gaussian* distribution for the density, and a modified *Gaussian* distribution for the temperature fitted the experimental data very well as seen in figures 6.2 and 6.3. The equations for the fits are given by

$$\rho(x) = e^{-\frac{(x-L/2)^2}{2\sigma_\rho^2}}$$
(6.2)

$$T(x) = (1-h)e^{-\frac{(x-L/2)^2}{2\sigma_T^2}} + h$$
(6.3)

Where $h = 0.415$, $L = 15.24$ cm, $\sigma_\rho = 2.4$ cm, $\sigma_T = 2.45$ cm, and x is the position along the diameter of the vacuum chamber. In our modeling we assume a *Gaussian* distribution based on a temperature measured at a single point by the *Langmuir* probe. Along the line of sight the fractional abundances are calculated for each N_e/T_e grid point. The excited populations are also calculated for the same grid and the total intensity obtained using equation (6.1).

94

To get an idea for the likely of emission for different plasma temperatures, figure 6.4 shows the modeled contribution of the line of sight to the total line intensity (i.e. the integrand of equation 6.1) as function of temperature.
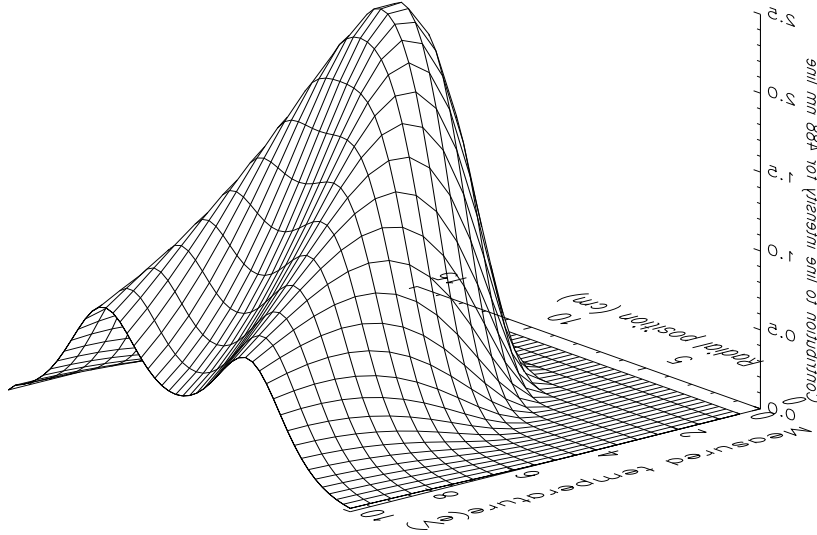
Figure 6.4: Contribution to the total intensity along the line of sight as a function of central electron temperature.

At low temperatures, most of the Ar II emission originates from the center of the plasma column. From temperatures of about 7 eV or higher one starts to see a dip in the Ar II emission coming from the core. This is because of the drop in Ar^+ abundances at these temperatures. By 10 eV core temperature one would expect to see Ar II emission mostly coming from the cooler edges of the plasma as a consequence of the temperature profile (see figure 6.3).

6.5 Metastable Lifetimes and Opacities

As shown in section 2.4.2, the metastable lifetime can be estimated from equation (2.9). In our case we consider Ar^+ to have no metastables but the ground, and the $3p^5$ (^2P) term to contain most of the Ar^+ population. We evaluated the expected lifetimes of the next excited term $3s3p^6$ (^2S) for different temperatures and an electron density of 10^{12} cm^{-3}. We have assumed that $T_i \approx \frac{1}{10}T_e$. We also show the distance that an Ar^+ ion in the $3s3p^6$ (^2S) state would travel before decaying, to get an indication of the likelihood of this excited term being metastable and undergoing a collision with the wall before reaching equilibrium with the ground. Table 6.2 shows these results.

T_e (eV)	Rad-Lifetime(Sec.)	Collsn-Lifetime(Sec.)	Tot-Lifetime(Sec.)	Trav-Dist.(cm)
0.3447	8.4746×10^{-3}	$2.2819 \times 10^{+2}$	8.4743×10^{-3}	0.0004
0.6894	8.4746×10^{-3}	$2.0645 \times 10^{+2}$	8.4742×10^{-3}	0.0006
1.7235	8.4746×10^{-3}	$5.1544 \times 10^{+1}$	8.4732×10^{-3}	0.0009
3.4471	8.4746×10^{-3}	$3.0906 \times 10^{+1}$	8.4723×10^{-3}	0.0013
6.8942	8.4746×10^{-3}	$3.0233 \times 10^{+1}$	8.4722×10^{-3}	0.0019
17.2354	8.4746×10^{-3}	$4.3470 \times 10^{+1}$	8.4729×10^{-3}	0.0030
34.4709	8.4746×10^{-3}	$6.2275 \times 10^{+1}$	8.4734×10^{-3}	0.0042
68.9417	8.4746×10^{-3}	$8.7049 \times 10^{+1}$	8.4738×10^{-3}	0.0060

Table 6.2: Lifetimes of the Ar^+ ion for the $3s3p^6$ (^2S) term with electron density $n_e = 10^{12}$ cm^{-3}.

As we see in table 6.2, the associated mean-free-path of the Ar^+ ion varies from 0.0004 to 0.006 cm, much less than the dimensions of our plasma column (diameter = 15.24 cm). Thus we expect the quasi-static approximation to be good for our Ar^+ modeling.

Figure 6.5 shows the traveled distance of the Ar$^+$ ions as a function of electron temperature.
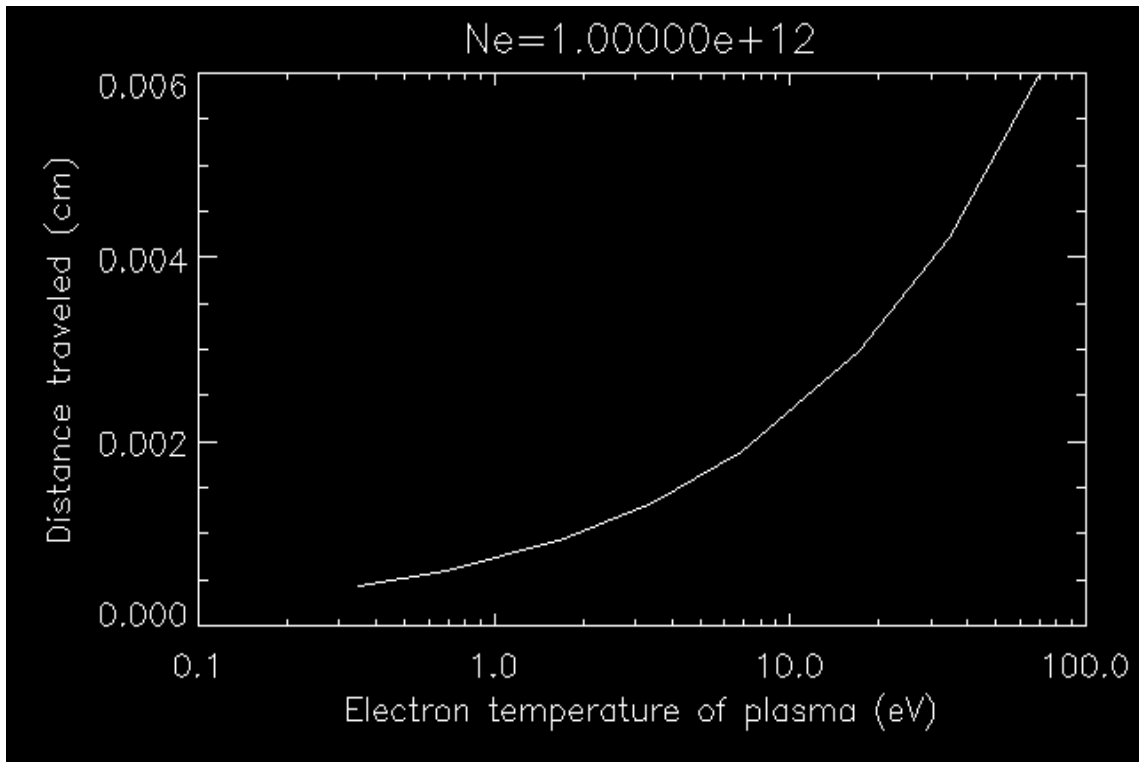
Figure 6.5: Traveled distance of the Ar$^+$ ions as a function of electron temperature.

In order to calculate the opacity of our plasma column we made use of the ADAS214 code and assumed a parabolic density profile along the diameter of the vacuum chamber, and a cylindrical geometry. We use $n_e = 10^{12}$ cm^{-3} as the typical value for our electron density.

We computed the opacity for transitions from the following terms to the ground state. The index numbers correspond to those used in our adf04 file.

- 1. $1s^2 2s^2 2p^6 3s^2 3p^5$ (^{2}P) (Ground)

- 2. $1s^2 2s^2 2p^6 3s 3p^6$ (^{2}S)

- 3. $1s^2 2s^2 2p^6 3s^2 3p^4 3d$ (^{4}D)

- 4. $1s^2 2s^2 2p^6 3s^2 3p^4 4s$ (^{4}P)

- 5. $1s^2 2s^2 2p^6 3s^2 3p^4 4s$ (^{2}P)

By running the ADAS214 code to compute the opacities for these transitions, we found that our observed spectral lines are optically thin, and only the $3p^4 4s$ (^{2}P) transition to the ground is moderately optically thick. Thus did not significantly affect our population modeling.

6.6 Experimental Results

Measurements were taken across the whole spectral range (300 nm to 1100 nm), and 44 strong lines were identified. From all of the observed lines we extracted integrated line intensities for a selection that were unambiguously identified, were strong enough to be observed, and most of them had no obvious line blends. For the ones that were blended we included the blending in our theoretical modeling in the integration process (6.1). The complete analysis of all the Ar spectral lines will be published in a future paper. For this work we consider a selection of strong lines for the purpose of testing the ionization/recombination and excitation data in our model. Figure 6.6 shows a $Grotrian$ diagram of Ar^{+} transitions and table 6.3 shows a summary of the lines we considered.
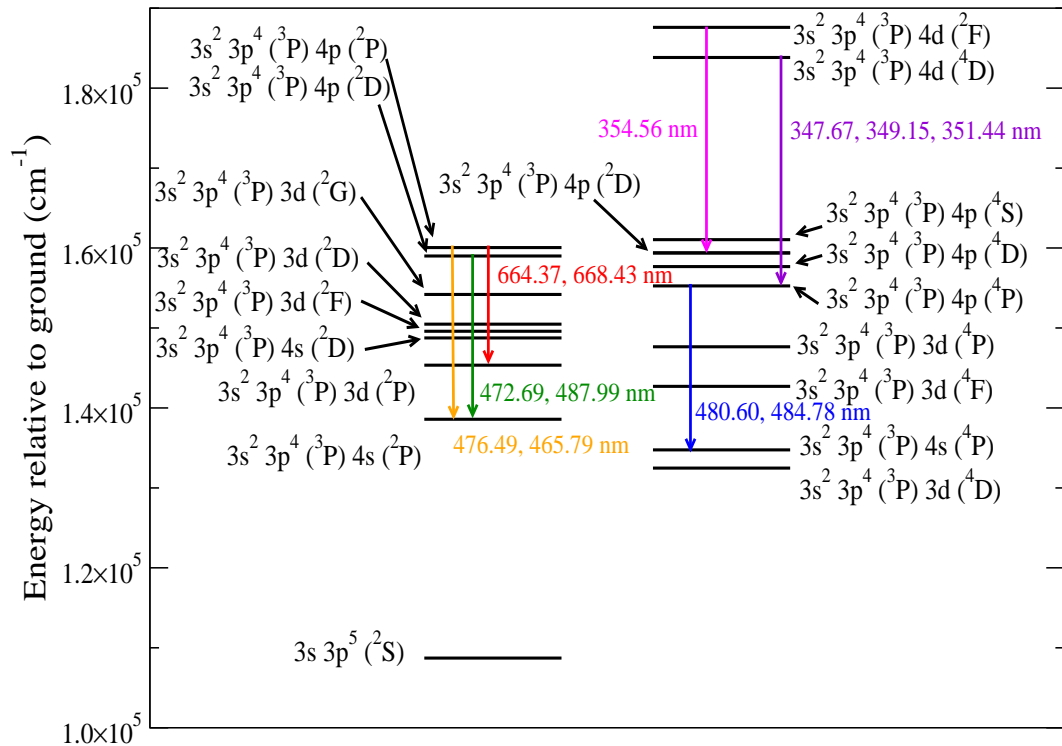
Figure 6.6: $Grotrian$ diagram of Ar^{+}.

Thus, we will mostly be considering dipole transitions within a spin system. In our search for T_e sensitive line ratios we investigated ratios of lines from the two different spin systems. We also suspected that ratios of the 347.67, 349.15, 351.44, and 354.56 nm lines to the other lines may be T_e sensitive due to the high energy necessary to excite to the $3p^4 4d$ (^{2}F), and $3p^4 4d$ (^{4}D) terms (see figure 6.6).

Wavelength (nm)	Upper level	Lower level
347.67 nm	$3p^4 4d$ ($^4D_{5/2}$)	$3p^4 4p$ ($^4P_{5/2}$)
349.15 nm	$3p^4 4d$ ($^4D_{7/2}$)	$3p^4 4p$ ($^4P_{5/2}$)
351.44 nm	$3p^4 4d$ ($^4D_{5/2}$)	$3p^4 4p$ ($^4P_{3/2}$)
351.99 nm	$3p^4 4d$ ($^4F_{5/2}$)	$3p^4 4p$ ($^4D_{5/2}$)
354.56 nm	$3p^4 4d$ ($^2F_{5/2}$)	$3p^4 4p$ ($^2D_{3/2}$)
355.95 nm	$3p^4 4d$ ($^2F_{7/2}$)	$3p^4 4p$ ($^2D_{5/2}$)
358.24 nm	$3p^4 4d$ ($^4F_{5/2}$)	$3p^4 4p$ ($^4D_{3/2}$)
465.79 nm	$3p^4 4p$ ($^2P_{1/2}$)	$3p^4 4s$ ($^2P_{3/2}$)
472.69 nm	$3p^4 4p$ ($^2D_{3/2}$)	$3p^4 4s$ ($^2P_{3/2}$)
473.59 nm	$3p^4 4p$ ($^4P_{3/2}$)	$3p^4 4s$ ($^4P_{5/2}$)
476.49 nm	$3p^4 4p$ ($^2P_{3/2}$)	$3p^4 4s$ ($^2P_{1/2}$)
480.60 nm	$3p^4 4p$ ($^4P_{5/2}$)	$3p^4 4s$ ($^4P_{5/2}$)
484.78 nm	$3p^4 4p$ ($^4P_{1/2}$)	$3p^4 4s$ ($^4P_{3/2}$)
487.99 nm	$3p^4 4p$ ($^2D_{5/2}$)	$3p^4 4s$ ($^2P_{3/2}$)
664.37 nm	$3p^4 4p$ ($^4D_{7/2}$)	$3p^4 3d$ ($^4F_{9/2}$)
668.43 nm	$3p^4 4p$ ($^4D_{5/2}$)	$3p^4 3d$ ($^4F_{7/2}$)

Table 6.3: Table of some of the extracted spectral lines.

Our RMPS excitation data is term resolved (LS), thus we first checked that the level populations within a term are statistically populated. This is important because we are using the (LS)-resolved data of Griffin et al. [6] and assuming statistically populated levels in our model.

Figure 6.7 shows line ratios of transitions originating from different levels with the same term. If the levels are statistically populated, the ratio should be equal to the ratio of statistical weights and $Einstein$'s A_{jk} coefficients. This expected value is also shown on the plots. If appears that the assumption of statistically populated levels is very reasonable. The majority of the line ratios that can be used to test the statistical distribution of levels within a term share a similar level of agreement with the spectral ratio, however, we notice that some lines show deviations from the expected statistical ratio.
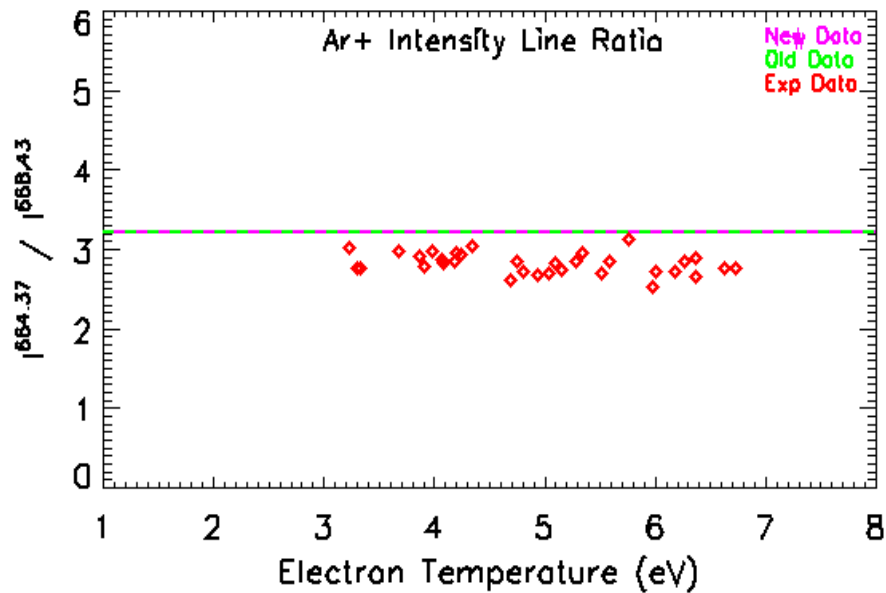
Figure 6.7: Intensity line ratio of I(664.37)/I(668.43).

We next compared the experimental measurements using the new DR data of Loch et al. [38] and older data sets. In both data sets we used the most recent RMPS excitation data. Thus the only difference in the two data sets is the ionization/recombination data used. Figures 6.8, 6.9, 6.10, 6.11, and 6.12 show these results.

The older data does not correctly predict the onset of Ar II emission, while the newest data is in reasonable agreement with the measurements. We notice that the *Gaussian* distribution of T_e and N_e along the line of sight also has to be included. A homogeneous plasma model does not reproduce the slope of the intensity at higher temperatures. It can also be seen that there is a strong scattering in the measured intensities. This is due to variations in N_e for the different temperatures measured.
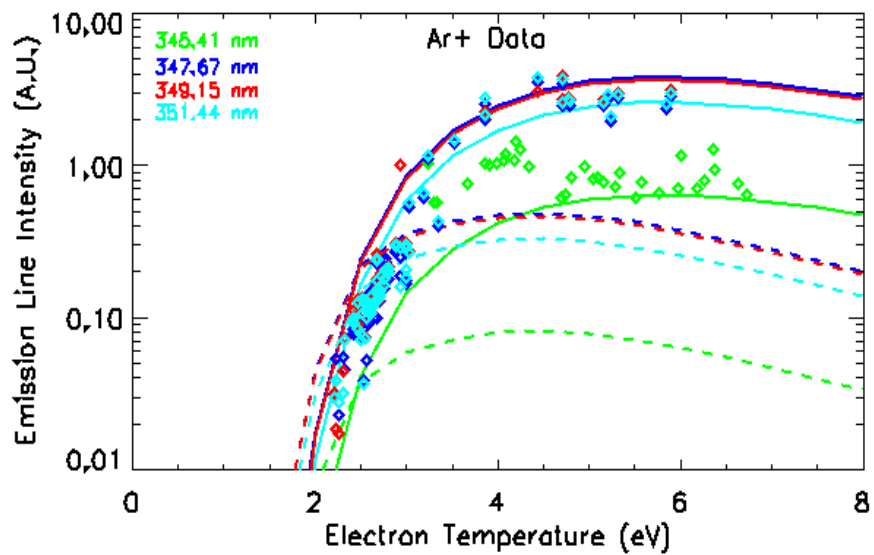
Figure 6.8: New ionization balance data gives good agreement with the experimental measurements for all the different lines. The solid line shows the results using the new ionization balance data, the dashed line shows the results by using the old ionization balance data.
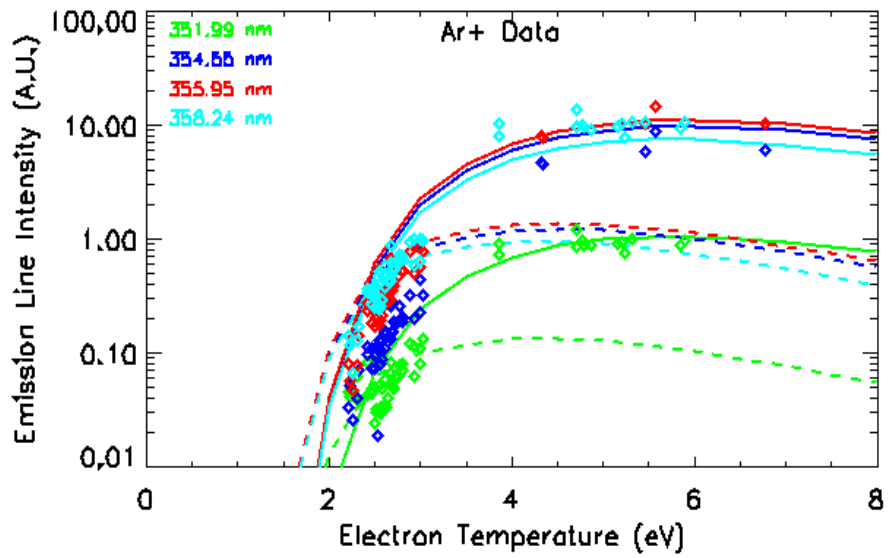
Figure 6.9:
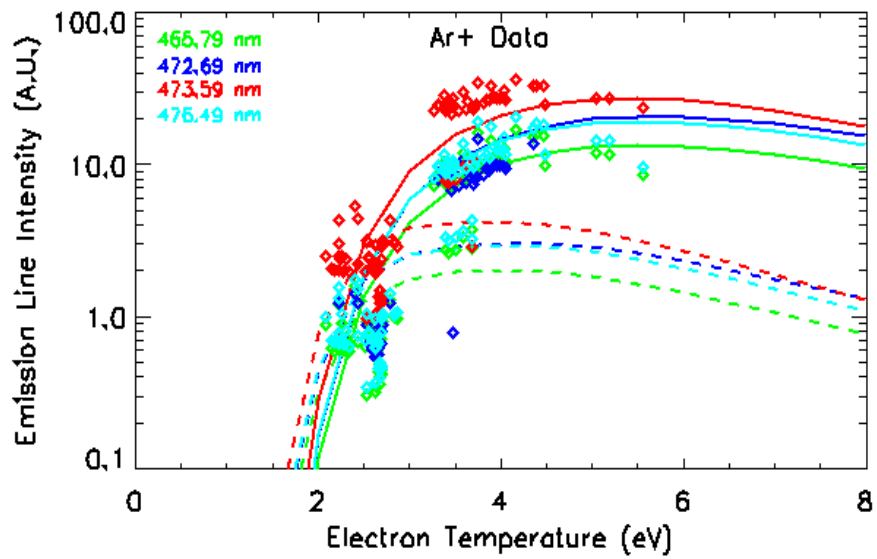
Figure 6.10: New ionization balance data gives good agreement with the experimental measurements for all the different lines. The solid line shows the results using the new ionization balance data, the dashed line shows the results by using the old ionization balance data.
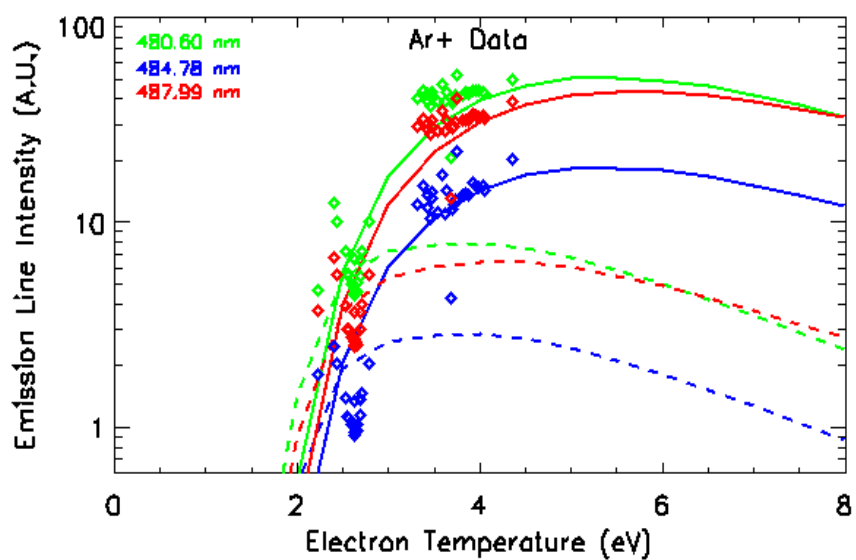
Figure 6.11:
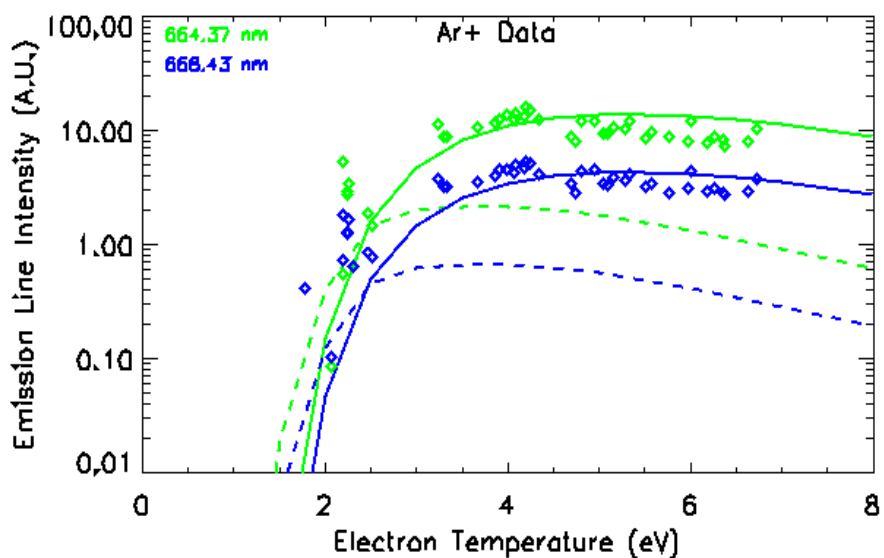
Figure 6.12: New ionization balance data gives good agreement with the experimental measurements for all the different lines. The solid line shows the results using the new ionization balance data, the dashed line shows the results by using the old ionization balance data.

There is, in general, good agreement between the theoretical line intensities and the experimental measurements when the most recent atomic data is used. We next looked at line ratios and whether they could be used to test the RMPS excitation data. We present a selection of results using the RMPS and R-Matrix data while using the most recent ionization/recombination data. The effects of the different excitation data sets become clearer when we look at line ratios. Figures 6.13, 6.14, 6.15, 6.16, 6.17, and 6.18 show several of these line ratios. The new data produces closer agreement with the experimental measurements, though the scatter in the experimental measurements makes a definite conclusions difficult. The experimental measurements are consistent with the RMPS atomic data, and are in disagreement with the R-Matrix data. We believe that this is the first experimental verification of continuum coupling effects in electron-impact excitation data.
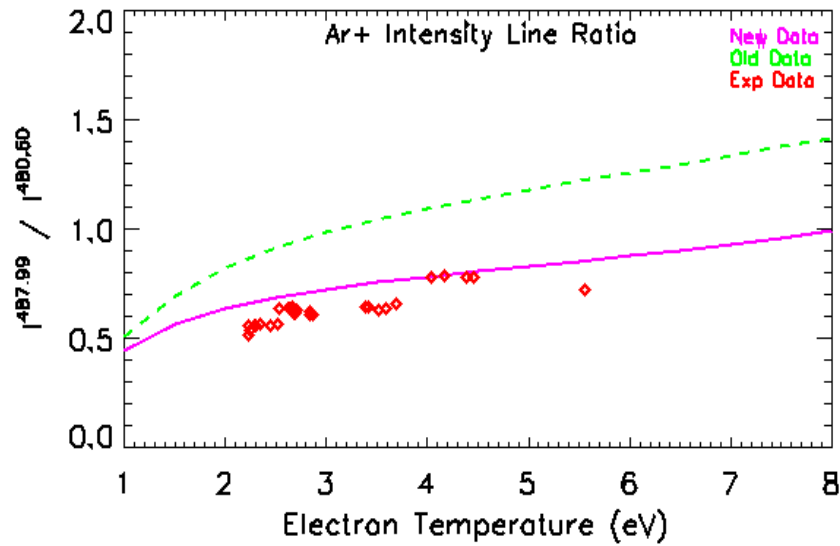
Figure 6.13: Intensity line ratio of I(487.99)/I(460.60). The solid line shows the results using the RMPS excitation data.
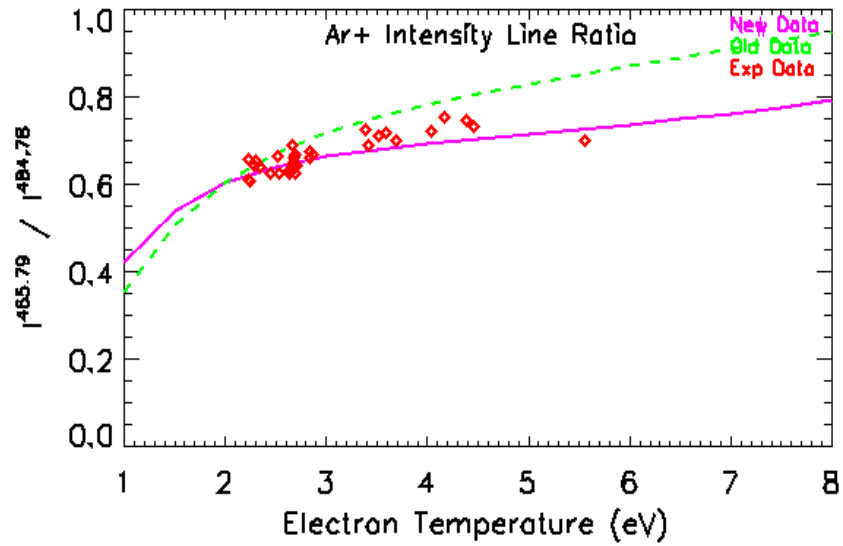
Figure 6.14: Intensity line ratio of I(465.79)/I(484.78). The solid line shows the results using the RMPS excitation data.
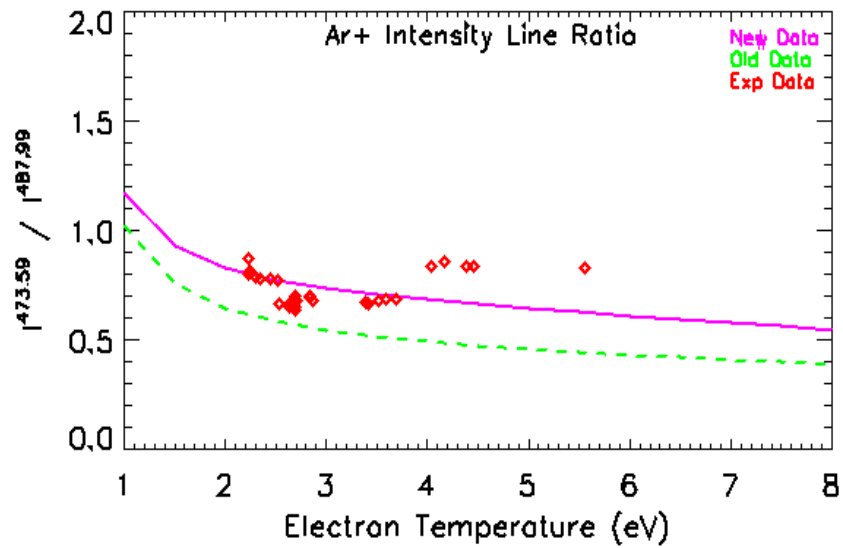
Figure 6.15: Intensity line ratio of I(473.59)/I(487.99). The solid line shows the results using the RMPS excitation data.

106
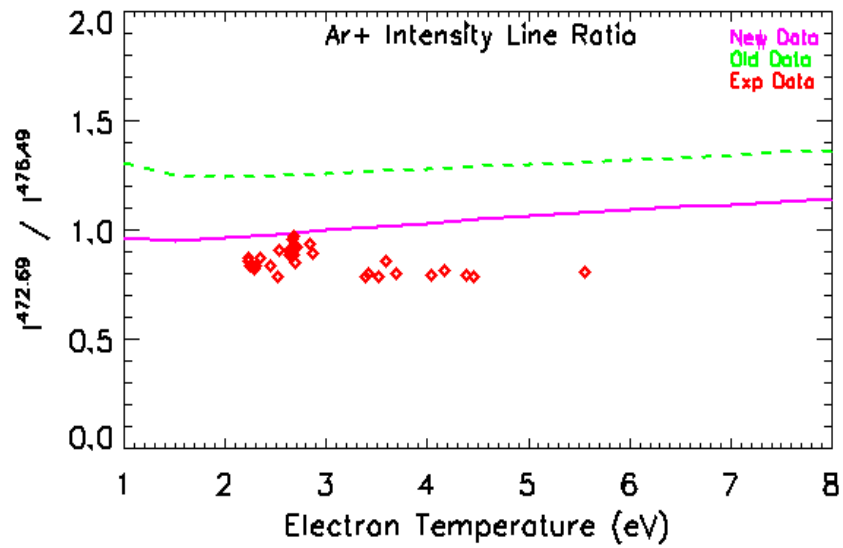
Figure 6.16: Intensity line ratio of I(472.69)/I(476.49). The solid line shows the results using the RMPS excitation data.
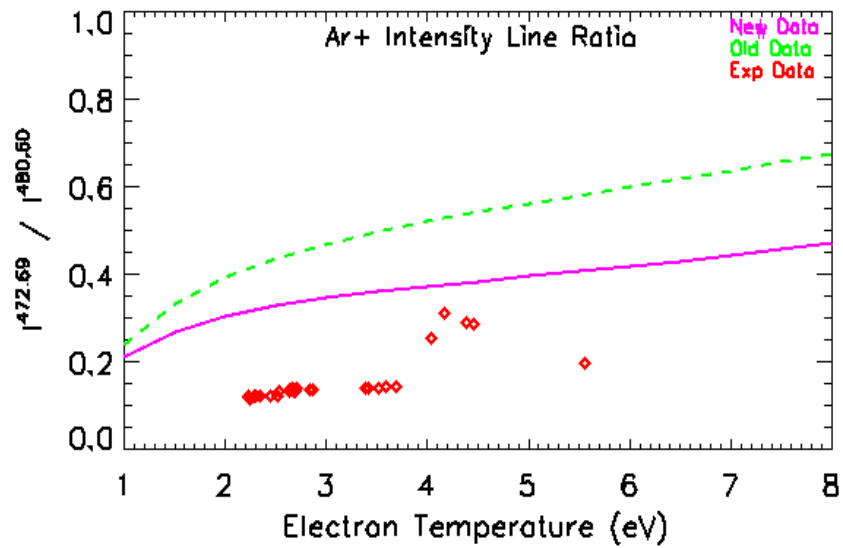
Figure 6.17: Intensity line ratio of I(472.69)/I(480.60). The solid line shows the results using the RMPS excitation data.
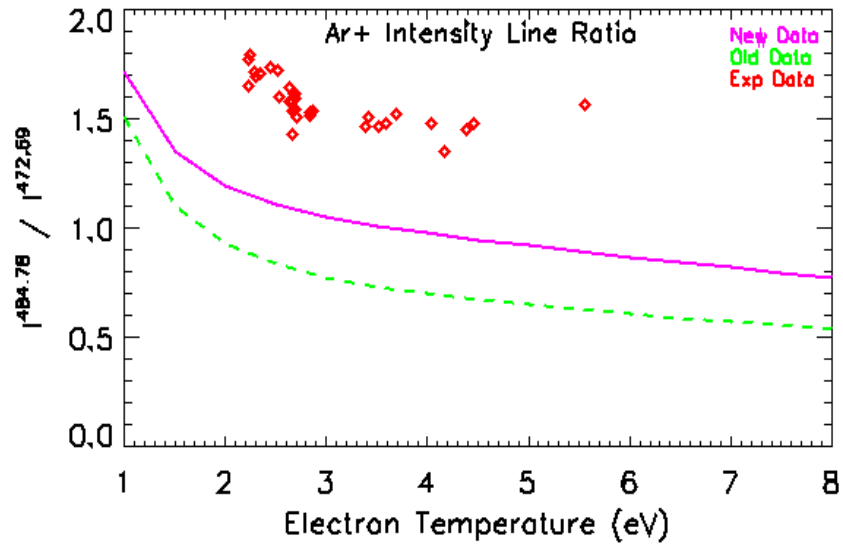
Figure 6.18: Intensity line ratio of I(484.78)/I(472.69). The solid line shows the results using the RMPS excitation data.

As can be seen from figure 6.6, the lines at 347.67, 349.15, and 351.44 nm originate from levels that are higher in energy than the upper levels from the rest of the observed transitions. This has the potential to make line ratios of these lines to other observed lines very temperature sensitive, and more sensitive to continuum coupling effects (which affect the levels closest to the continuum the most).

We show some of these line ratios in figures 6.19 and 6.20. Figure 6.19 shows the ratio between the 349.15 nm line and the 668.43 nm, and is clearly very temperature sensitive. The line ratio between the 354.55 nm and the 668.43 nm lines is shown in figure 6.20, and results in the most significant differences between the R-Matrix and the RMPS calculation, while also being sensitive to temperature. By examining the $Grotrian$ diagram in figure 6.6, we notice that more energy (from the ground [22]) is required to populate the upper levels $3p^44d$ ($^4D_{7/2}$) (22.77 eV) for the 349.15 nm line, and the $3p^44d$ ($^2F_{5/2}$) (23.26 eV) for the 354.55 nm line. The upper level for the 668.43 nm line is $3p^44p$ ($^4D_{5/2}$) which has an energy from the ground of 19.55 eV. It is expected that as temperature increases, the population of the upper levels of the 349.15 nm and the 354.55 nm lines to increase also. It is also expected that the 354.55 nm will be the most sensitive since is the one with highest energy level value from the two. By also looking to the ionization balance calculation shown in figure 6.1, we conclude that most of the energetic electrons need to excite to the $3p^44d$ ($^4D_{7/2}$), and $3p^44d$ ($^2F_{5/2}$) levels must be coming from the tail of the $Maxwellian$.

Figure 6.19 shows the experimental ratio between the 349.15 nm and the 668.43 nm lines. We can see that the experimental data lies closer to the newly calculated RMPS data by Griffin et al. [6]. This help us to show the first reliable experimental observation of continuum coupling effects in the electron-impact excitation data, and it demonstrates the reliability of the newly calculated RMPS data to model the emission of Ar^+ and its applications for plasma temperature line ratio diagnostics. Unfortunately we do not have good experimental data to compare the 354.55 nm and the 668.43 nm line ratio (see figure 6.20). This ratio is even more sensitive to electron temperature, and shows a bigger difference between the R-Matrix and the RMPS data. Future line intensity experimental data for this line ratio would be very useful.
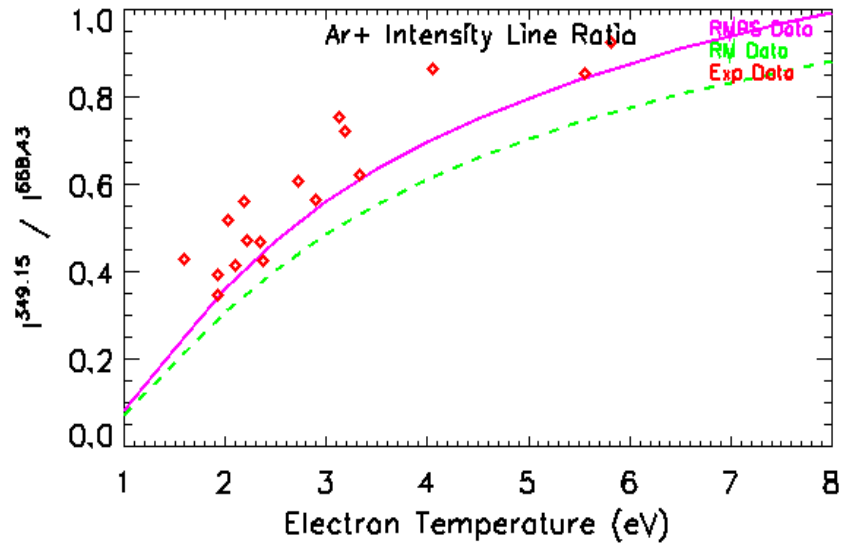
Figure 6.19: Intensity line ratio of I(349.15)/I(668.43). The solid line shows the results using the RMPS excitation data.
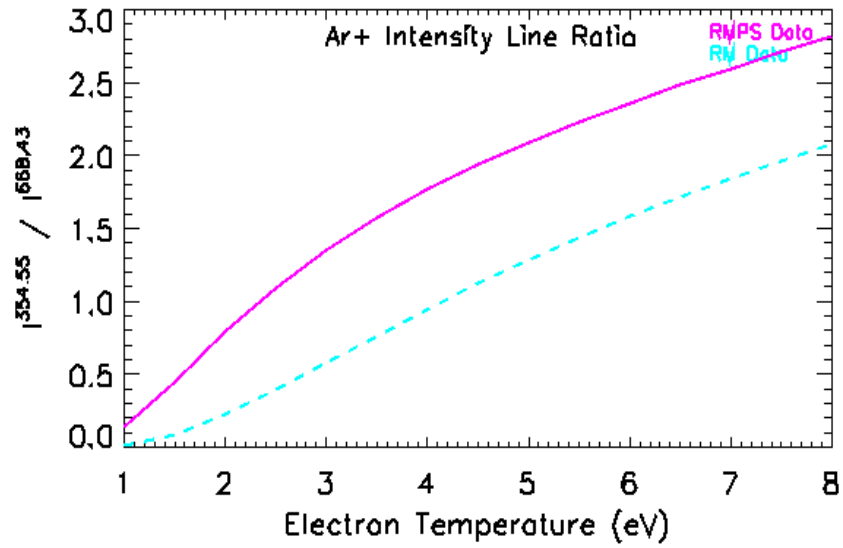
Figure 6.20: Intensity line ratio of I(354.55)/I(668.43). The solid line shows the results using the RMPS excitation data.

AR^{2+} MODELING [48]

7.1 Introduction

Argon is an important species for TOKAMAK studies, being used as a gas to radiatively cool the divertor (see chapter 6.1), and as a potential means of mitigating plasma disruptions (Whyte et al. [36]). In particular, Ar III lines have been shown to provide useful spectral diagnostics for astrophysical studies (Keenan and McCann [10]; Keenan and Conlon [49]). The $3s^2 3p^4$ ($^1D_2$) $\rightarrow 3s^2 3p^4$ ($^3P_{1,2}$) and $3s^2 3p^4$ ($^1S_0$) $\rightarrow 3s^2 3p^4$ ($^1D_2$) transitions of Ar III emit strongly in planetary nebulae (Aller and Keyes [50]; Perez-Montero et al. [51]). Transitions within the first 5 levels of Ar^{2+} have been shown to be very useful as spectral diagnostics. The ratio of $I(\lambda 7135\mathring{A} + \lambda 7751\mathring{A})/I(\lambda 5192\mathring{A})$ has been shown to be a good indicator of electron temperature (De Robertis et al. [52]; Keenan and McCann [10]), and the ratio $I(\lambda 7135\mathring{A})/I(\lambda 9\mu m)$ is density sensitive in the range 10^2 - 10^8 cm^{-3} (Keenan and Conlon [49]).

We see weak Ar III spectral lines from the helicon source. However, no accurate atomic data existed for this ion, with previous R-Matrix calculations also being for forbidden transitions within the $3p^4$ ground configuration [7, 8]. This chapter describes new R-Matrix excitation data that we calculated as part of this work. The results for the transitions within the $3p^4$ ground configuration are compared with the previous R-Matrix calculations, and the implications of our new data on planetary nebulae T_e and N_e diagnostics is discussed.

There has been much recent interest in improving the atomic data available for the low ion stages of argon, in particular for the excitation data that is required to model collision dominated plasmas. R-Matrix with Pseudo-States (RMPS) electron-impact excitation data was recently calculated for neutral argon (Ballance and Griffin [53]) and Ar^+ (Griffin et al. [54]). Madison et al. [55] calculated electron-impact excitation from the $3p^5 3d$ states of neutral argon using the R-Matrix method, and two first order Distorted Wave methods. For Ar^{2+}, Johnson and Kingston [7] calculated excitations within the configuration $3s^2 3p^4$ and $3s3p^5$ of Ar^{2+} using the R-Matrix method. Their results were generated in (LS) coupling and transformed to level-resolution using the JAJOM (Saraph [9]) method. Later Galavis et al. [8] also used the R-Matrix method to calculate level-resolved excitations within the $3s^2 3p^4$ configuration as part of the IRON project. They used a large configuration-interaction calculation to get the atomic structure, followed by a smaller collision calculation. Burgess et al. [5] pointed out that the $3s^2 3p^4$ (^1D) $\rightarrow$ $3s^2 3p^4$ (^1S) quadrupole effective collision strength of Galavis et al. [8] did not appear to go to the expected high energy $Born$ limit point. Galavis et al. [56] then found that including more partial waves in the calculation for this transition increased the collision strength at higher energies, making it trend closer to the expected limit point. Neither the Johnson and Kingston [7] or the Galavis et al. [8] calculations include n=4 states in their target configurations.

The aim of this chapter is to use the R-Matrix method to calculate electron-impact excitation of Ar^{2+}, including excitation up to the 5s sub-shell. This should improve upon the previous R-Matrix calculations for the first nine levels of this ion by including more resonance channels. It will also provide accurate atomic data for the excited configurations, which have not been calculated before using the R-Matrix method. With increased computational resources, R-Matrix calculations have developed from relatively small (LS) coupled calculations, to large calculations involving hundreds of levels. In order to transform from (LS) coupling, the Intermediate Coupling Frame Transformation method (ICFT) was introduced by Griffin et al. [57]. Level-resolved Breit-Pauli calculations also became feasible because of large scale parallelization of the codes, and were found to produce very similar results to the ICFT method (see Griffin et al. [57]).

The ICFT method is computationally less demanding as it requires the diagonalization of (LS)-resolved $Hamiltonians$ rather than (LSJ)-resolved $Hamiltonians$. As a large number of levels are involved in our calculation resulting in thousands of transitions, we use the ICFT calculation as a consistency check on our Breit-Pauli calculation. We also notice that fully relativistic $Dirac\ R$-Matrix calculations are also now possible for systems involving hundred of levels (see for example Ballance and Griffin [58]). We do not expect fully relativistic effects to be important for Ar^{2+}.

Coupling to the target continuum was found to be large for neutral argon excitation data, decreasing the collision strength by up to a factor of two above the ionization threshold (see Ballance and Griffin [53]). The effect was found to be smaller but still significant for Ar^+ (see Griffin et al. [54]), found up to 30% decrease in collision strength above the ionization threshold. This was shown in the previous chapter to have an observable effect on expected line intensities in our helicon plasma. We expect the effect to be small for Ar^{2+}, thus a non-pseudo states R-Matrix calculation should be sufficient. However, we examined our collision strength data above the ionization threshold for evidence of an artificial rise in the collision strength due to continuum coupling effects being omitted.

In this chapter we present results from three R-Matrix calculations. We first compare an ICFT and Breit-Pauli calculation as a check on our results. Then we show results from a Breit-Pauli calculation with the first 9 level energies shifted to NIST [22] energy values. This last calculation will then be compared with literature values, and then discuss the effect of the new data on diagnostic line ratios. In the next section we will describe the theoretical methods used. Section 7.3 will then show the results of the comparison between the different theoretical methods.

7.2 Atomic Structure Calculation and Optimization

We use the AUTOSTRUCTURE (Badnell [2]) code, a many body Breit-Pauli structure package to calculate the structure of the target used in our collision calculations. The graphical interface to AUTOSTRUCTURE GASP (Graphical Autostructure Package [3]), was used to run the AUTOSTRUCTURE code. We have included the following configurations in our calculation: $3s^2 3p^4$, $3s3p^5$, $3p^6$, $3p^5 3d$, and $3s^2 3p^3 nl$ ($3d \leqslant nl \leqslant 5s$). We found a significant improvement in the first 9 energy levels by including the $3p^5 3d$ configuration. The average percentage difference within the first 9 energy levels and those from NIST [22] was 11.16% by excluding the $3p^5 3d$ configuration, and 4.83% by including it in our structure. The same configurations were used in our scattering calculation. Our structure was optimized by using the singular value decomposition method discussed in chapter 3.4, to give best agreement with selected NIST [22] values for the level energies and line strengths. The orbitals were determined by using a $Thomas - Fermi - Dirac - Amaldi$ (TFDA) (see chapter 3.2) statistical potential in the AUTOSTRUCTURE calculation. We obtained good results from the atomic structure optimization process with a $\chi^2 = 4.13$ before the optimization, and a $\chi^2 = 0.33$ after the optimization, thus representing an improvement of 92.01% in our χ^2 value. We found that this optimization method gave us better results than AUTOSTRUCTURE's default optimization of minimization of energies, which gives a $\chi^2 = 2.07$. We also found better average percentage difference within the first 9 energy levels and those from NIST. AUTOSTRUCTURE's default optimization gives a 20.03% difference while our optimization method gives 4.83%.

7.2.1   *R*-Matrix Calculation

The scattering calculation was performed with our set of parallel R-Matrix programs (Mitnik et al. [59]; Ballance and Griffin [60]), which are extensively modified versions of the serial RMATRIX I programs of Berrington et al. [61]. In our calculation we have employed both the Breit-Pauli, and ICFT (Intermediate Coupling Frame Transformation) R-Matrix methods for electron-impact excitation (Griffin et al. [57]). The original impetus for the ICFT approach was to reduce the time consuming diagonalization of each large Breit-Pauli $Hamiltonian$. In the ICFT method, as each partial wave includes only the mass-velocity and $Darwin$ corrections to the LSΠ N+1 $Hamiltonian$, and omits the spin-orbit interaction; this greatly reduces the size of each symmetric matrix to be diagonalized. In the outer region, the resulting (LS) coupled scattering S or K-matrices are transformed to (JK) coupling by means of an algebraic transformation to provide level-to-level excitation cross-sections. This transformation involves TCCs (Term Coupling Coefficients) which are calculated from a Breit-Pauli structure calculation (including spin-orbit interaction), to express the eigenvectors for the resulting levels as linear combinations of the multi-configuration mixed terms. The coefficients of this expansion are the TCCs. With the implementation of a parallel version of our codes, and for the scale of calculations described in this section, both methods would take a similar amount of time, however the ICFT approach remains better suited for small memory serial machines and/or small parallel clusters as calculations increase in size. The consistency of results between ICFT and Breit-Pauli calculations reported later in this paper should provide a lower bound on the error we would expect in the subsequent collisional-radiative modeling. We generated effective collision strengths from our R-Matrix collision strength data via convolution with a $Maxwellian$ electron distribution (equation 4.61). We make use of Burgess-Tully plots [5] to show effective collision strengths from threshold to the infinite energy point on a single plot for the type 2 transition (see chapter 4.5.2) that we will consider. This involves the transformations given by equation (4.63), where we use a C-value of 5.0 to compare with the Burgess-Tully results shown in Galavis et al. [56].

7.2.2 Collisional-Radiative Model

We use the ADAS [11] suite of codes for our population and emission modeling. These codes are based on collisional-radiative theory, first developed by Bates et al. [1] and later generalized by Summers and Hooper [12]. The ion consists of a set of levels with radiative and collisional couplings. ionization and recombination to and from metastables of the next ionization stage (i.e. the plus ion stage) are included. The time dependence of the population (N_i) of an arbitrary level i in ion stage $+z$ is given by equation (2.1). A spectral line intensity ratio for a homogeneous plasma is evaluated via

$$\frac{I_{j \to k}^{flux}}{I_{i \to l}^{flux}} = \frac{N_j A_{j \to k}}{N_i A_{i \to l}} \tag{7.1}$$

and an energy intensity ratio is given by

$$\begin{aligned}
\frac{I_{j \to k}^{energy}}{I_{i \to l}^{energy}} &= \frac{N_j A_{j \to k} \Delta E_{jk}}{N_i A_{i \to l} \Delta E_{il}} \\
&= \frac{N_j A_{j \to k} \lambda_{il}}{N_i A_{i \to l} \lambda_{jk}}
\end{aligned} \tag{7.2}$$

When comparing with spectral line ratios observed from planetary nebulae we will use this latter equation, since the observations will be of the energy absorbed at a given wavelength.

7.3 Results

Our results can be split into three main areas: structure, collisional data, and emission modeling.

7.3.1 Atomic Structure

Our final optimized atomic structure consisted of configurations $3s^23p^4$, $3s3p^5$, $3p^6$, $3p^53d$, and $3s^23p^3nl$ ($3d \leq nl \leq 5s$), giving a total of 186 levels. Our optimized λ parameters, obtained using our singular value decomposition code are given in table 7.1. Our structure was optimized using NIST energy levels and line strengths. The level energies from our structure calculation are given in table 7.2. We show results for the first 29 levels, the remaining energies can be found in the archived data file [62]. The average percentage error between our calculated energies and the NIST energies is 3.46%. The largest error is for the $3s^23p^4$ ($^1D_2$) level. Because of the diagnostic importance of the transitions within the $3p^4$ configuration, we shift to NIST values all the energies associated with the $3p^4$ and $3s3p^5$ configurations. This will be described in the next section.

Orbital	1s	2s	2p	3s	3p	3d
λ	1.000665	1.005124	1.137871	1.191384	1.064135	1.053192
Orbital	4s	4p	4d	4f	5s	
λ	1.093229	0.916915	1.199858	0.999963	0.999797	

Table 7.1: Final λ values for the 1s-5s orbitals.

Configuration	$^{2S+1}L_J$	NIST Energy (Ryd)	Present Energy (Ryd)	%Err
$3s^23p^4$	$(^3P_2)$	0.0000	0.0000	0.0
$3s^23p^4$	$(^3P_1)$	0.0101	0.0096	5.2
$3s^23p^4$	$(^3P_0)$	0.0143	0.0137	4.4
$3s^23p^4$	$(^1D_2)$	0.1277	0.1488	16.6
$3s^23p^4$	$(^1S_0)$	0.3031	0.2841	6.2
$3s3p^5$	$(^3P_2)$	1.0370	1.0023	3.3
$3s3p^5$	$(^3P_1)$	1.0461	1.0108	3.4
$3s3p^5$	$(^3P_0)$	1.0509	1.0152	3.4
$3s3p^5$	$(^1P_1)$	1.3124	1.3028	0.7
$3p^3(4S^o)3d$	$(^5D_1)$	1.3203	1.3165	0.3
$3p^3(4S^o)3d$	$(^5D_3)$	1.3204	1.3172	0.2
$3p^3(4S^o)3d$	$(^5D_4)$	1.3205	1.3178	0.2
$3p^3(4S^o)3d$	$(^3D_3)$	1.4299	1.4536	1.7
$3p^3(4S^o)3d$	$(^3D_2)$	1.4300	1.4536	1.7
$3p^3(4S^o)3d$	$(^3D_1)$	1.4310	1.4545	1.6
$3p^3(2D^o)3d$	$(^1S_0)$	1.4749	1.5274	3.6
$3p^3(2D^o)3d$	$(^3F_2)$	1.4832	1.5015	1.2
$3p^3(2D^o)3d$	$(^3F_3)$	1.4861	1.5047	1.3
$3p^3(2D^o)3d$	$(^3F_4)$	1.4897	1.5088	1.3
$3p^3(2D^o)3d$	$(^3G_3)$	1.5683	1.5908	1.4
$3p^3(2D^o)3d$	$(^3G_4)$	1.5686	1.5915	1.5
$3p^3(2D^o)3d$	$(^3G_5)$	1.5691	1.5925	1.5
$3p^3(4S^o)4s$	$(^5S_2)$	1.5891	1.6067	1.1
$3p^3(2D^o)3d$	$(^1G_4)$	1.6008	1.6339	2.1
$3p^3(2P^o)3d$	$(^1D_2)$	1.6360	1.6380	0.1
$3p^3(4S^o)4s$	$(^3S_1)$	1.6465	1.6833	2.2
$3p^3(2P^o)3d$	$(^3F_4)$	1.6986	1.7044	0.3
$3p^3(2P^o)3d$	$(^3F_3)$	1.7010	1.7064	0.3
$3p^3(2P^o)3d$	$(^3F_2)$	1.7032	1.7084	0.3

Table 7.2: Energies in Rydbergs for the lowest 29 levels of Ar^{2+}.

As a further check on our structure, we present a selection of our calculated radiative rates in table 7.3, we show our calculated radiative rates compared with NIST [22] values and the calculations of Mendoza and Zeippen [63]. The average percentage difference between the NIST $Einstein$'s A_{jk} coefficients and ours is 65.36%. We notice that for most of the transitions the NIST uncertainty estimates on the $Einstein$'s A_{jk} coefficients are 25% or $\geq$ 50%, our $Einstein$'s A_{jk} coefficients are in general within the NIST uncertainty estimates. In the data set we use for our emission modeling the $Einstein$'s A_{jk} coefficients for transitions within the $3s^2 3p^4$ configuration will be replaced by the calculated values of Mendoza and Zeippen [63]. This will allow us to make a direct comparison with previous modeling results from the literature, highlighting the differences due to the excitation data only. However, our final archived data set will contain our calculated $Einstein$'s A_{jk} coefficients.

Initial - Final Config. Config.	Initial - Final Level Level	NIST A_{jk}	Mendoza & Zeippen [63]	Present A_{jk}
$3s3p^5 \rightarrow 3s^2 3p^4$	$^3P_1 \rightarrow {}^3P_2$	$1.59 \times 10^{+8}$		$1.16 \times 10^{+8}$
$3s3p^5 \rightarrow 3s^2 3p^4$	$^3P_0 \rightarrow {}^3P_1$	$3.74 \times 10^{+8}$		$2.78 \times 10^{+8}$
$3s3p^5 \rightarrow 3s^2 3p^4$	$^3P_2 \rightarrow {}^3P_2$	$2.79 \times 10^{+8}$		$2.08 \times 10^{+8}$
$3s3p^5 \rightarrow 3s^2 3p^4$	$^3P_1 \rightarrow {}^3P_1$	$9.20 \times 10^{+7}$		$6.95 \times 10^{+7}$
$3s3p^5 \rightarrow 3s^2 3p^4$	$^3P_1 \rightarrow {}^3P_0$	$1.22 \times 10^{+8}$		$9.21 \times 10^{+7}$
$3s3p^5 \rightarrow 3s^2 3p^4$	$^3P_2 \rightarrow {}^3P_1$	$9.00 \times 10^{+7}$		$6.90 \times 10^{+7}$
$3s^2 3p^4 \rightarrow 3s^2 3p^4$	$^1S_0 \rightarrow {}^1D_2$	9.50×10^{-1}	$2.59 \times 10^{+0}$	$2.59 \times 10^{+0}$
$3s^2 3p^4 \rightarrow 3s^2 3p^4$	$^1D_2 \rightarrow {}^3P_2$	3.48×10^{-1}	3.14×10^{-1}	1.13×10^{-1}
$3s^2 3p^4 \rightarrow 3s^2 3p^4$	$^1D_2 \rightarrow {}^3P_1$	9.64×10^{-2}	8.23×10^{-2}	8.22×10^{-2}
$3s^2 3p^4 \rightarrow 3s^2 3p^4$	$^1D_2 \rightarrow {}^3P_0$	1.25×10^{-4}	2.21×10^{-5}	2.21×10^{-5}
$3s^2 3p^4 \rightarrow 3s^2 3p^4$	$^1S_0 \rightarrow {}^3P_2$	4.30×10^{-2}	4.17×10^{-2}	4.17×10^{-2}
$3s^2 3p^4 \rightarrow 3s^2 3p^4$	$^1S_0 \rightarrow {}^3P_1$	$4.02 \times 10^{+0}$	$3.91 \times 10^{+0}$	$3.91 \times 10^{+0}$
$3s^2 3p^4 \rightarrow 3s^2 3p^4$	$^3P_0 \rightarrow {}^3P_2$	2.72×10^{-6}	2.37×10^{-6}	2.37×10^{-6}
$3s^2 3p^4 \rightarrow 3s^2 3p^4$	$^3P_1 \rightarrow {}^3P_2$	3.10×10^{-2}	3.08×10^{-2}	3.08×10^{-2}
$3s^2 3p^4 \rightarrow 3s^2 3p^4$	$^3P_0 \rightarrow {}^3P_1$	5.19×10^{-3}	5.17×10^{-3}	5.17×10^{-3}
$3p^3(^4S)4p \rightarrow 3p^3(^4S)4s$	$^5P_3 \rightarrow {}^5S_2$	$2.00 \times 10^{+8}$		$4.61 \times 10^{+8}$
$3p^3(^4S)4p \rightarrow 3p^3(^4S)4s$	$^5P_2 \rightarrow {}^5S_2$	$2.00 \times 10^{+8}$		$4.60 \times 10^{+8}$
$3p^3(^4S)4p \rightarrow 3p^3(^4S)4s$	$^5P_1 \rightarrow {}^5S_2$	$2.00 \times 10^{+8}$		$4.60 \times 10^{+8}$
$3p^3(^2D)4p \rightarrow 3p^3(^2D)4s$	$^3F_4 \rightarrow {}^3D_3$	$2.00 \times 10^{+8}$		$3.83 \times 10^{+8}$
$3p^3(^2D)4p \rightarrow 3p^3(^2D)4s$	$^3F_3 \rightarrow {}^3D_2$	$1.80 \times 10^{+8}$		$3.75 \times 10^{+8}$
$3p^3(^2D)4p \rightarrow 3p^3(^2D)4s$	$^3F_2 \rightarrow {}^3D_1$	$1.60 \times 10^{+8}$		$3.56 \times 10^{+8}$

Table 7.3: Comparisons of selected radiative rates for transitions in Ar^{2+}

7.3.2 Scattering Calculations

The orbitals used in our R-Matrix calculations were generated from the AUTOSTRUCTURE (Badnell [2]) code using the optimized λ parameters from table 7.1. Our exchange calculation included partial waves from $L = 0$ to $L = 14$ ($J = 0.5$ to $J = 11.5$ for the Breit-Pauli calculation). The non-exchange calculation went from $L = 10$ up to $L = 40$ ($J = 12.5$ to $J = 37.5$). The contributions from higher partial waves were then calculated for dipole transitions using the method originally described by Burgess [64], and for the non-dipole transitions assuming a geometric series in L, using energy ratios with special procedures for handling transitions between nearly degenerate terms. Using AUTOSTRUCTURE [2], we also calculated infinite energy Bethe/$Born$ limits, allowing us to extend the effective collision strengths and rate coefficients to temperature ranges above the highest calculated collision strength. In our outer region calculations, we used 80,000 energy mesh points over the resonance region (up to 6 Ryd), and 500 energy mesh points for the higher energies (6 Ryd to 12 Ryd).

It has been shown by Griffin et al. [57] that an ICFT calculation would produce the same results as a Breit-Pauli calculation. As a check on our calculation we performed an ICFT and a Breit-Pauli calculation using the same set of radial orbitals for both. Figure 7.1 shows the ICFT and Breit-Pauli collision strength for the $3s^2 3p^4$ ($^1P_2$) $\rightarrow$ $3s^2 3p^4$ ($^1D_2$) transition. Although small differences can be seen, the two calculations are clearly very close to each other.
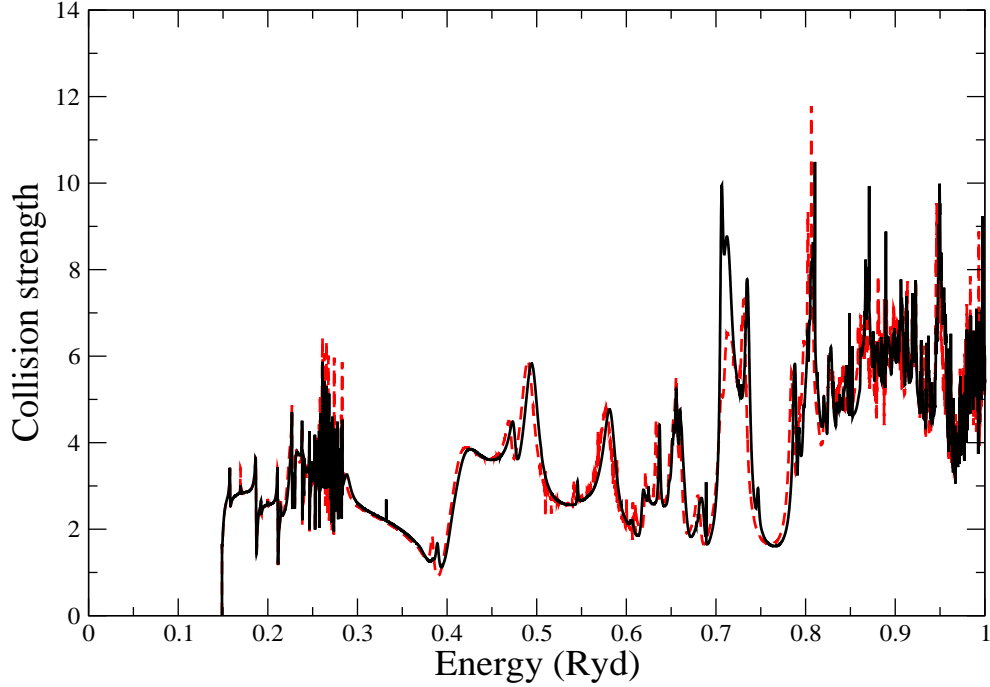
Figure 7.1: Comparison of the ICFT and Breit-Pauli collision strengths for the $3s^23p^4$ ($^1P_2$) $\rightarrow$ $3s^23p^4$ ($^1D_2$) transition. The dashed line shows the ICFT results and the solid line shows the Breit-Pauli results.

This level of agreement was typical for the collision strengths calculated. The 186 levels in our Ar^{2+} calculation give rise to 17,205 transitions. We used the scatter plot method of Witthoeft et al. [65] to compare the $Maxwellian$ effective collision strengths for all of the transitions at one time. This method takes the ratio of effective collision strengths for all transitions for a given temperature and plots this ratio against one of the effective collision strengths. Thus, a ratio of one would indicate the data sets are the same. This method also allows one to see the strength of the transitions that are in disagreement. We chose an electron temperature of 1.55 eV as one typical of planetary nebula, and low enough to strongly sample the resonance region of the collision strengths. Of the 17,205 transitions, 82% of the ICFT effective collision strengths are within 10% of the Breit-Pauli values. 94% of the ICFT effective collision strengths are within 20% of the Breit-Pauli values, and 98% are within 40%.

Of the transitions that show a difference, they are in general for weaker transitions involving highly excited levels with effective collision strengths that are extremely sensitive to the resonance contributions on top of a weak background. These transitions are not likely to make a difference in population modeling. For example, the transitions within the $3p^4$ configuration are within 4% of each other. Population modeling using the ICFT and Breit-Pauli data sets produces essentially the same excited populations for all cases we investigated. For the final data set we used the Breit-Pauli results.

To provide the most accurate data for modeling, a Breit-Pauli calculation was then done with shifts to NIST energies for the first 9 energy levels, due to their importance in spectral line diagnostics. To test the convergence of our energy mesh over the resonance region we performed a series of calculations using different meshes, namely 10,000, 20,000, 40,000 and 80,000 mesh points in the resonance region. We calculated $Maxwellian$ averaged effective collision strengths for each of these meshes and compared the files. Figure 7.2 shows a scatter plot comparison of our Breit-Pauli calculation using 40,000 and 80,000 mesh points in the resonance region. Of the 17,205 transitions, most are converged with a few outliers. There was a progression of convergence as the mesh was increased. For example, comparing calculations with 20,000 and 40,000 energy mesh points in the resonance region we found that 93.4% of the transitions were converged to within 2% of each other. Comparing the 20,000 and 40,000 energy mesh point calculations, 96.4% of the transitions were converged to within 2% of each other. Finally, comparing the 40,000 and 80,000 energy mesh point calculations, 98.4% of the transitions were converged to within 2% of each other, with 95.5% being within 1%. Thus, we believe that our 80,000 energy mesh point calculation is converged.
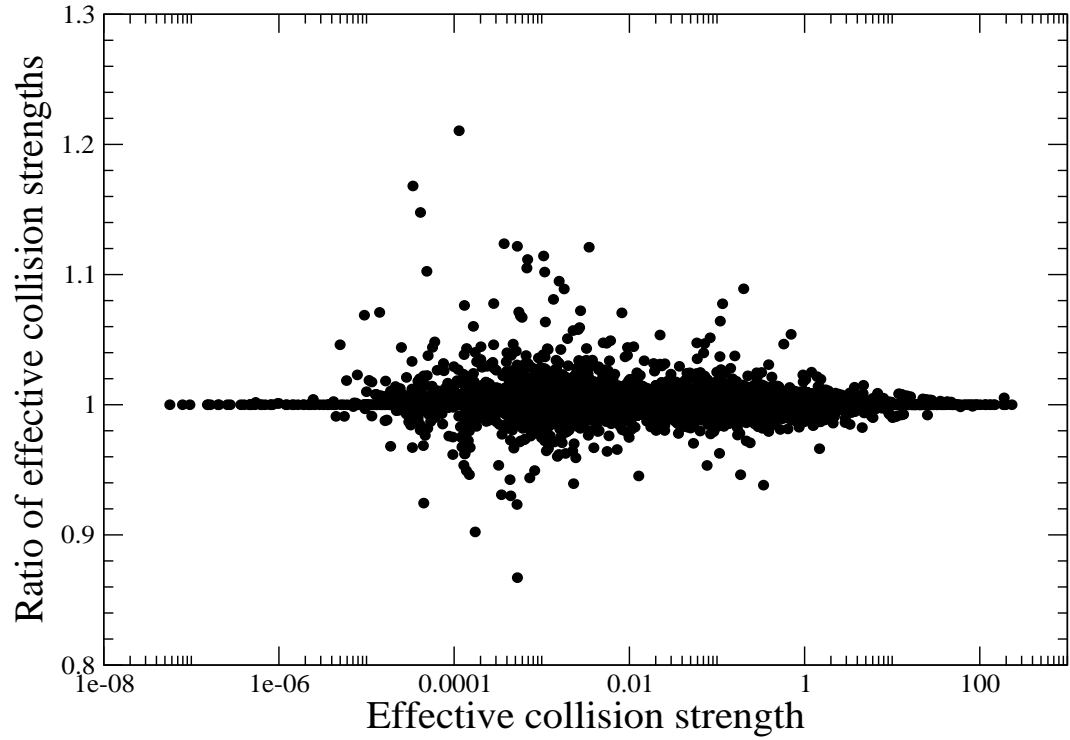
Figure 7.2: Scatter plot showing the ratio of effective collision strengths at T_e = 1.55 eV between two Breit-Pauli R-Matrix calculations. One had 40,000 energy mesh point in the resonance region, the other had 80,000 energy mesh points in the resonance region. We show the ratio of effective collision strength vs the effective collision strength of the 40,000 energy mesh calculation.

Of the previous R-Matrix calculations, we can compare with the collision strengths from Johnson and Kingston [7], see figure 7.3 for a comparison of a selection of transitions. There are clear differences in the resonance positions and heights, with the background collision strengths being in good agreement. The differences in the resonance contributions may be due to the well known problems with the JAJOM method (Griffin et al. [57]) that was used by Johnson and Kingston [7] to transform the (LS) results to (LSJ) resolution.
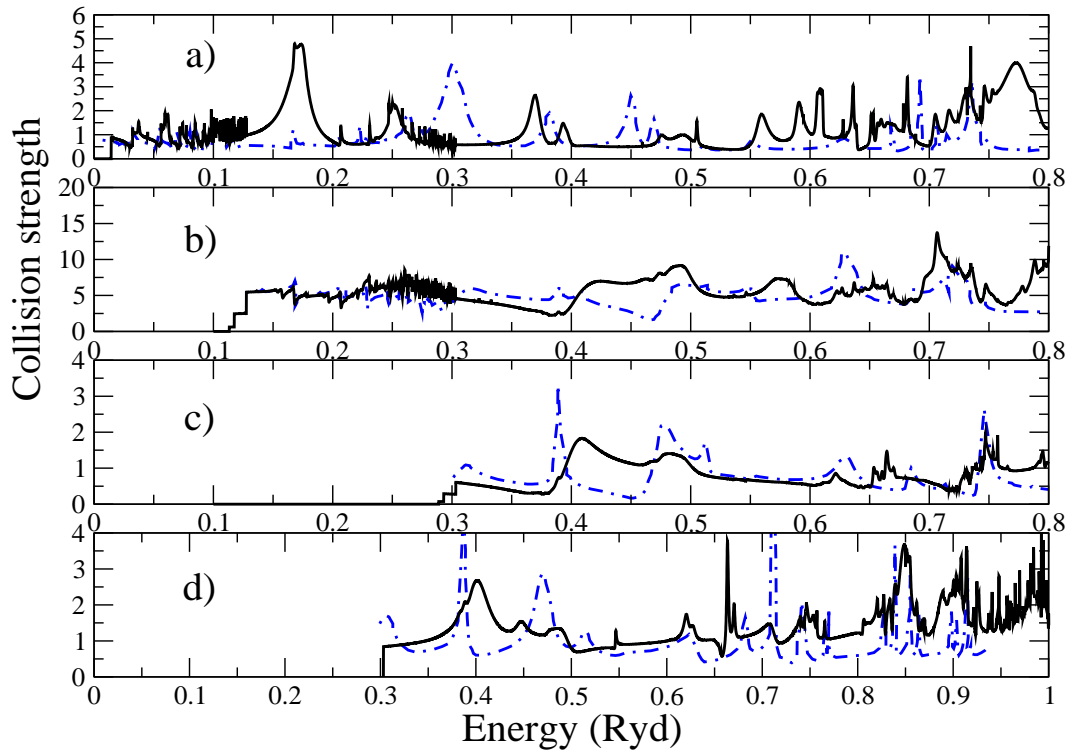
Figure 7.3: Comparison of selected Breit-Pauli collision strengths (with energy shifts included for the first 9 energy levels) with Johnson and Kingston [7]. Plot a) shows the $3p^4$ ($^3P_2$) $\rightarrow 3p^4$ ($^3P_0$) transition. Plot b) shows the $3p^4$ (^3P) $\rightarrow 3p^4$ (^1D) transition, where the level-resolved Breit-Pauli collision strengths have been summed to give the term-resolved collision strength. Plot c) shows the $3p^4$ (^3P) $\rightarrow 3p^4$ (^1S) transition, where the level-resolved Breit-Pauli collision strengths have been summed to give the term-resolved collision strength. Plot d) shows the $3p^4$ ($^1D_2$) $\rightarrow 3p^4$ ($^1S_0$) transition. In all plots the solid line shows the Breit-Pauli results and the dot-dashed line shows the Results of Johnson and Kingston [7].

We can compare our effective collision strength results with the IRON project data of Galavis et al. [8], and with the tabulated values of Johnson and Kingston [7]. Figure 7.4 shows the comparison for a selection of transitions. Table 7.4 shows our calculated effective collision strengths for transitions between the $3s^2 3p^4$ levels.

Temperature (K)	$^3P_1$ - $^3P_2$	$^3P_0$ - $^3P_2$	$^1D_2$ - $^3P_2$	$^1S_0$ - $^3P_2$	$^3P_0$ - $^3P_1$
1800	3.860	0.808	3.010	0.307	1.410
4500	3.820	0.866	2.970	0.299	1.420
9000	4.030	0.990	2.940	0.354	1.420
18000	4.210	1.100	2.930	0.421	1.380
45000	4.260	1.160	3.090	0.478	1.320
90000	4.310	1.200	3.080	0.467	1.290
180000	3.820	1.080	2.570	0.378	1.100
450000	2.660	0.791	1.570	0.223	0.693
900000	1.930	0.617	0.958	0.133	0.433
1800000	1.480	0.515	0.556	0.074	0.254
4500000	1.180	0.458	0.261	0.033	0.118
9000000	1.080	0.445	0.148	0.018	0.064
18000000	1.030	0.442	0.085	0.009	0.034
Temperature (K)	$^1D_2$ - $^3P_1$	$^1S_0$ - $^3P_1$	$^1D_2$ - $^3P_0$	$^1S_0$ - $^3P_0$	$^1S_0$ - $^1D_2$
1800	1.850	0.202	0.622	0.069	0.871
4500	1.820	0.192	0.612	0.065	0.995
9000	1.800	0.217	0.602	0.072	1.160
18000	1.780	0.257	0.595	0.085	1.240
45000	1.870	0.302	0.625	0.105	1.340
90000	1.860	0.301	0.621	0.108	1.440
180000	1.550	0.245	0.516	0.089	1.450
450000	0.945	0.145	0.315	0.053	1.380
900000	0.578	0.086	0.193	0.031	1.370
1800000	0.334	0.048	0.112	0.017	1.410
4500000	0.155	0.021	0.052	0.008	1.510
9000000	0.085	0.011	0.029	0.004	1.570
18000000	0.047	0.005	0.016	0.002	1.630

Table 7.4: Effective collision strengths for transitions between the $3s^2 3p^4$ levels.

At the highest temperatures, our effective collision strengths are consistently higher than the previous calculations. Since we have a similar background cross-section, the differences are due to the extra resonance channels included in our calculation, and to a lesser extent differences in our top-up procedures. Most transitions show differences at low temperatures where sensitivity to the low energy resonance contribution is strongest. This is particularly true for the transitions $3p^4$ ($^3P_2$) $\rightarrow 3p^4$ ($^1S_0$), and $3p^4$ ($^1D_2$) $\rightarrow 3p^4$ ($^1S_0$), shown in figure 7.4 e & f.
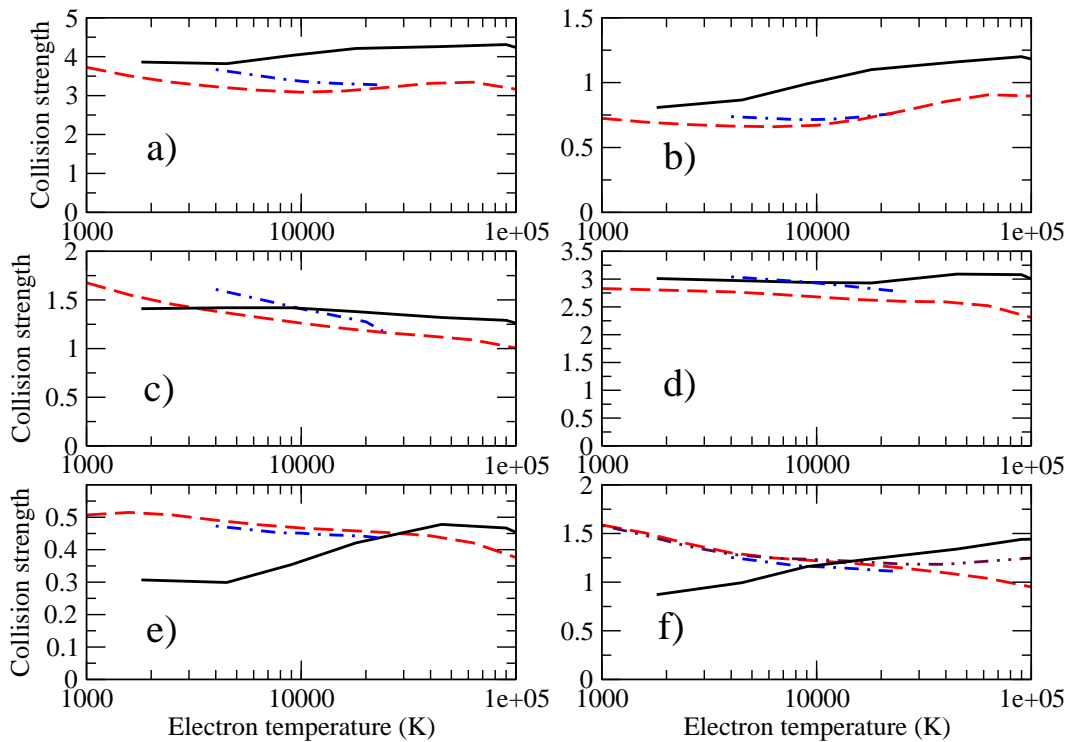
Figure 7.4: Comparison of selected Breit-Pauli effective collision strengths (with energy shifts included for the first 9 energy levels) with Johnson and Kingston [7] and with Galavis et al. [8, 56]. Plot a) shows the $3p^4$ ($^3P_2$) $\rightarrow 3p^4$ ($^3P_1$) transition. Plot b) shows the $3p^4$ ($^3P_2$) $\rightarrow 3p^4$ ($^3P_0$) transition. Plot c) shows the $3p^4$ ($^3P_1$) $\rightarrow 3p^4$ ($^3P_0$) transition. Plot d) shows the $3p^4$ ($^3P_2$) $\rightarrow 3p^4$ ($^1D_2$) transition. Plot e) shows the $3p^4$ ($^3P_2$) $\rightarrow 3p^4$ ($^1S_0$) transition. Plot f) shows the $3p^4$ ($^1D_2$) $\rightarrow 3p^4$ ($^1S_0$) transition. In all plots the solid line shows the Breit-Pauli R-Matrix results, the dashed line shows the results of Galavis et al. [8], and the dot-dashed line shows the results of Johnson and Kingston [7]. In plot f) the double-dot dashed line shows the results of Galavis et al. [56].

In both cases our effective collision strengths are smaller than previous calculations at the lowest temperatures. This is most likely due to the contributions from near threshold resonances. For example, the $3p^4$ ($^1D_2$) $\rightarrow$ $3p^4$ ($^1S_0$) transition has contribution due to a reported $3s3p^5(^3P)3d$ (^2P) resonance that occurs at the excitation threshold in the previous R-Matrix calculations of Johnson and Kingston [7]. Galavis et al. [8] also point out the large contribution from a near threshold resonance in their calculation of this transition. The near threshold resonance in the $3p^4$ (^3P) $\rightarrow$ $3p^4$ (^1S) transition is likely to be due to the same resonance. We do not see this near threshold resonance in our calculations for either of these transitions. As will be seen later, these two transitions are key for spectral diagnostics. Thus, we performed a smaller R-Matrix calculation, using the same configurations as Johnson and Kingston [7]. In this calculation we do see a near threshold resonance in the $3p^4$ ($^1D_2$) $\rightarrow$ $3p^4$ ($^1S_0$) transition, as seen in previous work. We identified the resonances as belonging to the $J = 3/2$ partial wave. Investigation of the eigenphase sum shows that this broad resonance belongs to the $3s3p^53d$ configuration, and is shifted to lower energy in our larger Breit-Pauli calculation. Thus it does not contribute to our collision strength. Our resonance position should be more accurate, due to the larger number of configurations in our structure calculation. However, this resonance is very close to the excitation threshold and is clearly sensitive to configuration interaction effects. Experimental measurements of this collision strength would be very useful.

At higher temperatures for the $3p^4$ ($^1D_2$) $\rightarrow$ $3p^4$ ($^1S_0$) transition we verify the findings of Burgess et al. [5] and Galavis et al. [56], that contributions from higher partial waves are required for the effective collision strength to tend to the right limit point. We plot our results for this transition in a Burgess-Tully plot in figure 7.5 to highlight the high energy behaviour. Our results go to a limit point of 1.72, close to the value of 1.68 expected by Burgess et al. [5]. As pointed out by Galavis et al. [56], the rise in slope of the Burgess-Tully plot towards the limit point does not happen until relatively close to the limit point.
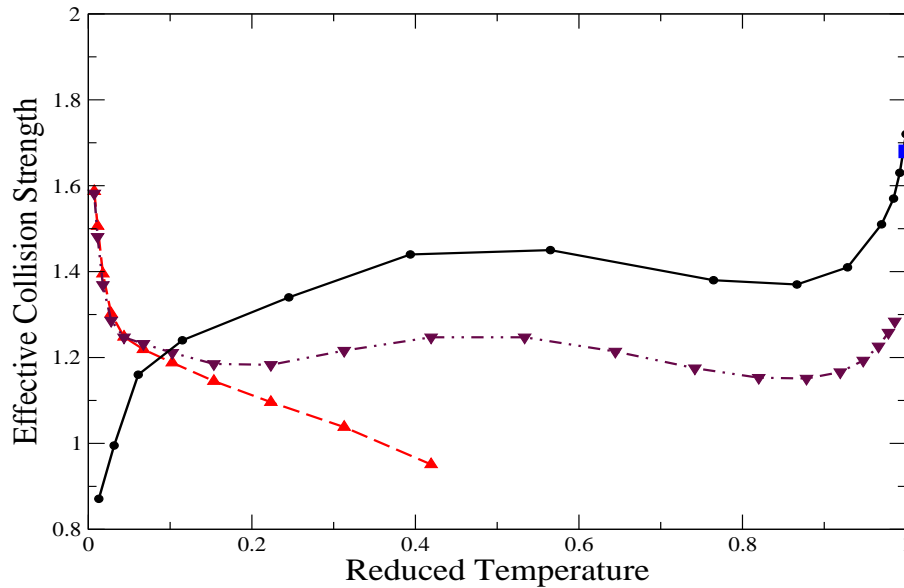
Figure 7.5: Burgess Tully plot of effective collision strength vs reduced temperature (X). Results are shown for transition $3p^4$ ($^1D_2$) $\rightarrow$ $3p^4$ ($^1S_0$). In the reduced temperature scale zero corresponds to the value at threshold and one corresponds to the value at the infinite energy point. The solid line shows the results from our Breit-Pauli R-Matrix calculation, the dashed line shows the results from the R-Matrix calculation of Galavis et al. [8], and the double-dot dashed line shows the results of Galavis et al. [56] where more partial waves were included compared to their previous calculation. The solid square shows the limit point of Burgess et al. [5]

7.3.3   Emission Modeling

Our Breit-Pauli atomic data set was used to model commonly observed forbidden transitions of Ar III. Our modeling data consists of the Breit-Pauli excitation data, including shifts to NIST energies for the first 9 levels. Our dipole $Einstein$'s A_{jk} coefficients were evaluated in our R-Matrix calculation. Our non-dipole $Einstein$'s A_{jk} coefficients came from an AUTOSTRUCTURE calculation. For the purpose of the modeling work in this paper we use the same $Einstein$'s A_{jk} coefficients for transitions within the $3p^4$ configuration as those of Mendoza and Zeippen [63]. These were the $Einstein$'s A_{jk} coefficients used in previous emission models using R-Matrix data from Keenan and McCann [10], and Keenan and Conlon [49]. Using the same $Einstein$'s A_{jk} coefficients will allow us to highlight differences in emission modeling due to the excitation collision data. The final set of data that is available online will include our computed $Einstein$'s A_{jk} coefficients for all the transitions. We first consider the temperature sensitive energy intensity ratio

$$R_1 = I^{energy}(\lambda 7135 \mathring{A} + \lambda 7751 \mathring{A})/I^{energy}(\lambda 5192 \mathring{A})$$
$$= \frac{(N_5 A_{5 \to 1}/\lambda_{7135}) + (N_4 A_{4 \to 1}/\lambda_{7751})}{N_5 A_{5 \to 4}/\lambda_{5192}}. \tag{7.3}$$

where the numbers in the subscripts of N and A denote the index numbers of the energy levels involved in the transitions. The ratio is insensitive to electron density up to $N_e \sim 1 \times 10^5$ cm^{-3}. Our results are shown in figure 7.6. We also calculated this ratio using the data of Johnson and Kingston [7] and the data of Galavis et al. [8], where we used $Einstein$'s A_{jk} coefficients from Mendoza and Zeippen [63] for the radiative rates. We notice that the ratio we calculate for the Johnson and Kingston [7] data is equivalent to that shown by Keenan and McCann [10].

Our R_1 ratio is close to that obtained from the two previous R-Matrix calculations. The excited populations are coronal at low densities and are only sensitive to excitation rate coefficients from the ground to the $3p^4$ ($^1S_0$) level, excitation from the ground to $3p^4$ ($^1D_2$) level, and radiative decay from the $3p^4$ ($^1S_0$) and $3p^4$ ($^1D_2$) levels. Since we use the same $Einstein$'s A_{jk} coefficients in all of our calculations, the differences in our ratio are primarily because our effective collision strength for $3p^4$ ($^3P_2$) $\rightarrow$ $3p^4$ ($^1S_0$) is smaller than archived data, due to differences in low energy resonance contributions. Our new R-Matrix data does not make a large difference to the temperatures diagnosed from measured line ratios. Our diagnosed temperatures are within 10% of those diagnosed using the older R-Matrix data sets.
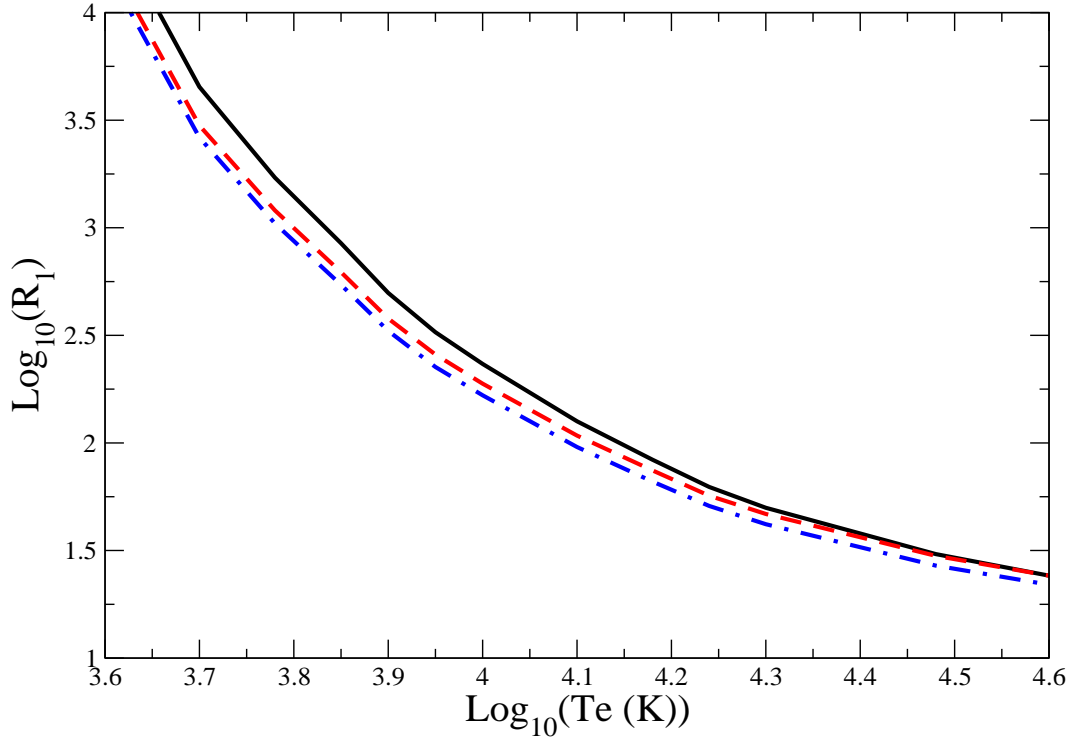
Figure 7.6: R_1 line ratio as a function of electron temperature. The results are calculated at $N_e = 1 \times 10^3$ cm^{-3}, though the results are insensitive to electron density up to $N_e = 1 \times 10^5$ cm^{-3}. The solid line shows the results using the new R-Matrix Breit-Pauli collision data. The dot-dashed line show the results using the data of Johnson and Kingston [7] and the dashed line shows the results using the data of Galavis et al. [8].

Figure 7.7 shows the results for the density sensitive energy intensity ratio
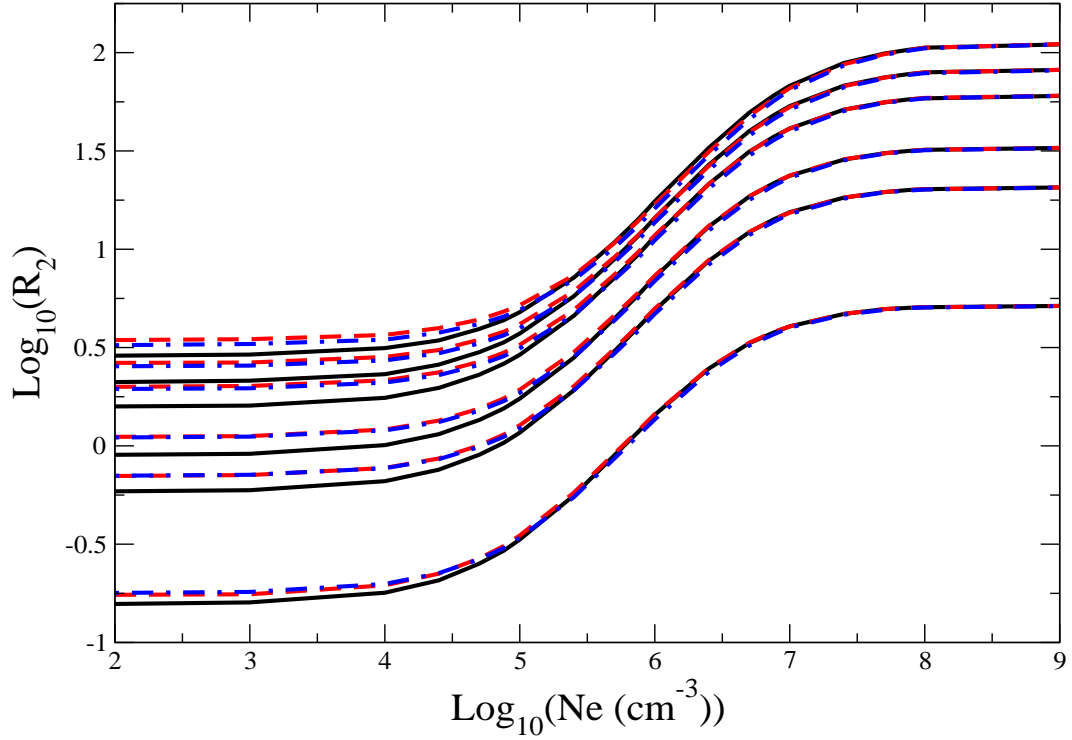
Figure 7.7: R_2 line ratio as a function of electron density. The results are calculated for a range of electron temperatures, namely 5,000, 8,000, 10,000, 15,000, 20,000 and 30,000K. The lowest line ratio is the 5,000K results, with the higher ratios showing the progressively higher temperature results. The solid line shows the results using the new R-Matrix Breit-Pauli collision data. The dot-dashed line show the results using the data of Johnson and Kingston [7] and the dashed line shows the results using the data of Galavis et al. [8].

$$R_2 = I^{energy}(\lambda 7135\text{Å})/I^{energy}(\lambda 9\mu m)$$

$$= \frac{N_4 A_{4\rightarrow 1}/\lambda_{7135}}{N_2 A_{2\rightarrow 1}/\lambda_{90000}} \tag{7.4}$$

We again compare with calculations using the data of Johnson and Kingston [7] and the data of Galavis et al. [8]. The modeling using the Johnson and Kingston data is equivalent to the ratio shown in Keenan and Conlon [49]. For each temperature we see that all the R_2 ratios go from the coronal value at low densities to the local thermodynamic equilibrium value by $N_e \sim 1 \times 10^8$ cm^{-3}. Our ratios are consistently lower than those from the previous R-Matrix calculations. This is primarily due to our collisional excitation rate from the ground to the $3p^4$ ($^1S_0$) being smaller than those from the previous calculations. Our new data makes a significant difference to electron densities diagnosed using the above line ratio. For example, the line ratio for planetary nebula NGC 6572 shown in Keenan and Conlon [49] is 0.23 and is for an electron temperature of 10,000K.

The new R-Matrix data gives a value of $\log_{10}(N_e) = 4.98$ ($N_e = 9.46 \times 10^4$ cm^{-3}) compared with the value given by Keenan and Conlon using the data of Johnson and Kingston [7] of $\log_{10}(N_e) = 4.7$ ($N_e = 5.0 \times 10^4$ cm^{-3}). We found that cascades from higher levels do not affect either the R_1 or R_2 line ratios. Measurement of the excitation cross-sections for these forbidden transitions of Ar^{2+} would be very useful, especially measurements that could determine if there is a near threshold resonance in the $3p^4$ ($^1D_2$) $\rightarrow 3p^4$ ($^1S_0$) and $3p^4$ (^3P) $\rightarrow 3p^4(^1S)$ transitions. Our R-Matrix data also includes excitations up to excited configurations. We do not show any modeling results for transitions involving these configurations. We expect this data to be of high quality and intend to use the data to model Ar III spectra in the future.

Our final data set is archived online at the Oak Ridge atomic data center [62] and in the ADAS database [11]. Tables 7.2, 7.3, and 7.4 are only available in electronic form at the CDS [66].

CHAPTER 8

NE MODELING AND EXPERIMENT

8.1 Introduction

Emission modeling of Ne plasmas have important applications in plasma processing [67], astrophysics [68], and lasers [69]. It is also an important tool for non-invasive plasma diagnostics [70], and in studies of radiative disruption mitigation in TOKAMAKS. We first model spectral emission of neon using Plane Wave $Born$ (see chapter 4.2) electron-impact excitation data available in the ADAS [11] database, and calculated by Martin O'Mullane. This is the data most commonly used in current fusion modeling on neon spectral emission. We then present preliminary results of emission modeling using recent RMPS (LS), and R-Matrix (IC) electron-impact excitation data calculated by Griffin and Ballace [71]. We compare these calculations with other R-Matrix calculation by Zatsarinny and Bartschat [72]. Zatsarinny and Bartschat [72] calculated electron-impact excitation cross-sections, but did not calculate collision strengths data that we could use to generate effective collision strengths for emission modeling. Thus, we developed the OMEGA fortran code, which reads the electron-impact excitation cross-section files and the file containing the energy levels, and computes collision strengths which are stored in a generic R-Matrix OMEGA file. This output file can be used to calculate $Maxwellian$ effective collision strengths that we use to calculate spectral line emission. This code will also allow us to convert future atomic data sets generated by Zatsarinny and Bartschat into ADAS [11] data files that can be used for spectral modeling.

8.2 Atomic Data Comparison

In order to accurately compare the different sets of electron-impact excitation data, we first focus on comparing the different atomic structures used for the computation of these collision data sets. We focus mainly in the first 12 lower levels, since all the spectral lines we are modeling originate from these levels. The purpose of comparing the structure first is mainly to eliminate the possibilities that differences in the collision data sets are caused by differences in atomic structure. After comparing the atomic structures, we then proceed to compare the available electron-impact exctation cross-sections from transitions from the ground and metastables. We compare some electron-impact excitation cross-sections from the ground level $2p^6$ ($^1S_0$) with Chilton's et al. [73] experimental data, and some electron-impact excitation cross-sections from one of the metastable levels $2p^5 3s\ ^2[3/2]_2^o$ ($^3P_2$) with Boffard et al. [74] experimental data. These sets of experimental data will give us an idea of the quality of the collision data. At this point we can compare the emission line intensity generated by each of these data sets against ASTRAL measurements.

8.2.1 Atomic Structure Comparison

To give us an indication of the quality of the atomic data, we make use of the NIST [22] atomic (level/term) energies to compare the atomic structures. We first compare O'Mullane's [11] atomic structure used in his Plane Wave $Born$ electron-impact excitation calculation. O'Mullane made use of the Cowan Atomic Structure Program [20] to calculate the atomic structure. The structure calculation included configurations $1s^2 2s^2 2p^6$ and $1s^2 2s^2 2p^5 nl$, with nl = 3s, 3p, and 3d, thus calculating atomic collision data for the first 27 levels of neon. Table 8.1 shows the comparison of the energies for the first 12 levels of neon used by O'Mullane with those given by NIST [22].

Lev. (#)	NIST En.(Ryd)	Present En.(Ryd)	Diff. (%)	Configuration	Term Mixing $^{2S+1}L_J$ (%)
1	0.0000000	0.0000000	0.0000	$2p^6$	$^1S_0$ (1.00)
2	1.2214791	1.2214970	0.0015	$2p^5 3s\ ^2[3/2]^o_2$	$^3P_2$ (1.00)
3	1.2252832	1.2253006	0.0014	$2p^5 3s\ ^2[3/2]^o_1$	$^3P_1$ (0.33) $^1P_1$ (0.67)
4	1.2285579	1.2285757	0.0015	$2p^5 3s\ ^2[1/2]^o_0$	$^3P_0$ (1.00)
5	1.2383091	1.2383272	0.0015	$2p^5 3s\ ^2[1/2]^o_1$	$^1P_1$ (0.33) $^3P_1$ (0.67)
6	1.3510244	1.3510418	0.0013	$2p^5 3p\ ^2[1/2]_1$	$^3S_1$ (0.67) $^3P_1$ (0.22) $^1P_1$ (0.11)
7	1.3637753	1.3637932	0.0013	$2p^5 3p\ ^2[5/2]_3$	$^3D_3$ (1.00)
8	1.3652988	1.3653168	0.0013	$2p^5 3p\ ^2[5/2]_2$	$^3D_2$ (0.40) $^1D_2$ (0.60)
9	1.3680086	1.3680269	0.0013	$2p^5 3p\ ^2[3/2]_1$	$^3D_1$ (0.17) $^1P_1$ (0.56) $^3P_1$ (0.28)
10	1.3697789	1.3697966	0.0013	$2p^5 3p\ ^2[3/2]_2$	$^3P_2$ (0.83) $^3D_2$ (0.10) $^1D_2$ (0.07)
11	1.3739366	1.3739547	0.0013	$2p^5 3p\ ^2[3/2]_1$	$^1P_1$ (0.11) $^3D_1$ (0.83) $^3P_1$ (0.06)
12	1.3747239	1.3747420	0.0013	$2p^5 3p\ ^2[3/2]_2$	$^1D_2$ (0.33) $^3D_2$ (0.50) $^3P_2$ (0.17)

Table 8.1: Energies in $Rydbergs$ for the lowest 12 levels of Ne used by O'Mullane Plane Wave $Born$ (IC) resolved calculation [11].

O'Mullane replaced the energy levels from his calculation for those of C. E. Moore [75], thus making the atomic structure comparison more difficult. As shown in section 4.2, the Plane Wave $Born$ it is not accurate for near neutral systems, and much less for low energy incident electrons, thus making the modeling for low temperatures not as accurate. In order to improve the quality of the collision data, O'Mullane took several effective collision strengths from the ground $2p^6$ (^1S) state to the $2p^5 3s$ and $2p^5 3p$ levels using theoretical data from Zeman and Bartschat [76], and experimental data from Tsurubuchi et al. [77], Machado et al. [78], and Chilton et al. [73].

The last column in table 8.1 (and in subsequent tables) shows the term mixing coefficients from the other terms within the given configuration. This is provided purely as a guide for later spectral modeling, and to allow us to predict which transitions are most likely to affect the measured spectral lines. Notice that (LS) coupling notation is not appropriate for neutral neon, and that (JK) coupling notation is more appropriate. O'Mullane also replaced some of the $Einstein$'s A_{jk} coefficients with Del Val's et al. [79] experimental values. The $Einstein$'s A_{jk} coefficients for transitions to the ground (see table 8.5) used to compare the atomic structure with those from the other calculations were not replaced by experimental values.

Zatsarinny and Bartschat [72] calculated semi-relativistic Breit-Pauli R-Matrix (IC) resolved electron-impact excitation data, with a variety of non-orthogonal valence orbitals, thus getting good results in their atomic structure calculation. They closely coupled the lowest 31 physical fine-structure states of neon. The structure calculation included configurations $1s^2 2s^2 2p^6$ and $1s^2 2s^2 2p^5 nl$, with nl = 3s, 3p, 3d, and 4s. Table 8.2 shows the comparison of the energies for the first 12 levels of neon used by Zatsarinny and Bartschat with those from NIST [22].

Lev. (#)	NIST En.(Ryd)	Present En.(Ryd)	Diff. (%)	Configuration	Term Mixing $^{2S+1}L_J$ (%)
1	0.0000000	0.0000000	0.0000	$2p^6$	$^1S_0$ (1.00)
2	1.2214791	1.2289803	0.6141	$2p^5 3s\ ^2[3/2]^o_2$	$^3P_2$ (1.00)
3	1.2252832	1.2329990	0.6297	$2p^5 3s\ ^2[3/2]^o_1$	$^3P_1$ (0.33) $^1P_1$ (0.67)
4	1.2285579	1.2363798	0.6367	$2p^5 3s\ ^2[1/2]^o_0$	$^3P_0$ (1.00)
5	1.2383091	1.2472877	0.7251	$2p^5 3s\ ^2[1/2]^o_1$	$^1P_1$ (0.33) $^3P_1$ (0.67)
6	1.3510244	1.3598929	0.6564	$2p^5 3p\ ^2[1/2]_1$	$^3S_1$ (0.67) $^3P_1$ (0.22) $^1P_1$ (0.11)
7	1.3637753	1.3715298	0.5686	$2p^5 3p\ ^2[5/2]_3$	$^3D_3$ (1.00)
8	1.3652988	1.3730152	0.5652	$2p^5 3p\ ^2[5/2]_2$	$^1D_2$ (0.60) $^3D_2$ (0.40)
9	1.3680086	1.3759403	0.5798	$2p^5 3p\ ^2[3/2]_1$	$^1P_1$ (0.56) $^3D_1$ (0.17) $^3P_1$ (0.28)
10	1.3697789	1.3775168	0.5649	$2p^5 3p\ ^2[3/2]_2$	$^3P_2$ (0.83) $^3D_2$ (0.10) $^1D_2$ (0.07)
11	1.3739366	1.3821370	0.5969	$2p^5 3p\ ^2[3/2]_1$	$^3D_1$ (0.83) $^1P_1$ (0.11) $^3P_1$ (0.06)
12	1.3747239	1.3828204	0.5890	$2p^5 3p\ ^2[3/2]_2$	$^3D_2$ (0.50) $^1D_2$ (0.33) $^3P_2$ (0.17)

Table 8.2: Energies in $Rydbergs$ for the lowest 12 levels of Ne used by Zatsarinny and Bartschat R-Matrix (IC) resolved calculation [72].

We clearly see that the atomic structure calculation appears to be very accurate when comparing with the NIST [22] energy values.

We now compare a small atomic structure used by Griffin and Ballance R-Matrix electron-impact excitation calculation [71]. Griffin and Connor made use of Badnell's Autostrucure Atomic Structure Program [2] to calculate the atomic structure. The structure calculation included configurations $1s^2 2s^2 2p^6$ and $1s^2 2s^2 2p^5 nl$, with nl values given from 3s to 5p, thus calculating atomic collision data for the first 79 spectroscopic levels of neon. Table 8.3 shows the comparison of the energies for the first 12 levels of neon used by Griffin and Ballance with those given by NIST [22].

Lev. (#)	NIST En.(Ryd)	Present En.(Ryd)	Diff. (%)	Configuration	Term Mixing $^{2S+1}L_J$ (%)
1	0.0000000	0.0000000	0.0000	$2p^6$	$^1S_0$ (1.00)
2	1.2214791	1.2209323	0.0448	$2p^5 3s\ ^2[3/2]^o_2$	$^3P_2$ (1.00)
3	1.2252832	1.2258087	0.0429	$2p^5 3s\ ^2[3/2]^o_1$	$^3P_1$ (0.33) $^1P_1$ (0.67)
4	1.2285579	1.2296808	0.0914	$2p^5 3s\ ^2[1/2]^o_0$	$^3P_0$ (1.00)
5	1.2383091	1.2445165	0.5013	$2p^5 3s\ ^2[1/2]^o_1$	$^1P_1$ (0.33) $^3P_1$ (0.67)
6	1.3510244	1.3503765	0.0480	$2p^5 3p\ ^2[1/2]_1$	$^3S_1$ (0.67) $^3P_1$ (0.22) $^1P_1$ (0.11)
7	1.3752608	1.3750601	0.0146	$2p^5 3p\ ^2[1/2]_0$	$^3P_0$ (0.33) $^1S_0$ (0.67)
8	1.3637753	1.3614090	0.1735	$2p^5 3p\ ^2[5/2]_3$	$^3D_3$ (1.00)
9	1.3652988	1.3633233	0.1447	$2p^5 3p\ ^2[5/2]_2$	$^3D_2$ (0.40) $^1D_2$ (0.60)
10	1.3680086	1.3663496	0.1213	$2p^5 3p\ ^2[3/2]_1$	$^3D_1$ (0.17) $^1P_1$ (0.56) $^3P_1$ (0.28)
11	1.3697789	1.3685350	0.0908	$2p^5 3p\ ^2[3/2]_2$	$^3P_2$ (0.83) $^3D_2$ (0.10) $^1D_2$ (0.07)
12	1.3739366	1.3733009	0.0463	$2p^5 3p\ ^2[3/2]_1$	$^1P_1$ (0.11) $^3D_1$ (0.83) $^3P_1$ (0.06)

Table 8.3: Energies in $Rydbergs$ for the lowest 12 levels of Ne used by Griffin and Ballance R-Matrix (IC) resolved calculation [71].

The atomic structure also shows good agreement with the energy values given by NIST [22].

We now compare the structure for Griffin and Ballance largest RMPS (LS) coupling calculation [71]. The structure calculation was also performed by means of Badnell's Autostrucure Atomic Structure Program [2]. The structure calculation included configurations $1s^2 2s^2 2p^6$ and $1s^2 2s^2 2p^5 nl$, with nl values given from 3s to 5p. They also employed $\bar{n}l$ pseudo-orbitals to generate pseudo-states for the configurations: $2p^5 \bar{5}d$; $2p^5 \bar{5}f$; $2p^5 \bar{n}l$, with $\bar{n}$=6 through $\bar{n}$=14 and l=0 to l=4. This leads to a total of 560 levels (247 terms), 79 which are spectroscopic. Table 8.4 shows the comparison of the energies for the first 12 levels (6 terms) of neon used by Griffin and Ballance with those given by NIST [22]. Griffin and Ballance [71] collision calculation was performed in (LS) coupling, but in order to be able to compare the atomic structures we computed the energies in (IC) coupling, as well as in (LS) coupling as shown in table 8.4.

Lev. (#)	NIST En.(Ryd)	Present En.(Ryd)	Diff. (%)	Configuration	Term Mixing $^{2S+1}L_J$ (%)
1	0.0000000	0.0000000	0.0000	$2p^6$	$^1S_0$ (1.00)
2	1.2214791	1.2248912	0.2793	$2p^5 3s\ ^2[3/2]^o_2$	$^3P_2$ (1.00)
3	1.2252832	1.2298209	0.3703	$2p^5 3s\ ^2[3/2]^o_1$	$^3P_1$ (0.33) $^1P_1$ (0.67)
4	1.2285579	1.2338094	0.4275	$2p^5 3s\ ^2[1/2]^o_0$	$^3P_0$ (1.00)
5	1.2383091	1.2482131	0.7998	$2p^5 3s\ ^2[1/2]^o_1$	$^1P_1$ (0.33) $^3P_1$ (0.67)
6	1.3510244	1.3539154	0.2140	$2p^5 3p\ ^2[1/2]_1$	$^3S_1$ (0.67) $^3P_1$ (0.22) $^1P_1$ (0.11)
7	1.3752608	1.3792162	0.2876	$2p^5 3p\ ^2[1/2]_0$	$^3P_0$ (0.33) $^1S_0$ (0.67)
8	1.3637753	1.3658580	0.1527	$2p^5 3p\ ^2[5/2]_3$	$^3D_3$ (1.00)
9	1.3652988	1.3677551	0.1799	$2p^5 3p\ ^2[5/2]_2$	$^3D_2$ (0.40) $^1D_2$ (0.60)
10	1.3680086	1.3708331	0.2065	$2p^5 3p\ ^2[3/2]_1$	$^3D_1$ (0.17) $^1P_1$ (0.56) $^3P_1$ (0.28)
11	1.3697789	1.3728800	0.2264	$2p^5 3p\ ^2[3/2]_2$	$^3P_2$ (0.83) $^3D_2$ (0.10) $^1D_2$ (0.07)
12	1.3739366	1.3778515	0.2849	$2p^5 3p\ ^2[3/2]_1$	$^1P_1$ (0.11) $^3D_1$ (0.83) $^3P_1$ (0.06)
Term (#)	NIST En.(Ryd)	Present En.(Ryd)	Diff. (%)	Configuration	Term Mixing ^{2S+1}L (%)
1	0.0000000	0.0000000	0.0000	$2p^6$	^1S (1.00)
2	1.2229056	1.2278530	0.4046	$2p^5 3s\ ^2[3/2]^o$	^3P (0.33) ^1P (0.67)
3	1.2358713	1.2471870	0.9156	$2p^5 3s\ ^2[1/2]^o$	^1P (0.33) ^3P (0.67)
4	1.3570835	1.4003430	3.1877	$2p^5 3p\ ^2[1/2]$	^1S (0.67) ^3P (0.33)
5	1.3644101	1.3687710	0.3196	$2p^5 3p\ ^2[5/2]$	^3D (0.40) ^1D (0.60)
6	1.3691151	1.3739110	0.3503	$2p^5 3p\ ^2[3/2]$	^1D (0.07) ^3P (0.83) ^3D (0.10)

Table 8.4: Energies in $Rydbergs$ for the lowest 12 levels of Ne used by Griffin and Ballance RMPS (LS) resolved calculation [71].

We see that the agreement is still very good for all of the different calculations.

Having compared the atomic structures for the different sets of calculations, we now compare the $Einstein$'s A_{jk} coefficients for dipole transitions 3s $^2[1/2]_1^o$ ($^1P_1$) and 3s $^2[3/2]_1^o$ ($^3P_1$) to the ground level $2p^6$ ($^1S_0$). These two levels also correspond to transitions between terms that have a single level, and thus allow us to compare the (IC) coupling results with the (LS) data from Griffin and Ballance [71]. Table 8.5 shows the values of the $Einstein$'s A_{jk} coefficients for these two transitions

$(i) \longrightarrow (j)$ Initial Final Level Level	$A_{i \to j}$ Plane Wave $Born$ [11]	$A_{i \to j}$ R-Matrix (IC) [72]	$A_{i \to j}$ R-Matrix (IC) [71]	$A_{i \to j}$ RMPS (LS) [71]
3s $^2[1/2]_1^o \to 2p^6$ ($^1S_0$)	$6.11 \times 10^{+8}$	$6.51 \times 10^{+8}$	$7.29 \times 10^{+8}$	$6.95 \times 10^{+8}$
3s $^2[3/2]_1^o \to 2p^6$ ($^1S_0$)	$4.76 \times 10^{+7}$	$4.74 \times 10^{+7}$	$3.93 \times 10^{+7}$	$4.04 \times 10^{+7}$

Table 8.5: Dipole transitions to the ground and metastable for the lowest 12 levels of Ne.

As we see in table 8.5, all the dipole values seem to be close for the different sets of calculations. It also seems that the pseudo-states atomic structure calculated by Griffin and Ballance agrees closer to the other calculations than the one without them. Therefore we now can be more confident that the differences on the collision data are mainly caused by the employment of pseudo-states in the R-Matrix calculation, differences due to (IC) versus (LS) coupling, or differences in accuracy between the Plane Wave $Born$ method and the R-Matrix calculations.

8.2.2 Cross-Sections Comparison

After comparing the atomic structure for the different set of calculations, we focus on comparing some of the electron-impact excitation cross-sections. Unfortunately O'Mulane's [11] excitation cross-sections are not available, so we compare the (IC) and (LS) data of Griffin and Ballance [71], against the data of Zatsarinny and Bartschat [72]. Figures 8.1, 8.2, 8.3, and 8.1 show excitation cross-sections for the $2p^6$ ($^1S_0$) $\rightarrow$ 3s $^2[1/2]^o_1$ ($^1P_1$) and $2p^6$ ($^1S_0$) $\rightarrow$ 3p $^2[1/2]_1$ ($^3S_1$). As we can see, below the ionization potential, both R-Matrix (IC) and RMPS (LS) calculations (Griffin and Ballance [71]) are very close. The data of Zatsarinny and Bartschat [72] also shows a similar resonant structure, although with fewer resonances due to the smaller number of states included in their calculation. The differences between the Zatsarinny and Bartschat (IC) data with the (LS) of Griffin and Ballance at higher energies is due to the inclusion of continuum coupling effects [60] in the (LS) data. Notice that the (IC) calculation of Griffin and Ballance [71] does not extend above about 22 eV, and is then connected linearly to the limit point. The reason we have chosen the 3s $^2[1/2]^o_1$ ($^1P_1$) and 3p $^2[1/2]_1$ ($^3S_1$) levels to show these comparisons, is that each of these terms correspond to a single level in the (IC) coupling.
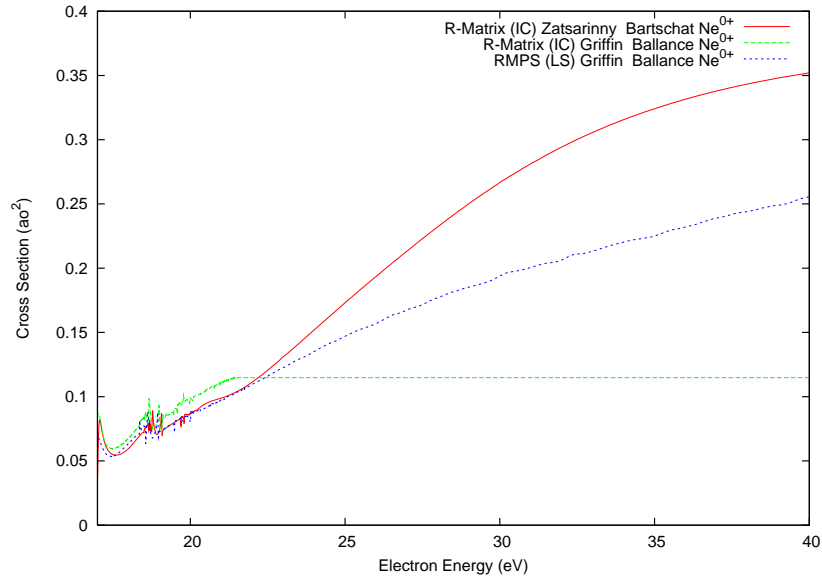
Figure 8.1: Excitation cross-section for the $2p^6$ ($^1S_0$) $\rightarrow$ 3s $^2[1/2]^o_1$ ($^1P_1$) transition.

Figure 8.2 shows the comparison between the two R-Matrix (IC) and RMPS (LS) data sets cal-culated by Griffin and Ballance [71], against the R-Matrix (IC) data set of Zatsarinny and Bartschat [72] below the ionization potential (21.565 eV). It is shown by Griffin and Ballance [60] that below the ionization potential the pseudo-state effects are small when comparing dipole transitions. We notice the high level of agreement between the calculations.
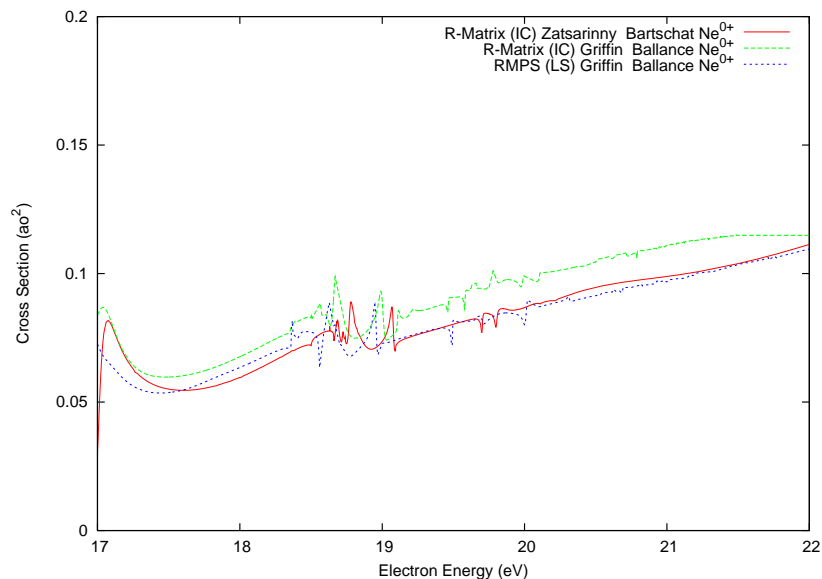
Figure 8.2: Excitation cross-section for the $2p^6$ ($^1S_0$) $\rightarrow$ 3s $^2[1/2]_1^o$ ($^1P_1$) transition.

Figure 8.3 shows the comparison for the $2p^6$ ($^1S_0$) $\rightarrow$ 3p $^2[1/2]_1$ ($^3S_1$) transition against Chilton's et al. [73] experimental values.
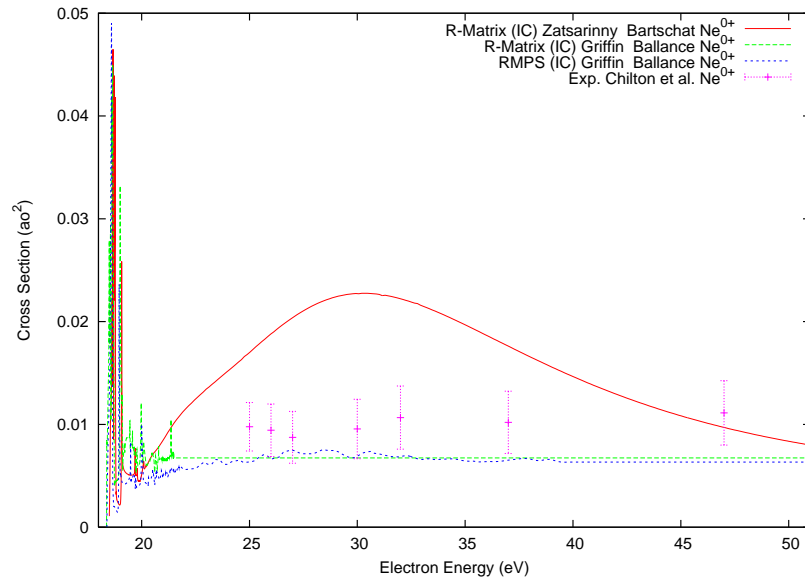
Figure 8.3: Excitation cross-section for the $2p^6$ ($^1S_0$) $\rightarrow$ 3p $^2[1/2]_1$ ($^3S_1$) transition.

We also notice that above the ionization potential the pseudo-state effects become significant as predicted by Ballance and Griffin [60], thus affecting the modeling above the ionization potential.

By taking a look below the ionization potential for the $2p^6$ ($^1S_0$) $\rightarrow$ 3p $^2[1/2]_1$ ($^3S_1$) transition (see figure 8.4), we notice that the level of agreement is very high between the three calculations. However, it is also clear that the omission of continuum coupling effects in the Zatsarinny and Bartschat data is extending below the ionization potential, even for this strong dipole excitation.
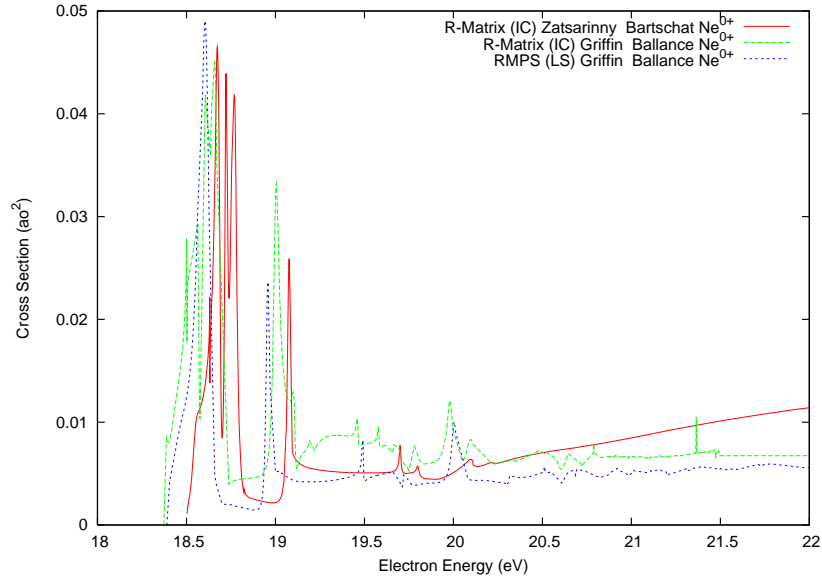
Figure 8.4: Excitation cross-section for the $2p^6$ ($^1S_0$) $\rightarrow$ 3p $^2[1/2]_1$ ($^3S_1$) transition.

We also notice from figure 8.4 that most of the resonances agree between the calculations, except the ones caused by the lack of the $1s^2 2s^2 2p^5 nl$ (nl = 4p, 4d, 4f, 5s, and 5p) in atomic structure calculation used by Zatsarinny and Bartschat.

In order to compare excitation cross-sections from the 3s $^2[3/2]^o_2$ ($^3P_2$) metastable level with Boffard et al. [74] experimental data, we compare only the data of Zatsarinny and Bartschat, and the (IC) calculation of Griffin and Ballance [71]. The $2p^5 3s$ (^3P) term has three levels of which, the $^3P_2$ and $^3P_0$ may be metastable, thus we cannot compare the metastable excitation measurements (from the $^3P_2$ level) with the RMPS (LS) coupling data. Figures 8.5, 8.6, 8.7, and 8.8 show the transitions from the 3s $^2[3/2]^o_2$ ($^3P_2$) metastable level to 3p $^2[5/2]_3$ ($^3D_3$), 3p $^2[5/2]_2$ ($^1D_2$), 3p $^2[3/2]_2$ ($^3P_2$), and 3p $^2[3/2]_2$ ($^3D_2$) excited levels.
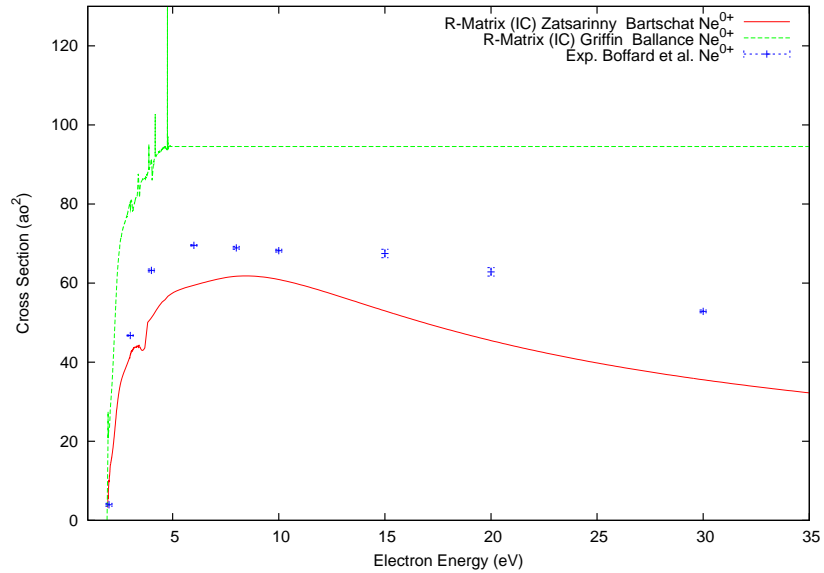
Figure 8.5: Excitation cross-section for the 3s $^2[3/2]^o_2$ ($^3P_2$) $\rightarrow$ 3p $^2[5/2]_3$ ($^3D_3$) transition.

These figures show that for some of the excitations the data of Zatsarinny and Bartschat is in better agreement with experiment (see figures 8.5, 8.6, and 8.8), while for other excitations, the data of Griffin and Ballance agrees better with experiment (see figure 8.7). Thus, for any excited populations that are sensitive to collisions from the metastable, one would expect to see differences between the emission results using the two different R-Matrix data sets.
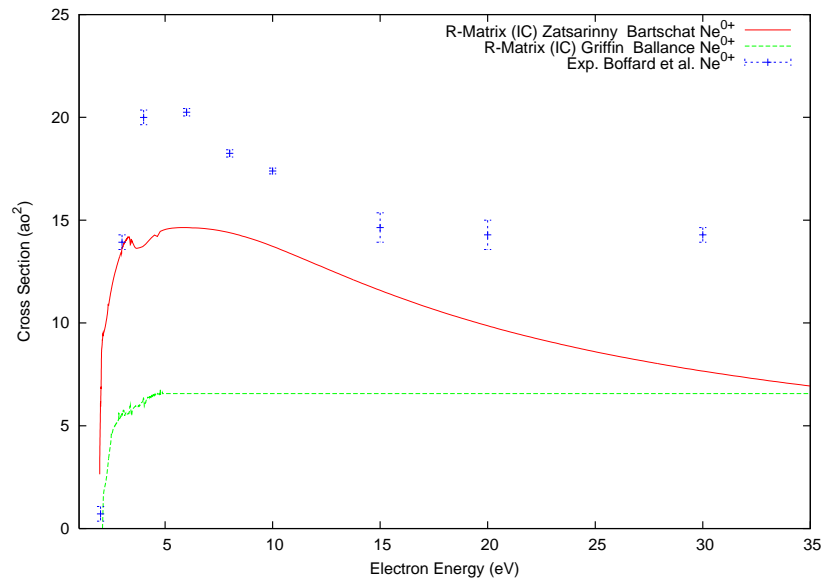
Figure 8.6: Excitation cross-section for the 3s $^2[3/2]^o_2$ ($^3P_2$) $\rightarrow$ 3p $^2[5/2]_2$ ($^1D_2$) transition.
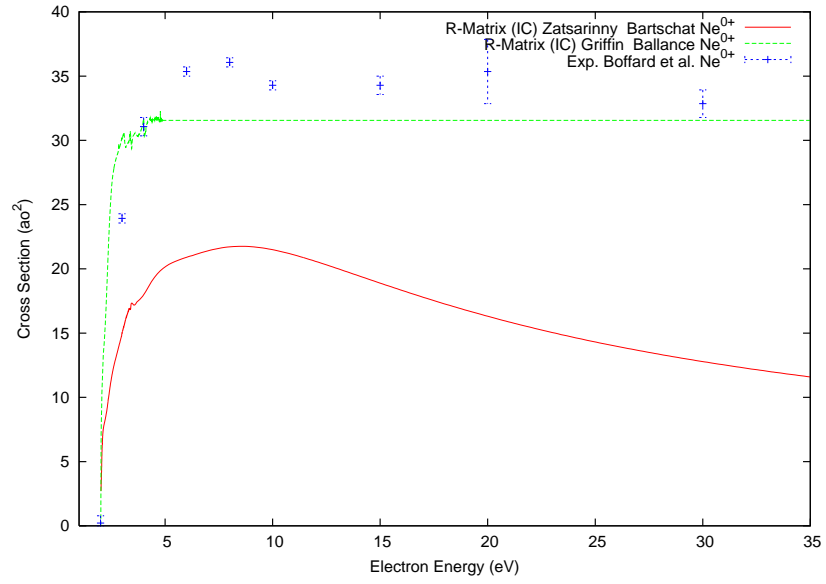
Figure 8.7: Excitation cross-section for the 3s $^2[3/2]^o_2$ ($^3P_2$) $\rightarrow$ 3p $^2[3/2]_2$ ($^3P_2$) transition.
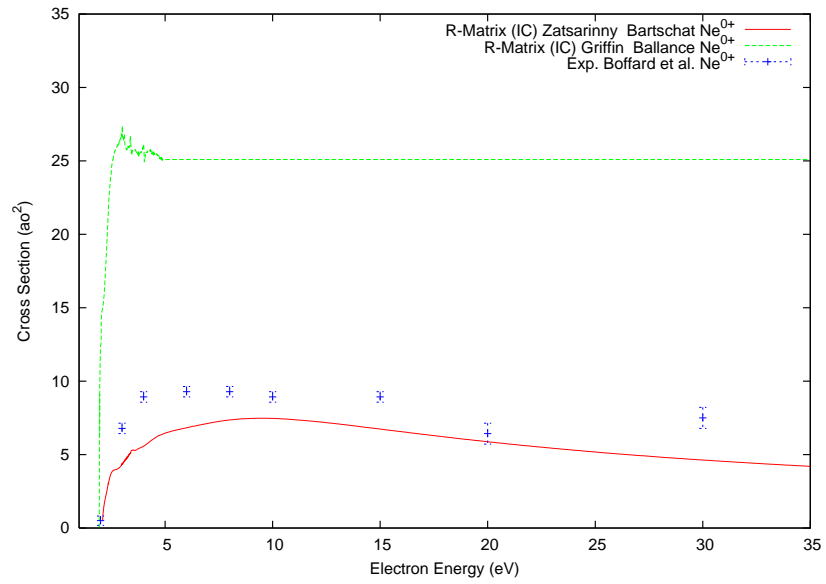
Figure 8.8: Excitation cross-section for the 3s $^2[3/2]^o_2$ ($^3P_2$) $\rightarrow$ 3p $^2[3/2]_2$ ($^3D_2$) transition.

8.3   Emission Modeling

In order to produce a modeled spectrum, we again apply our electron-impact excitation data into the collisional-radiative model (see chapter 2). We again employ the ADAS [11] suite of codes to the calculation of excited populations within a level. In order to calculate the fractional abundance within each of the ion stages, ADAS solve equation (2.20). Figure 8.9 show the results for the ionization balance calculation for neon.
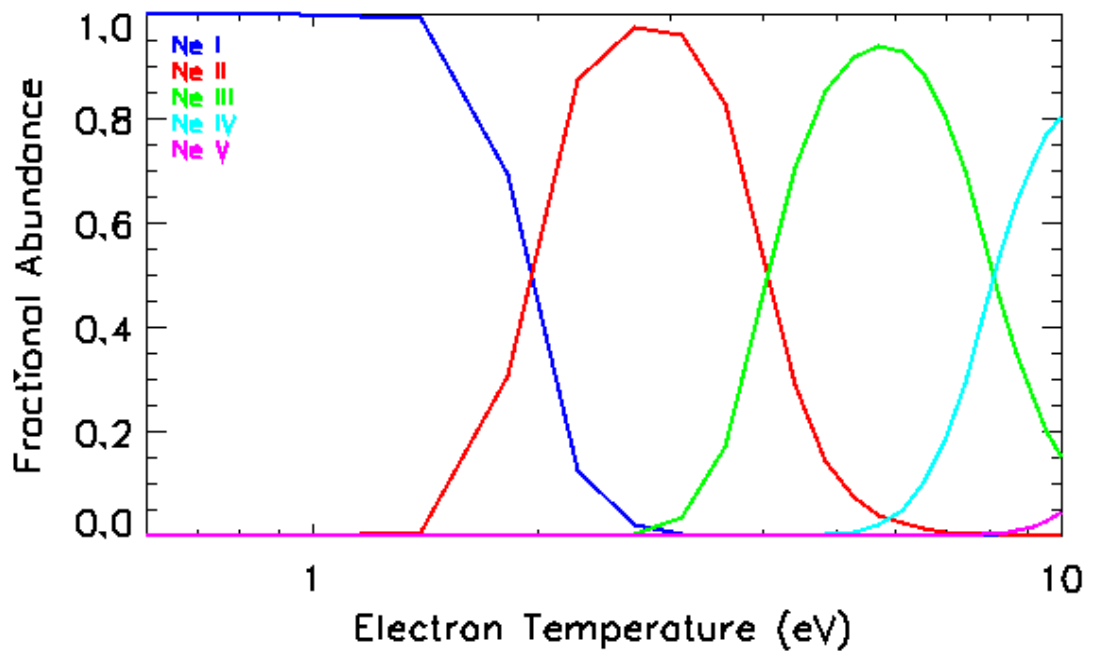
Figure 8.9: Ionization balance of Ne ($n_e = 10^{11}$ cm^{-3}).

Our ASTRAL Ne plasma temperature ranges mainly between 1 and 6 eV. We see mostly neutral Ne emission. By comparison with the energy levels shown in figure 8.10, we see that the free electrons in our plasma are well below the energy required for excitation from the ground. Thus, the excited populations may be populated from high energy electrons in the tail of the $Maxwellian$, but also likely to be populated from the metastable levels.
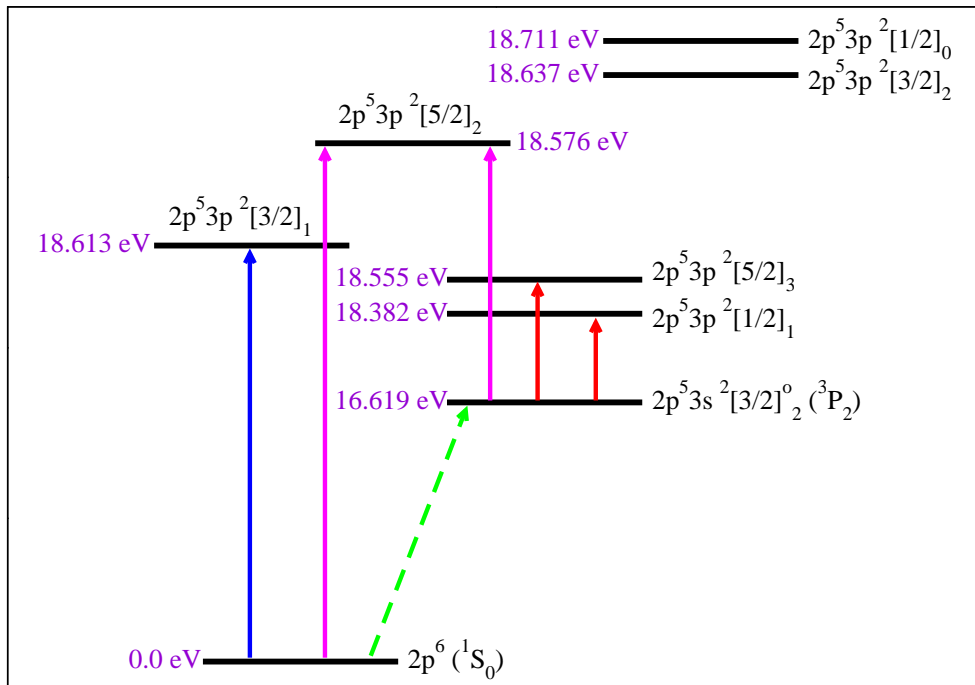
Figure 8.10: Excitation $Grotrian$ diagram of Ne.

As shown in chapter 6.4, in order to accurately model the line emission of Ne, we need to calculate the intensity of each spectral line which is given by equation (6.1). We have already shown (see chapter 6.4) the importance of the line of sight integration along the diameter of the vacuum chamber in order to include the temperature and density dependence. We therefore rely on experimental $Langmuir$ probe measurements (see chapter 5.3) to include in our emission modeling.

Figures 8.11 and 8.12 show the measured electron temperature and density distributions in the helicon plasma for conditions typical of our Ne experiments.
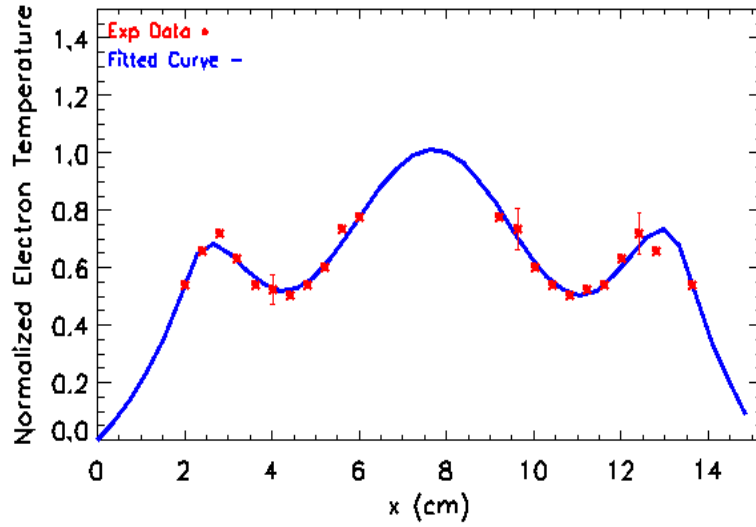
Figure 8.11: Normalized electron temperature distributions along the diameter of the vacuum chamber in ASTRAL.
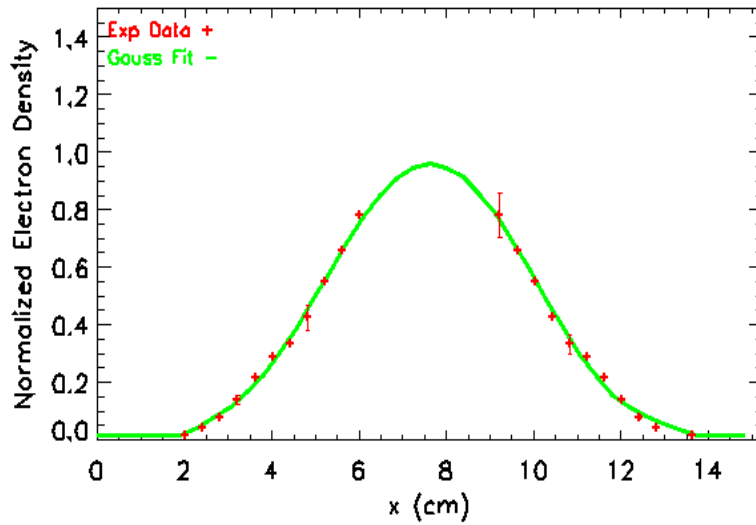
Figure 8.12: Normalized electron density distribution along the diameter of the vacuum chamber in ASTRAL .

The results have been normalized to allow a general distribution function to be fitted, which can be used for any T_e, N_e values. It was found that a polynomial distribution for the temperature, and a *Gaussian* distribution function for the density fitted well the experimental data, as shown in figures 8.11 and 8.12. The equations for the normalized fits are given by 8.1 and 8.2

$$T(x) = -1.117306 \times 10^{-4}x^6 + 5.172774 \times 10^{-3}x^5$$
$$- 9.340397 \times 10^{-2}x^4 + 0.830173x^3 - 3.775543x^2$$
$$+ 8.26994x - 6.20074 \tag{8.1}$$

$$\rho(x) = e^{-\frac{(x-L/2)^2}{2\sigma_\rho^2}} \tag{8.2}$$

Where L = 15.24 cm, σ_ρ = 2.0 cm, and x is the position along the diameter of the vacuum chamber. In our modeling we calculate along the line of sight the fractional abundances for each N_e/T_e grid point. The excited populations are also calculated for the same grid and the total intensity obtained using equation (6.1).

In order to compare only the atomic collision data, we rely on accurate *Einstein*'s A_{jk} coefficients calculated by Tachiev and Fischer [80]. We first consider spectral transitions that can be excited from the ground by a dipole collisional excitation. Since the R-Matrix (IC) of Zatsarinny and Bartschat [72] and the RMPS (LS) of Griffin and Ballance [71] data sets have similar cross-sections for excitation from the ground, one might expect these two data sets to produce similar results. Thus, differences in these predicted line intensity would strongly suggest that the excited levels are also populated from the metastables. This situation seems likely given the large energy required to excite from the ground. After looking at these spectral lines we will move on to the lines that are dipole connected to the metastable (see table 8.6 and figure 8.10). Since the intensity line emission is given in arbitrary units, the intensity plots are only helpful in comparing the relative intensity between different lines and the experiment.

To compare which set give us the best results, we rely on intensity line ratios. We are also making the assumption that the levels are being statistically populated when modeling intensity line emission by using the RMPS (LS) data set of Griffin and Ballance [71].

	Configuration	Term Mixing $^{2S+1}L_J$ (%)	Energy (eV)
Ground Level	$2p^6$	$^1S_0$ (1.00)	0.0 eV
Metastable Levels	$2p^5 3s\ ^2[3/2]^o_2$	$^3P_2$ (1.00)	16.619 eV
	$2p^5 3s\ ^2[1/2]^o_0$	$^3P_0$ (1.00)	16.715 eV

Population Likehood	Line (nm)	Upper Level Energy (eV)	Term Mixing of Upper Level $^{2S+1}L_J$ (%)
Ground	621.73 nm 626.65 nm 638.30 nm 653.29 nm 671.70 nm	$2p^5 3p\ ^2[3/2]_1$ 18.613 eV	$^1P_1$ (0.56) $^3P_1$ (0.28) $^3D_1$ (0.16)
Pure Metastable	640.22 nm	$2p^5 3p\ ^2[5/2]_3$ 18.555 eV	$^3D_3$ (1.00)
Metastable	602.99 nm 616.36 nm 659.89 nm 703.24 nm 724.52 nm 743.89 nm	$2p^5 3p\ ^2[1/2]_1$ 18.382 eV	$^3S_1$ (0.67) $^3P_1$ (0.22) $^1P_1$ (0.11)
Ground & Metastable	650.65 nm 717.39 nm	$2p^5 3p\ ^2[5/2]_2$ 18.576 eV	$^1D_2$ (0.60) $^3D_2$ (0.40)
Neither Ground nor Metastable	540.06 nm 585.25 nm 607.43 nm	$2p^5 3p\ ^2[1/2]_0$ 18.711 eV	$^1S_0$ (0.67) $^3P_0$ (0.33)
Neither Ground nor Metastable	594.48 nm 609.62 nm 614.31 nm 630.48 nm 667.83 nm 692.95 nm	$2p^5 3p\ ^2[3/2]_2$ 18.637 eV	$^3P_2$ (0.83) $^3D_2$ (0.10) $^1D_2$ (0.07)

Table 8.6: Ne spectral transitions measured in the ASTRAL experiment. Also shown are the square of the term mixing coefficients for the upper levels, to allow us to see what levels are likely to be excited from the ground.

8.4 Experimental Results

We present our modeling results and compare them to the experimental data from ASTRAL (see chapter 5). We first look at spectral lines that can be dipole excited from the ground (see table 8.6), showing this way the emission line intensity results first, and the intensity line ratios second for each section.

8.4.1 Spectral Dipole Lines Connected to the Ground

Figure 8.13: Line intensity for the $2p^5 3p\ ^2[3/2]_1$ upper level. The solid line shows the RMPS data set of Griffin and Ballance [71], the dashed line shows the R-Matrix data set of Zatsarinny and Bartschat [72], and the dotted line shows O'Mullane's [11] Plane Wave $Born$ (see chapter 4.2) data.
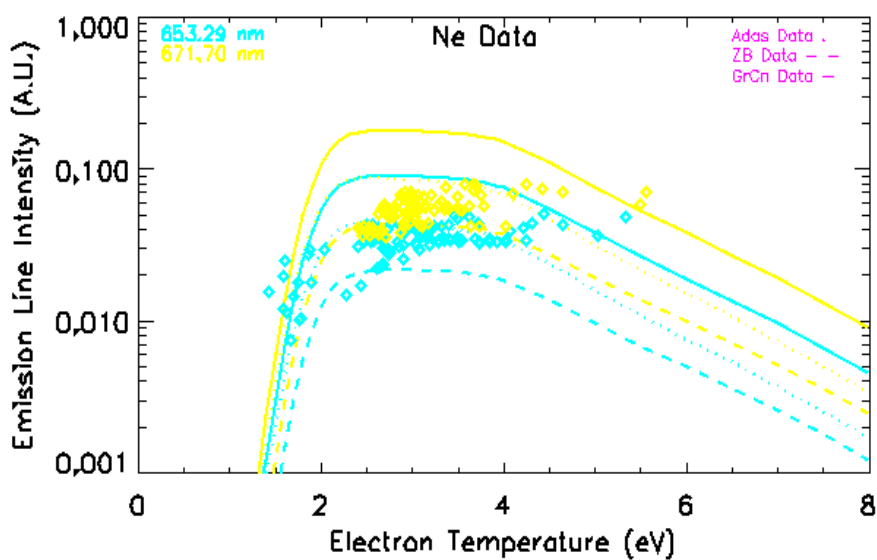
Figure 8.14: Line intensity for the $2p^5 3p$ $^2[3/2]_1$ upper level.

Figure 8.15: Intensity line ratio of I(638.30)/I(626.65). The solid line shows the RMPS data set of Griffin and Ballance [71], the dashed line shows the R-Matrix data set of Zatsarinny and Bartschat [72], and the dotted line shows O'Mullane's [11] Plane Wave $Born$ (see chapter 4.2) data.
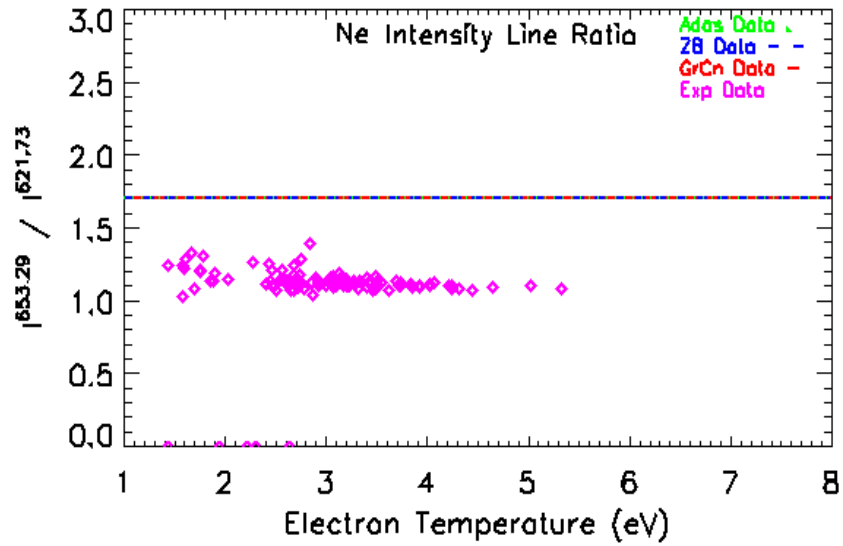
Figure 8.16: Intensity line ratio of I(653.29)/I(621.73). The solid line shows the RMPS data set of Griffin and Ballance [71], the dashed line shows the R-Matrix data set of Zatsarinny and Bartschat [72], and the dotted line shows O'Mullane's [11] Plane Wave $Born$ (see chapter 4.2) data.

In this case, the three sets of calculations agree on the line ratio. The fact that the R-Matrix and the RMPS data sets produce different intensities strongly suggests that the excited levels have a strong population contribution coming from the metastable. This would also explain why none of the data sets are able to explain all of the measurements.

8.4.2   Spectral Dipole Lines Connected to the Metastable
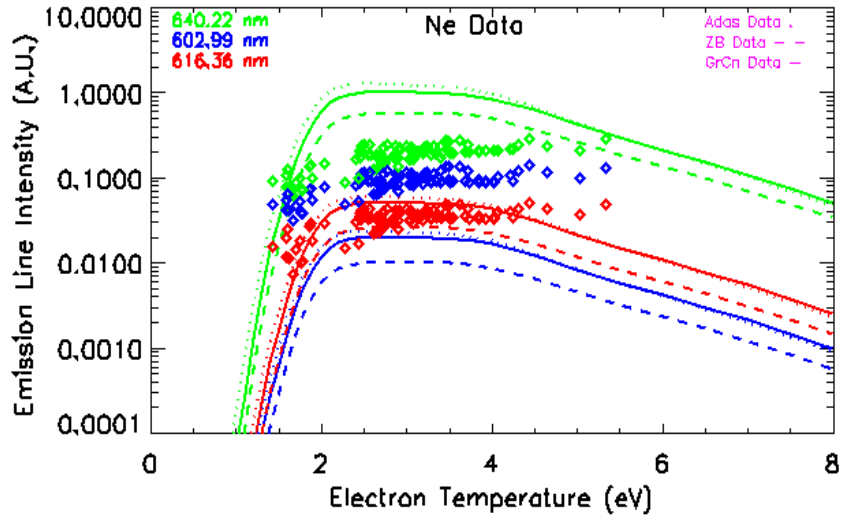
Figure 8.17: Line intensity for the $2p^5 3p\ ^2[5/2]_3$ and $2p^5 3p\ ^2[1/2]_1$ upper levels.
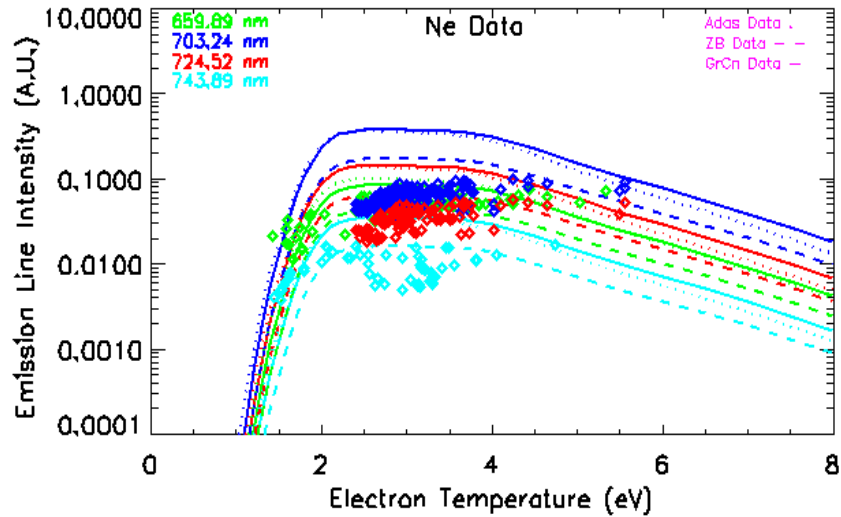
Figure 8.18: Line intensity for the $2p^5 3p\ ^2[1/2]_1$ upper level. The solid line shows the RMPS data set of Griffin and Ballance [71], the dashed line shows the R-Matrix data set of Zatsarinny and Bartschat [72], and the dotted line shows O'Mullane's [11] Plane Wave $\boldsymbol{Born}$ (see chapter 4.2) data.

155
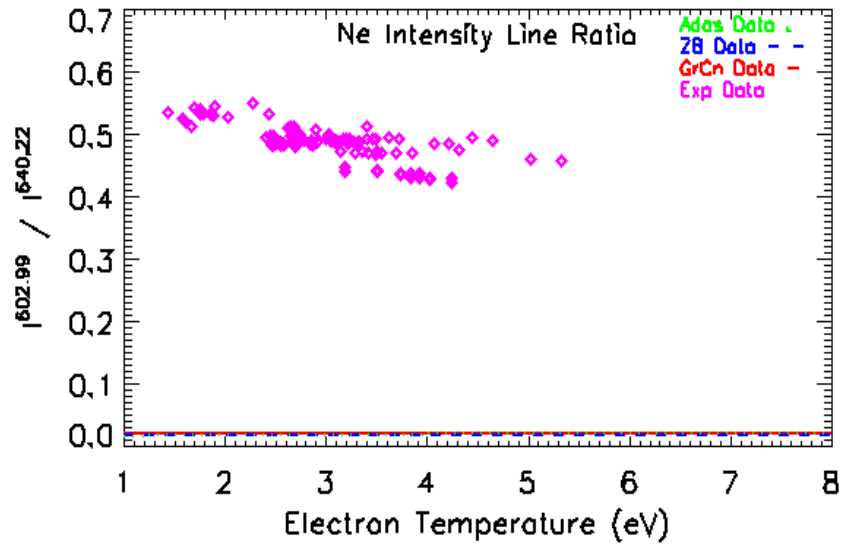
Figure 8.19: Intensity line ratio of I(602.99)/I(640.22).
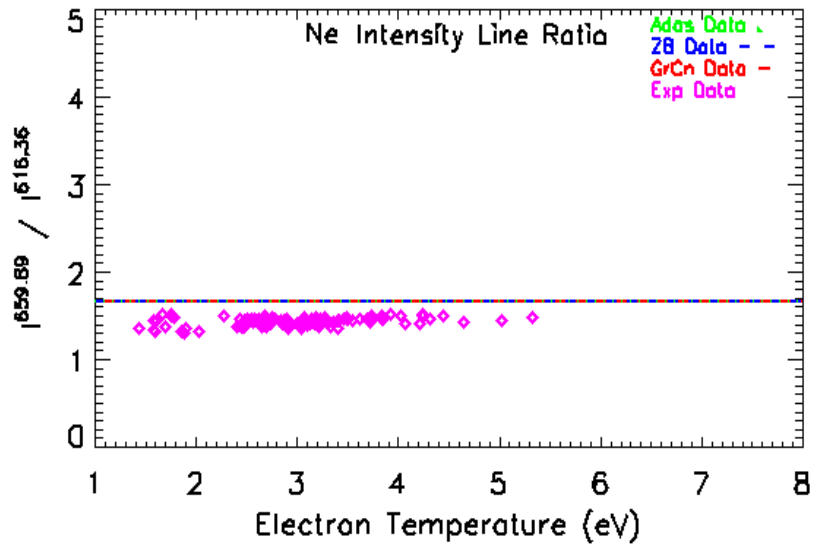
Figure 8.20: Intensity line ratio of I(659.89)/I(616.36). The solid line shows the RMPS data set of Griffin and Ballance [71], the dashed line shows the R-Matrix data set of Zatsarinny and Bartschat [72], and the dotted line shows O'Mullane's [11] Plane Wave $Born$ (see chapter 4.2) data.

The fact that the experimental ratio is also flat, means that our assumption of statistically splitting the level populations within a term for the (LS) resolved RMPS [71] data set is appropriate for our plasma conditions.
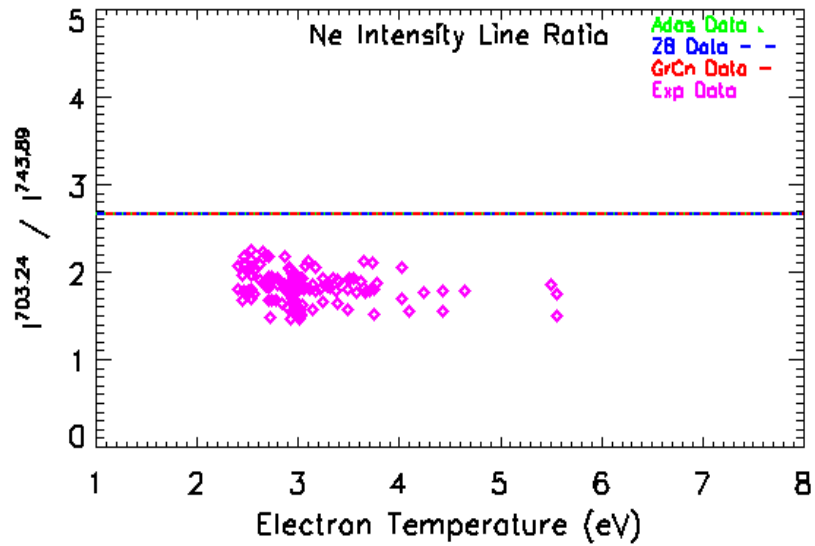
Figure 8.21: Intensity line ratio of I(703.24)/I(743.89). The solid line shows the RMPS data set of Griffin and Ballance [71], the dashed line shows the R-Matrix data set of Zatsarinny and Bartschat [72], and the dotted line shows O'Mullane's [11] Plane Wave $Born$ (see chapter 4.2) data.

The fact that some lines agree with the theory and others do not may again be due to differences in the excitation cross-sections from the metastable.

8.4.3   Spectral Dipole Lines Connected to the Ground and Metastable
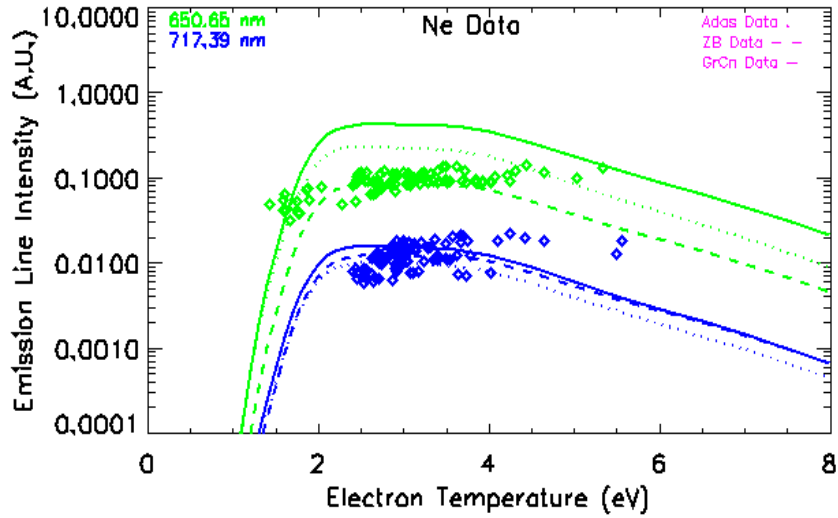
Figure 8.22: Line intensity for the $2p^5 3p\ ^2[5/2]_2$ upper level.
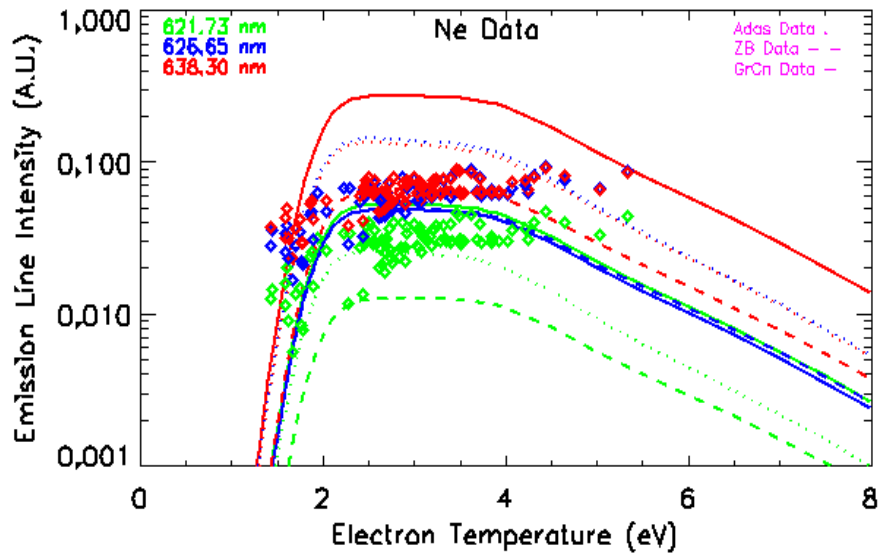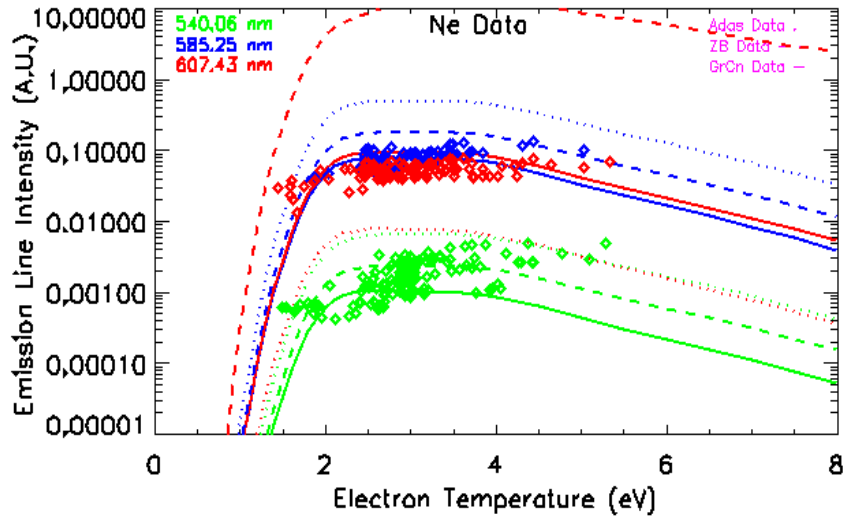

Figure 8.23: Line intensity for the $2p^5 3p\ ^2[1/2]_0$ upper level. The solid line shows the RMPS data set of Griffin and Ballance [71], the dashed line shows the R-Matrix data set of Zatsarinny and Bartschat [72], and the dotted line shows O'Mullane's [11] Plane Wave $\boldsymbol{Born}$ (see chapter 4.2) data.
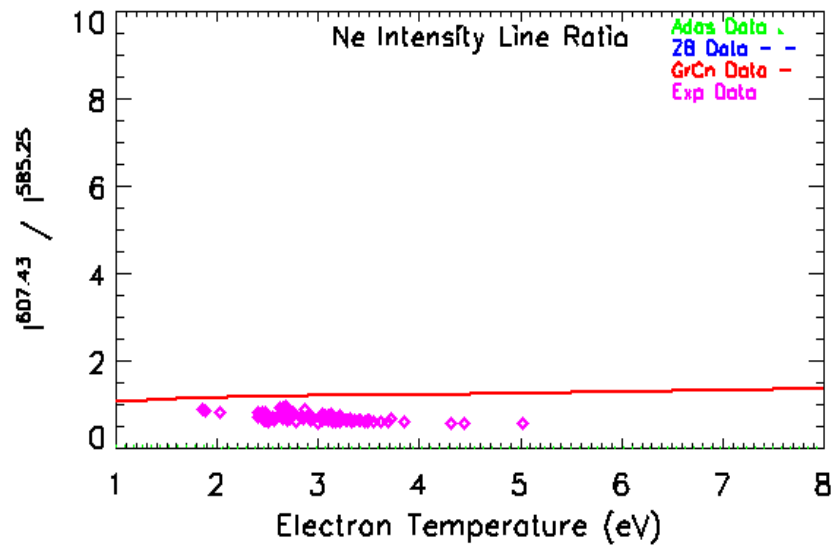
Figure 8.24: Intensity line ratio of I(607.43)/I(585.25). The solid line shows the RMPS data set of Griffin and Ballance [71], the dashed line shows the R-Matrix data set of Zatsarinny and Bartschat [72], and the dotted line shows O'Mullane's [11] Plane Wave $Born$ (see chapter 4.2) data.

8.4.4 Spectral Dipole Lines Not Connected to the Ground Nor the Metastable
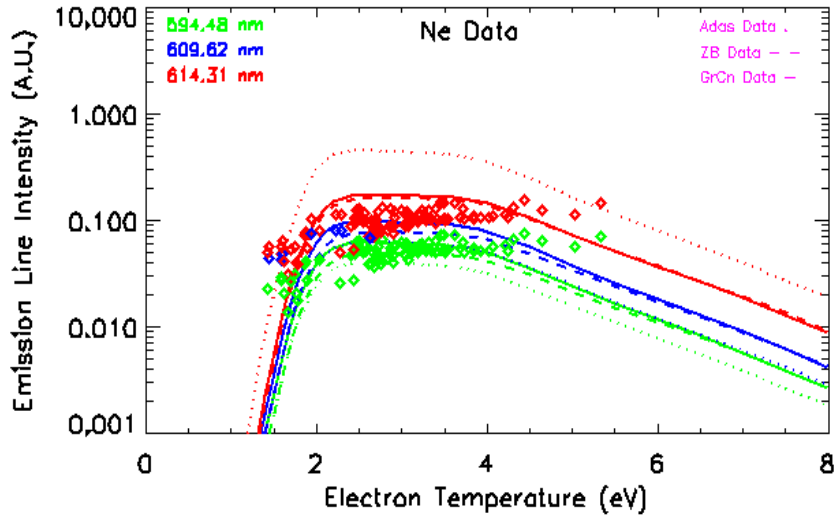
Figure 8.25: Line intensity for the $2p^5 3p \, {}^2[1/2]_0$ upper level.
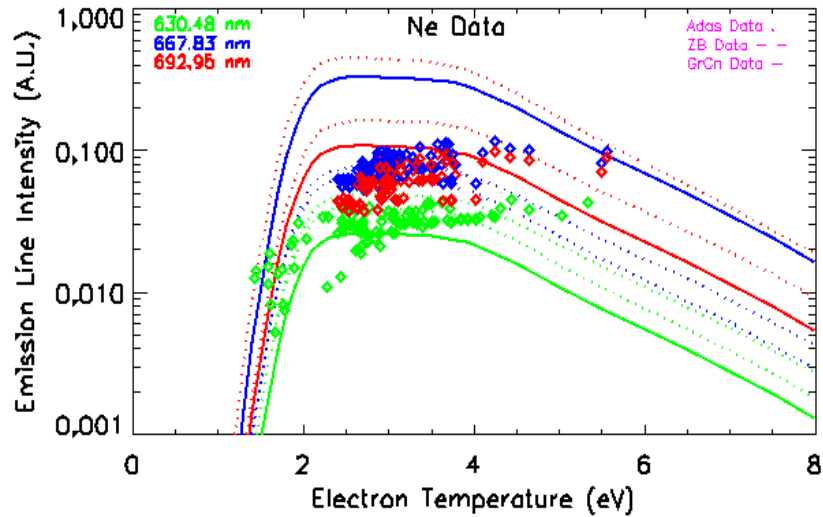
Figure 8.26: Line intensity for the $2p^5 3p \, {}^2[1/2]_0$ upper level. The solid line shows the RMPS data set of Griffin and Ballance [71], the dashed line shows the R-Matrix data set of Zatsarinny and Bartschat [72], and the dotted line shows O'Mullane's [11] Plane Wave $\boldsymbol{Born}$ (see chapter 4.2) data.
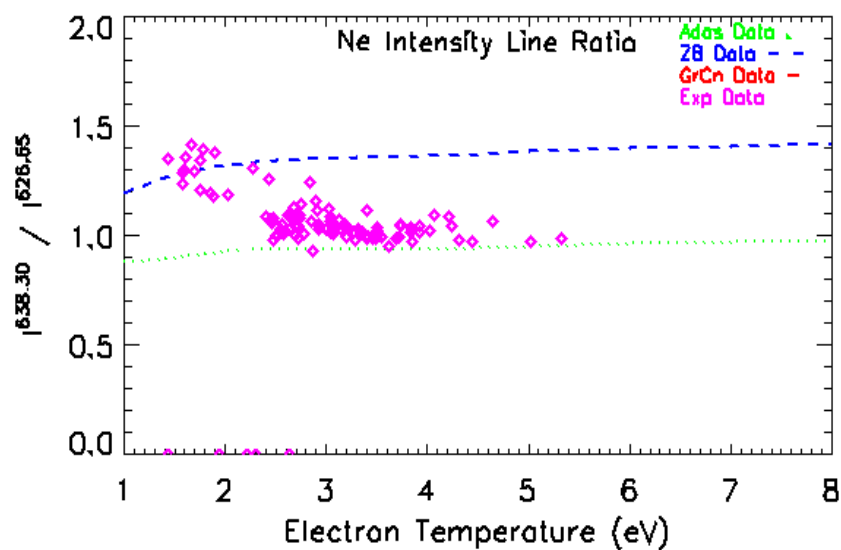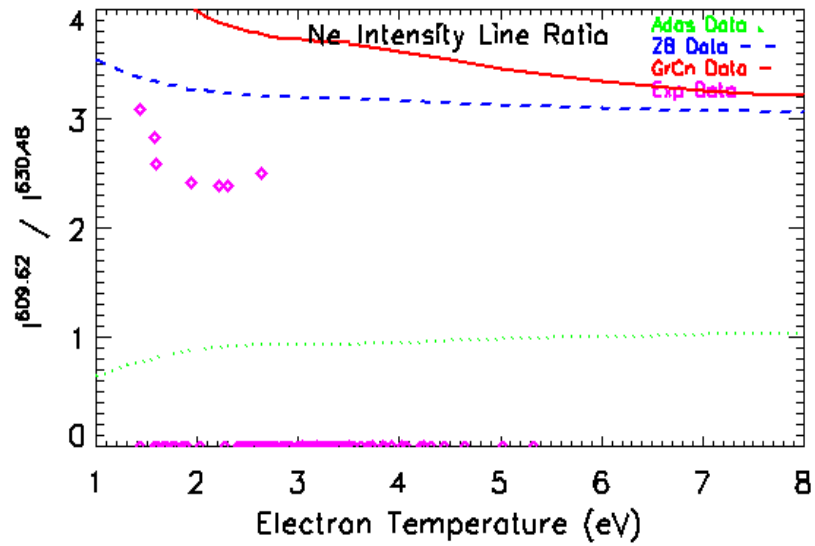
Figure 8.27: Intensity line ratio of I(609.62)/I(630.48).
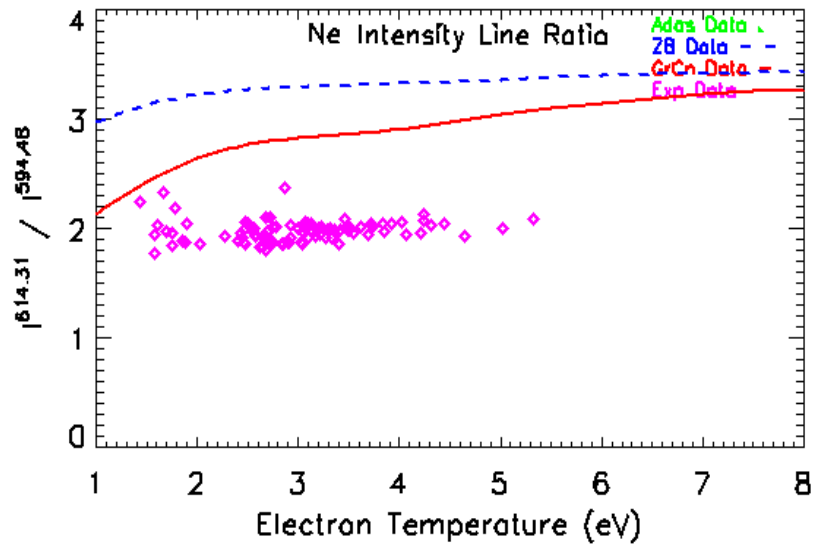
Figure 8.28: Intensity line ratio of I(614.31)/I(594.48). The solid line shows the RMPS data set of Griffin and Ballance [71], the dashed line shows the R-Matrix data set of Zatsarinny and Bartschat [72], and the dotted line shows O'Mullane's [11] Plane Wave $Born$ (see chapter 4.2) data.

161
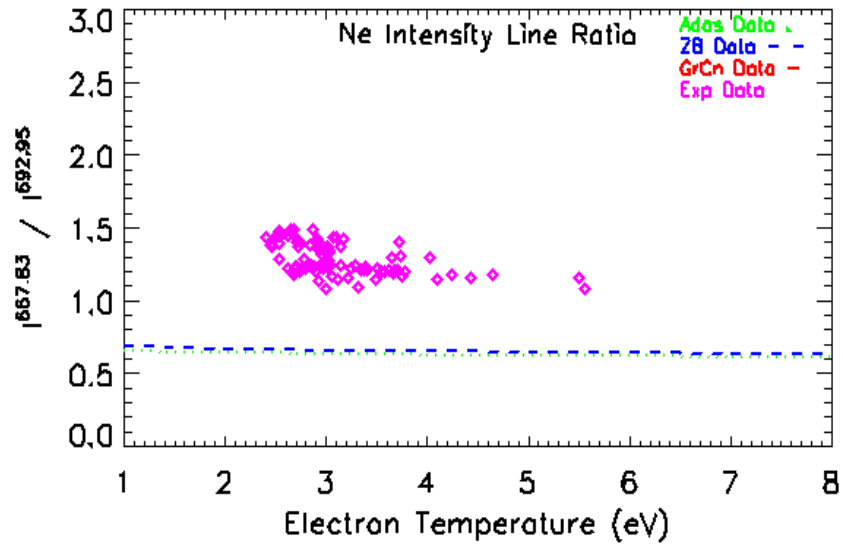
Figure 8.29: Intensity line ratio of I(667.83)/I(692.95). The solid line shows the RMPS data set of Griffin and Ballance [71], the dashed line shows the R-Matrix data set of Zatsarinny and Bartschat [72], and the dotted line shows O'Mullane's [11] Plane Wave $Born$ (see chapter 4.2) data.

Again, the sporadic agreemen of each of the data sets with the experiment suggests that each of them still have innacurate data, or that there are more complex mechanisms occuring in the plasma that have not taken in to account in our emission modeling (like interactions with the wall, opacity, metastable resolved ionization balance calculation, etc).

8.4.5   Other Dipole Line Ratios

We lastly take a look at a line ratio where the two lines originate from two different terms.
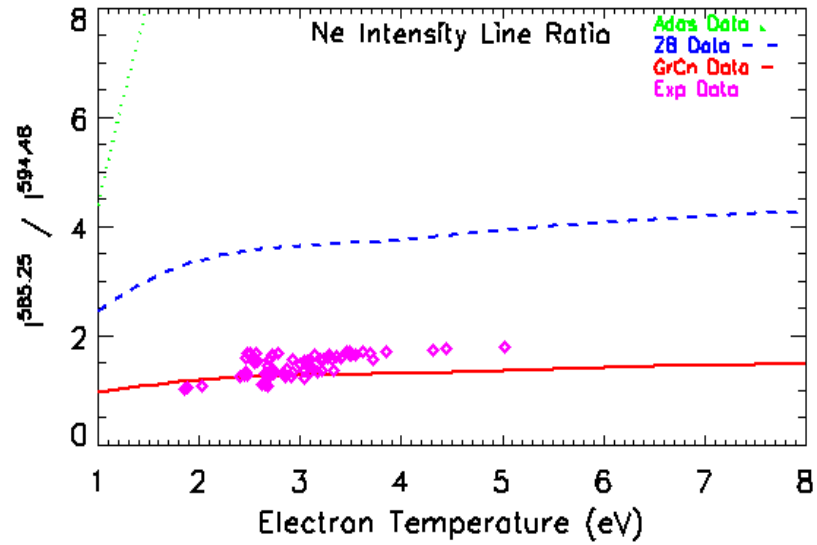
Figure 8.30: Intensity line ratio of I(585.25)/I(594.48). The solid line shows the RMPS data set of Griffin and Ballance [71], the dashed line shows the R-Matrix data set of Zatsarinny and Bartschat [72], and the dotted line shows O'Mullane's [11] Plane Wave $Born$ (see chapter 4.2) data.

CHAPTER 9

CONCLUSIONS

This dissertation has focused on modeling Ar II, Ar III, and Ne I emission, and on analyzing spectral emission from the Auburn ASTRAL helicon plasma. There are two main aims to this work. Firstly we investigated whether spectral measurements from ASTRAL could be used to benchmark the fundamental atomic data. Secondly we investigated intensity line ratios from Ar II, Ar III, and Ne I that could be used as temperature and density diagnostics. As part of these aims we generated, when needed, new atomic data that was used in the modeling. The work presented here is of general use for laboratory and astrophysical spectral diagnostics.

Some basic atomic structure theory has been described. The use of λ scale factors in optimizing atomic structure calculations was shown. The LAMDA code was developed to automatically adjust the λ scale factors and to optimize atomic structure based on NIST energies and line strengths. This LAMDA code has been used to optimize the atomic structure that was used for collisional data calculations.

We have also described various theoretical methods, such as the Plane Wave $Born$, Distorted-Wave, and R-Matrix approaches, that are used to calculate the atomic data in our modeling. We used collisional-radiative theory to predict spectral intensities, allowing for temperature and density variation along the line of sight of ASTRAL.

We successfully completed experimental measurements of Ar and Ne ions in the **A**uburn **S**teady s**T**ate **R**esearch f**A**ci**L**ity ASTRAL. As we have shown in chapters 6.1 and 8, $Langmuir$ probe measurements of the density and temperature distributions have been key for our emission modeling purposes. We have also shown the importance of wavelength calibration on the experimental spectroscopy data in order to reproduce accurate line intensity ratios.

We have assembled a new atomic data set for Ar^+. It includes RMPS, level-resolved Distorted Wave, and CADW rate coefficients. When we calculated ionization balance using the new data we see a shift in the temperature at which Ar II emits, in a good agreement with our ASTRAL measurements. The differences are mostly due to the new CADW dielectronic recombination data, with the new RMPS Ar^+ ionization also making a difference. This proved to be a useful experimental verification of the new atomic data. We have identified several line ratios in Ar^+ to test the RMPS excitation data, and to identify potentially useful line ratios for N_e and T_e diagnostics. In our comparison with ASTRAL line intensities as a function of T_e, we obtained good agreement with our theoretical predictions using the RMPS data, when the variation of T_e and N_e along the line of sight was accounted for.

The results from an ICFT calculation for Ar^{2+} are shown to be close to those from a Breit-Pauli calculation. Our final R-Matrix calculation consists of a Breit-Pauli calculation with the first 9 levels shifted to NIST energies. While this data for Ar^{2+} was generated to model ASTRAL emission, it was also found to have applications for planetary nebulae diagnostics. We compared the results of this calculation with literature values for transitions within the $3p^4$ configuration, finding differences at low temperatures due to low energy resonance contributions. Forbidden lines within the $3p^4$ configuration are commonly used as T_e and N_e diagnostics of low density planetary nebulae.

We calculated one temperature sensitive and one density sensitive line ratio, finding that our new data does not make a significant differences to the temperature diagnostic, but does have a sizeable affect on the density diagnostic compared to values calculated using previous R-Matrix data. Our final effective collision strengths are now available on the Oak Ridge National Laboratory Atomic Data Web [62], and in the ADAS [11] database.

We have presented mixed results for the modeling for neutral neon for different electron-impact excitation data sets. Some of the lines have been modeled successfully while some others have not. We used electron-impact excitation Plane Wave $Born$ (IC) data calculated by O'Mullane [11], R-Matrix (IC) data calculated by Zatsarinny and Bartschat [72], and newly calculated R-Matrix (IC) and RMPS (LS) data sets by Griffin and Ballance [71]. We have also assumed statistical populations on the atomic levels in order to use the RMPS (LS) excitation data of Griffin and Ballance in our emission modeling. The R-Matrix data sets show good agreement with experimental measurements of excitation cross-sections from the ground level, but varying levels of disagreement for excitation from the metastable level. Comparison with ASTRAL spectral measurements suggest that the metastable plays a significant role in populating the excited states. We concluded that in order to successfully model emission from neutral neon, we need to perform a new large RMPS (IC) resolved calculation in the future.

APPENDICES

Green's Function Solution for the Non-Homogeneous *Helmholtz* Equation

A.1   The *Helmholtz* Equation

The non-homogeneous *Helmholtz* equation is given by

$$(\vec{\nabla}^2 + k^2)\psi = Q \tag{A.1}$$

Where Q is an arbitrary "driven" function, therefore we seek a solution by using *Green*'s functions to find a solution in the integral form

$$\psi(\vec{r}) = \int G(\vec{r} - \vec{r}_o)Q(\vec{r}_o)d^3\vec{r}_o \tag{A.2}$$

By the definition, the *Green*'s function $G(\vec{r})$ for a linear differential equation represents the "response" of the system to a delta-function source. Therefore we write the *Green*'s function equation as

$$(\vec{\nabla}^2 + k^2)G(\vec{r}) = \delta^3(\vec{r}) \tag{A.3}$$

A.2 *Green*'s Function Solution

By applying the operator $(\vec{\nabla}^2 + k^2)$ into equation (A.2), and by the definition given by equation (A.3) we get

$$(\vec{\nabla}^2 + k^2)\psi(\vec{r}) = \int \left[(\vec{\nabla}^2 + k^2)G(\vec{r} - \vec{r}_o)\right]Q(\vec{r}_o)d^3\vec{r}_o$$

$$= \int \delta^3(\vec{r} - \vec{r}_o)Q(r_o)d^3\vec{r}_o = Q(\vec{r}) \tag{A.4}$$

The *Fourier* transform for $G(\vec{r})$ is given by

$$G(\vec{r}) = \frac{1}{(2\pi)^{3/2}} \int e^{i\vec{s}\cdot\vec{r}}g(\vec{s})d^3\vec{s} \tag{A.5}$$

applying the operator $(\vec{\nabla}^2 + k^2)$ into equation (A.5) we get

$$(\vec{\nabla}^2 + k^2)G(\vec{r}) = \frac{1}{(2\pi)^{3/2}} \int \left[(\vec{\nabla}^2 + k^2)e^{i\vec{s}\cdot\vec{r}}\right]g(\vec{s})d^3\vec{s} \tag{A.6}$$

with

$$\vec{\nabla}^2 e^{i\vec{s}\cdot\vec{r}} = -s^2 e^{i\vec{s}\cdot\vec{r}} \tag{A.7}$$

For one dimensional delta function $\delta(x)$ is given in its *Fourier* form as

$$\delta(x) = \frac{1}{2\pi} \int_{-\infty}^{+\infty} e^{ikx}dk \tag{A.8}$$

and for the threedimensional delta function $\delta^3(\vec{r})$

$$\delta^3(\vec{r}) = \frac{1}{(2\pi)^3} \int e^{i\vec{s}\cdot\vec{r}}d^3\vec{s} \tag{A.9}$$

therefore we rewrite equation (A.6) in the form

$$\frac{1}{(2\pi)^{3/2}} \int (-s^2 + k^2)e^{i\vec{s}\cdot\vec{r}}g(\vec{s})d^3\vec{s} = \frac{1}{(2\pi)^3} \int e^{i\vec{s}\cdot\vec{r}}d^3\vec{s} \tag{A.10}$$

169

it follows that the solution for $g(\vec{s})$ is given by

$$g(\vec{s}) = \frac{1}{(2\pi)^{3/2}(k^2 - s^2)} \tag{A.11}$$

by plugging this solution into equation (A.5) we get

$$G(\vec{r}) = \frac{1}{(2\pi)^3} \int e^{i\vec{s}\cdot\vec{r}} \frac{1}{(k^2 - s^2)} d^3\vec{s} \tag{A.12}$$

In order to simplify the problem let us use spherical coordinates (s, θ, ϕ), and fixing $\vec{r}$ into the $\hat{z}$ axis direction as shown by figure A.1.
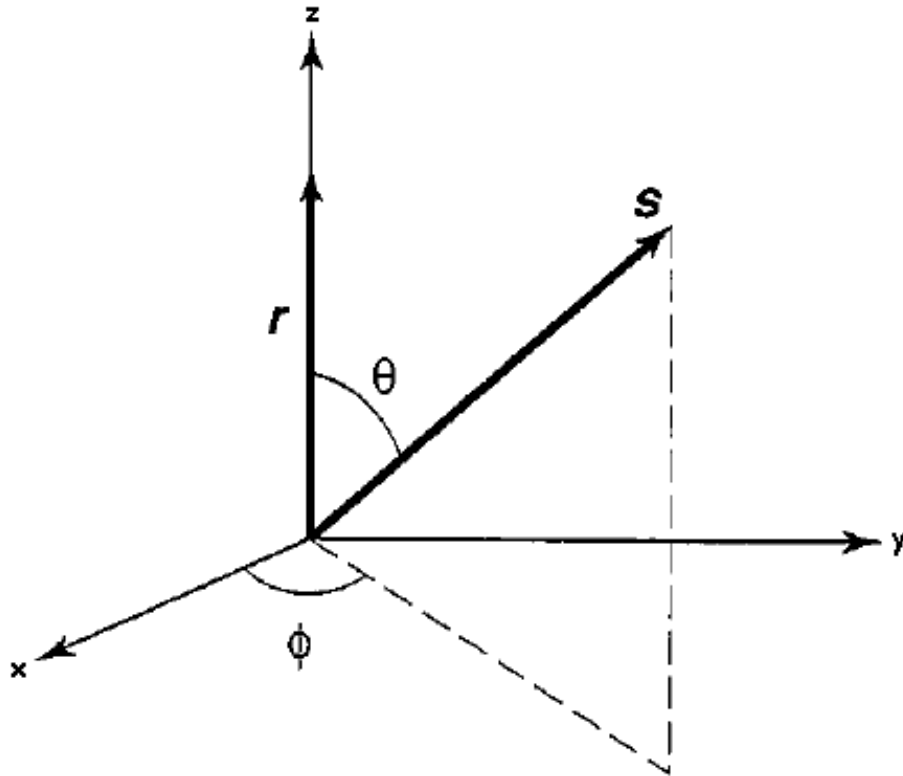
Figure A.1: Spherical coordinates representation.

170

Therefore $d^3\vec{s} = s^2 sin(\theta)dsd\theta d\phi$, and $\vec{s} \cdot \vec{r} = srcos(\theta)$. By integrating with respect to the angular dependence (θ, ϕ) we get

$$\int_0^{2\pi} \int_0^{\pi} e^{isrcos(\theta)} sin(\theta)d\theta d\phi = -\frac{2\pi e^{isrcos(\theta)}}{isr}\bigg|_0^{\pi} = \frac{4\pi sin(sr)}{sr} \tag{A.13}$$

thus we rewrite equation (A.12) in the form

$$G(\vec{r}) = \frac{1}{(2\pi)^2}\frac{2}{r}\int_0^{+\infty}\frac{s\, sin(sr)}{k^2 - s^2}ds = \frac{1}{4\pi^2 r}\int_{-\infty}^{+\infty}\frac{s\, sin(sr)}{k^2 - s^2}ds \tag{A.14}$$

Which is not a simple form to solve. Using $sin(sr) = \frac{1}{2i}(e^{isr} - e^{-isr})$ we rewrite the integral in the complex form

$$\begin{aligned} G(\vec{r}) &= \frac{i}{8\pi^2 r}\left\{ \int_{-\infty}^{+\infty}\frac{se^{isr}}{(s-k)(s+k)}ds - \int_{-\infty}^{+\infty}\frac{se^{-isr}}{(s-k)(s+k)}ds\right\} \\ &= \frac{i}{8\pi^2 r}(I_1 - I_2) \end{aligned} \tag{A.15}$$

where both integrals can be evaluated by using the $Cauchy$'s integral formula

$$\oint \frac{f(z)}{(z - z_o)}dz = 2\pi i f(z_o) \tag{A.16}$$

if z_o lies within the contour of integration, otherwise the integral is zero.
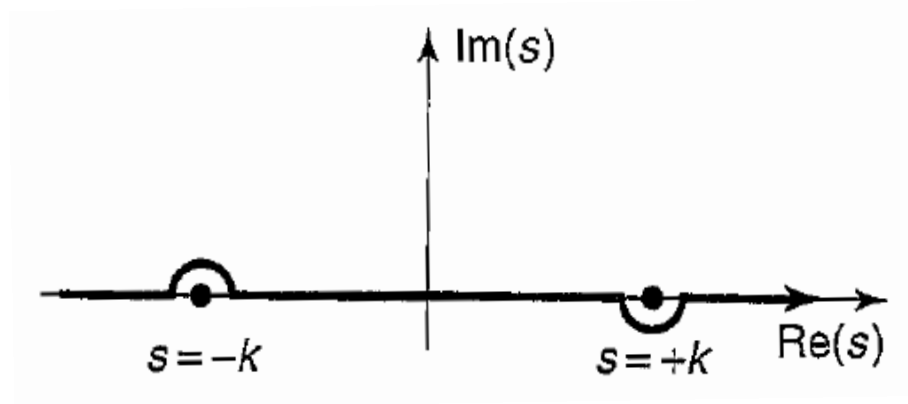
Figure A.2: Complex contour integration.

Figure A.2 describes how for each integral in equation (A.15), we chose to close the contour in such a way that the semicircle at infinity has a zero contribution. In case of the integral I_1, e^{isr} goes to zero when s has a large positive imaginary part. By defining the real axis as the "x" axis, and the imaginary axis "y", we then close the contour above (on the positive side of the imaginary axis). The contour encloses only the singularity at $s = +k$, therefore we get

$$I_1 = \oint \left[\frac{se^{isr}}{s+k} \right] \frac{1}{s-k} ds = 2\pi i \left[\frac{se^{isr}}{s+k} \right] \Bigg|_{s=k} = i\pi e^{ikr} \qquad (A.17)$$

For the case of the integral I_2, e^{-isr} goes to zero when s has a large negative imaginary part, therefore we close the contour below (on the negative side of the imaginary axis). The contour now encloses only the singularity at $s = -k$ and it goes around the clockwise direction so we pick up a minus sign, therefore we get

$$I_2 = -\oint \left[\frac{se^{-isr}}{s-k} \right] \frac{1}{s+k} ds = -2\pi i \left[\frac{se^{-isr}}{s-k} \right] \Bigg|_{s=-k} = -i\pi e^{ikr} \qquad (A.18)$$

therefore the final solution of the **Green**'s function is given by

$$G(\vec{r}) = -\frac{e^{ikr}}{4\pi r} \qquad (A.19)$$

172

SYSTEM RESPONSE FUNCTION FOR THE ASTRAL SPECTROMETER

B.1 Introduction

The response of the ASTRAL spectrometer [33] is measured as a function of wavelength. An absolutely calibrated Oriel Halogen lamp is used to measure the response of the spectrometer as a function of wavelength.

B.2 Calibration Procedures

B.2.1 Mounting the lamp

The lamp is held in an Oriel Model 63365 Lamp Mount, which allows for a vertical orientation in open air. Calibration data and lamp life standards can be found within the lamp's instruction manual [82]. The calibration area is surrounded by 5 non-reflective black surfaces. On top, no immediate surface is located close to the lamp.

The ceiling located about 3 meters above acts as the ultimate light collecting surface. Reflection from the ceiling is not a significant source of radiation for the collection optics. The open top surface keeps the temperature around the lamp constant, thus yielding a more stable operating environment. Laboratory lights are turned off during the entire calibration procedure.

B.2.2 Power Source

The lamp requires a well-regulated constant current that needs to be accurately calibrated to reproduce the same current value used in factory lamp calibration [82]. A Kepco ATE-75-15 regulated power supply is used to produce steady current for the lamp.

B.2.3 Measurement of Lamp Current

In order to reproduce the calibration current used in Oriel's Calibration Facility, a precision Fluke ammeter with accuracy of 0.5% is used. A gradual increase to reach the operating current was employed to improve the lamp's life and minimize drift [33]. A final lamp operation current of 6.50 Amperes was maintained during calibration. Ambient temperature was 21.1 ^{o}C.

B.2.4 CCD Camera Conditions

The acquisition time of the camera was 4 seconds to avoid photon detection saturation on the CCD, auto-background subtraction was used. Photons counts are comparable to those obtained during experiments. The camera temperature is maintained at -30 ^{o}C by a thermoelectric cooler. The entrance slit is 50 microns.

B.2.5 Oriel Model QTH 200W Calibration Curve

The calibration curve of the Oriel Quartz Tungsten Halogen lamp model QTH 200W is given by figure B.1. The irradiance data comes from Oriels Calibration Datasheets.
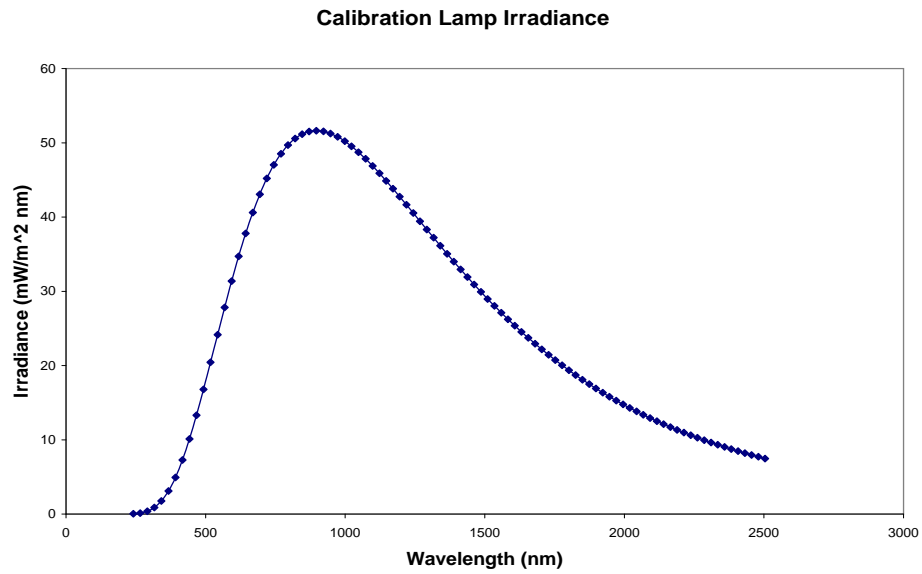
Figure B.1: $I_s(\lambda)$ Oriels Quartz Tungsten Halogen lamp calibration curve.

The irradiance $I_s(\lambda)$ (in mWatt/m^{2}nm) for different wavelengths can be calculated by using the fitting equation for non-NIST wavelengths [82]

$$I_s(\lambda) = \lambda^{-5}(C + D\lambda^{-1} + E\lambda^{-2} + F\lambda^{-3} + G\lambda^{-4} + H\lambda^{-5})e^{(A+B\lambda^{-1})} \qquad \text{(B.1)}$$

With the parameters shown in table B.1.

A =	42.9337969819961	E =	−17471.4519022005
B =	−4482.03454943898	F =	2832760.57547414
C =	0.986818227760581	G =	−1063959488.41395
D =	31.3179591896986	H =	0.00000

Table B.1: Oriel Model QTH 200W Calibration Curve Parameters

Irradiance tables are also available from Oriel Calibration Datasheets. Irradiance is given 1, 10, and 100 nm. The source was calibrated with a reference NIST source [82]. The uncertainty is smallest at about 700 nm (see table B.2).

Wavelength(nm)	250	350	654.6	900	1300	1600	2000	2400
Uncertainty(%)	2.7	1.85	1.75	1.85	1.88	2.45	3.07	4.87

Table B.2: Irradiance uncertainty at different wavelengths for the QTH 200W lamp.

B.2.6 Calibration

With the lamp calibrated according to Oriel's specifications, the spectrometer is now ready to be calibrated as a function of wavelength, and to evaluate the response at different wavelengths. We can now write the expression that relates the measured irradiance with the lamp's irradiance

$$I_m(\lambda) = T_{acq}R(\lambda)I_s(\lambda) \tag{B.2}$$

Where $I_m(\lambda)$ is the irradiance as measured by the spectrometer, T_{acq} is the acquisition time of the camera (in our case 4 sec) in the non-saturation region, $R(\lambda)$ is the response function of the system, and $I_s(\lambda)$ is the calibration lamp irradiance. From this equation we can simply solve for the response function of the system $R(\lambda)$ as a function of the wavelength. Knowing the response function of the system we can now compensate any experimental measurement as a function of wavelength of the spectrometer. We simply write the solution as

$$R(\lambda) = \frac{I_m(\lambda)}{T_{acq}I_s(\lambda)} \tag{B.3}$$

B.3 Measurements

A range between 275 and 1075 nm was selected for the spectroscopy measurements, this range was selected due to mechanical limitations of the spectrometer. We are showing the selected instrumental central wavelength for each spectral "window" (see table B.3), and the actual or real central experimental wavelength (see table B.4). The wavelength calibration of the spectrometer has been performed earlier, details can be found in the internal report [83].

Wavelengths(nm)	275	300	325	350	375	400	425	450	475
	500	525	550	575	600	625	650	675	700
	725	750	775	800	825	850	875	900	925
	950	975	1000	1025	1050	1075			

Table B.3: Selected experimental central wavelengths

Wavelengths(nm)	265.62	291.51	316.62	341.62	366.97	392.00	417.08
	442.35	467.45	492.66	517.77	542.95	568.12	593.29
	618.54	643.66	669.02	694.06	719.15	744.60	769.83
	795.00	820.50	845.66	871.10	896.63	922.04	947.50
	972.95	998.44	1022.59	1047.83	1073.06		

Table B.4: Measured experimental central wavelengths

In figure B.2 we can see the relation between instrumental and real wavelengths.

Experimental Selected Wavelength vs Mesured Experimental Wavelength
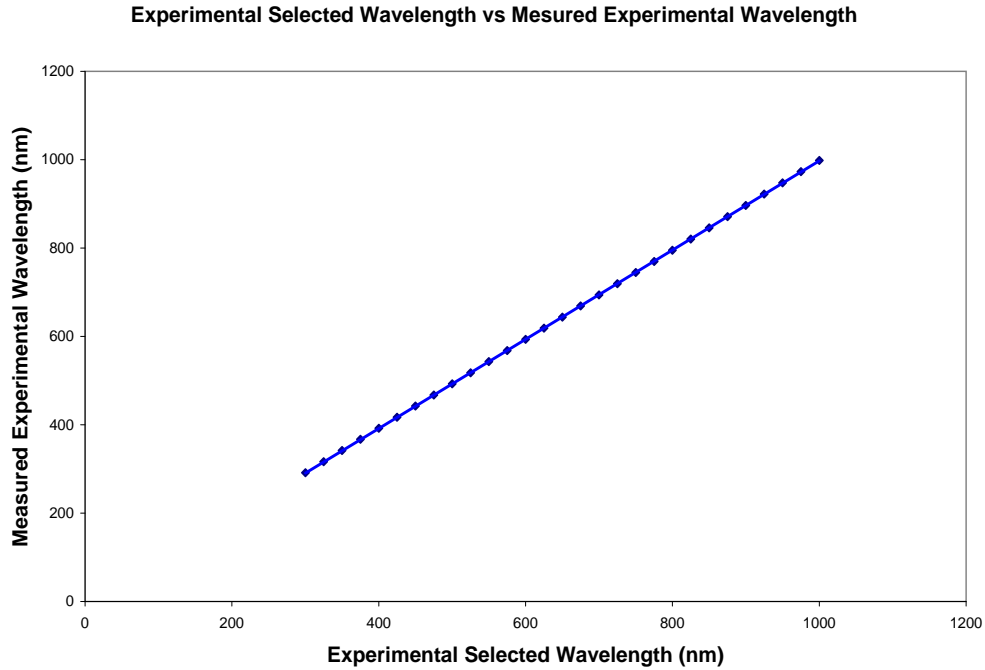
Figure B.2: Relation between actual wavelength and instrumental wavelength.

Fitting the curve with a linear equation, we find the relation between the two. We now find any actual wavelength λ_A by using the following equation

$$\lambda_A(\lambda_I) \approx 1.0093\lambda_I - 11.939 \tag{B.4}$$

where λ_I is the instrumental wavelength read on the monochromator. After the central wavelength correction for each specific spectral "window" is given, we now show in figure B.3 the experimental averaged results of the irradiance as a function of wavelength $I_m(\lambda)$, expressed as number of counts. We also see the regions where the measured intensity drops. Comparing with the fiber optic's response we conclude that those drops match the regions of absorption in the fiber.

Figure B.4 shows how the measured intensity drops also affect the system response function as a function of wavelength. Notice that we are showing the results of all the spectral "windows" with the same central wavelength values from table B.4.

Experimental Averaged Irradiance vs Wavelength
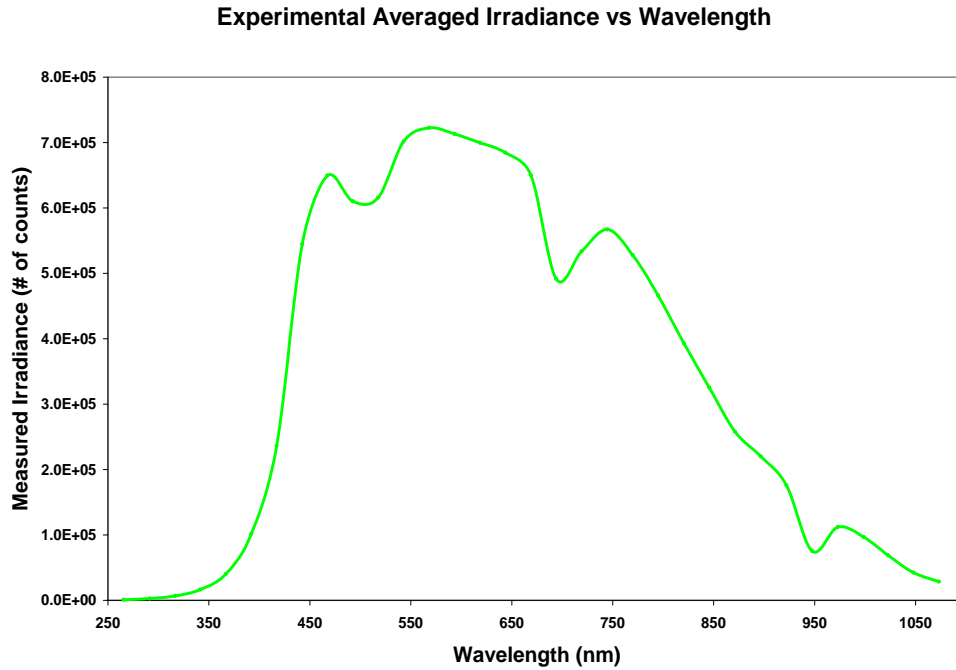
Figure B.3: $I_m(\lambda)$ Experimental averaged irradiance as a function of wavelength.

Finally having the experimental averaged irradiance, the calibration lamp irradiance, and the acquisition time we now use equation (B.3) to compute the system response function as a function of wavelength $R(\lambda)$.

Figure B.4 shows the computed system response function $R(\lambda)$.

Response Function vs Wavelength
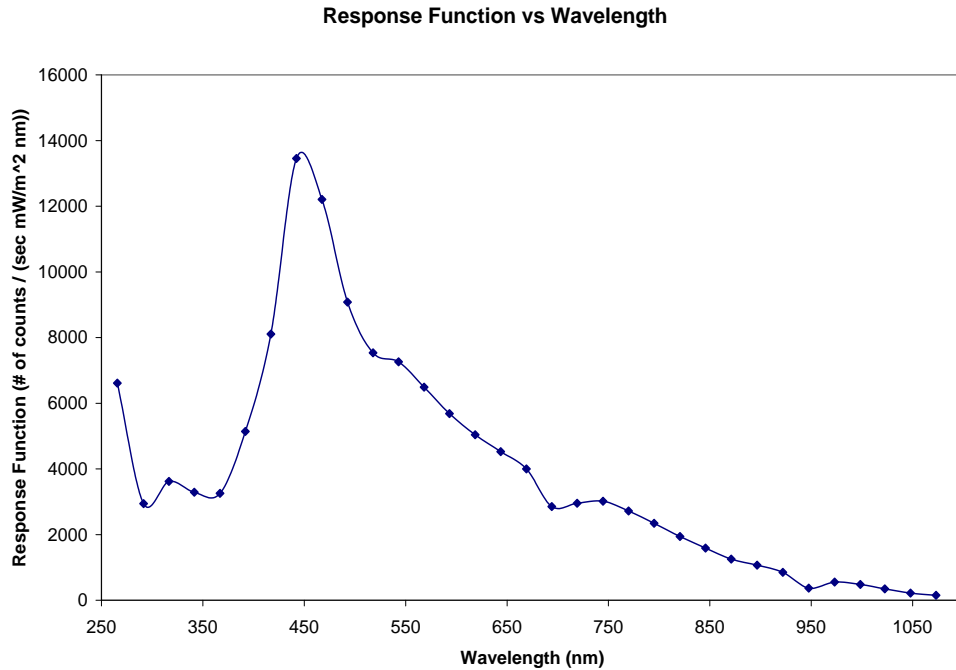
Figure B.4: $R(\lambda)$ System response function as a function of wavelength.

As we can see in figure B.4, the maximum response of the system is observed at 448 nm. Minimum response is observed in the IR (for $\lambda > 1000$ nm). The spectral region between 275 and 300 nm is subject to the greatest uncertainty because of the low irradiance of the lamp at these wavelengths. The system response function cannot be described by a simple expression. However, we can reproduce the data accurately by combining a set of fit equations for different wavelength regions. Table B.5 shows the values obtained using the fit for the different wavelengths from 266 to 1075 nm. Having the values of the system response function, the acquisition time, and the experimental measured value we now rearrange equation (B.2) to solve for the "real" experimental value

$$I_{exp}(\lambda) = \frac{I_m(\lambda)}{T_{acq}R(\lambda)}$$

(B.5)

Table B.5: Numerical values for the system response as a function of wavelength (λ vs $R(\lambda)$).

265	1867.73	306	1916.73	347	2462.82	388	4759.08	429	10213.65
266	1860.26	307	1920.45	348	2493.15	389	4845.65	430	10418.97
267	1853.96	308	1924.33	349	2524.60	390	4933.92	431	10629.57
268	1848.75	309	1928.40	350	2557.17	391	5023.89	432	10845.64
269	1844.52	310	1932.68	351	2590.89	392	5115.61	433	11067.37
270	1841.19	311	1937.19	352	2625.78	393	5209.11	434	11294.98
271	1838.67	312	1941.95	353	2661.83	394	5304.40	435	11528.66
272	1836.88	313	1946.98	354	2699.08	395	5401.54	436	11768.64
273	1835.76	314	1952.32	355	2737.53	396	5500.54	437	12015.15
274	1835.22	315	1957.98	356	2777.20	397	5601.45	438	12268.42
275	1835.22	316	1963.99	357	2818.10	398	5704.32	439	12528.70
276	1835.68	317	1970.38	358	2860.24	399	5809.17	440	12796.24
277	1836.55	318	1977.17	359	2903.64	400	5916.05	441	13071.30
278	1837.78	319	1984.38	360	2948.30	401	6025.02	442	13392.51
279	1839.33	320	1992.05	361	2994.24	402	6136.12	443	13498.20
280	1841.14	321	2000.20	362	3041.47	403	6249.40	444	13552.14
281	1843.19	322	2008.85	363	3090.01	404	6364.91	445	13593.25
282	1845.43	323	2018.03	364	3139.85	405	6482.72	446	13622.09
283	1847.83	324	2027.78	365	3191.02	406	6602.89	447	13639.18
284	1850.37	325	2038.10	366	3243.52	407	6725.47	448	13645.06
285	1853.01	326	2049.04	367	3297.36	408	6850.55	449	13640.25
286	1855.74	327	2060.61	368	3352.56	409	6978.18	450	13625.24
287	1858.54	328	2072.84	369	3409.13	410	7108.44	451	13600.55
288	1861.38	329	2085.76	370	3467.07	411	7241.41	452	13566.66
289	1864.26	330	2099.39	371	3526.40	412	7377.18	453	13524.06
290	1867.17	331	2113.76	372	3587.12	413	7515.83	454	13473.21
291	1870.09	332	2128.89	373	3649.25	414	7657.44	455	13414.57
292	1873.03	333	2144.81	374	3712.81	415	7802.12	456	13348.61
293	1875.97	334	2161.54	375	3777.79	416	7949.96	457	13275.76
294	1878.91	335	2179.10	376	3844.22	417	8101.07	458	13196.46
295	1881.86	336	2197.52	377	3912.10	418	8255.55	459	13111.14
296	1884.82	337	2216.81	378	3981.45	419	8413.52	460	13020.21
297	1887.79	338	2237.01	379	4052.28	420	8575.10	461	12924.07
298	1890.78	339	2258.14	380	4124.61	421	8740.40	462	12823.12
299	1893.80	340	2280.20	381	4198.45	422	8909.56	463	12717.76
300	1896.86	341	2303.24	382	4273.82	423	9082.71	464	12608.36
301	1899.97	342	2327.26	383	4350.73	424	9260.00	465	12495.29
302	1903.13	343	2352.28	384	4429.20	425	9441.55	466	12378.91
303	1906.38	344	2378.33	385	4509.25	426	9627.54	467	12259.57
304	1909.72	345	2405.42	386	4590.90	427	9818.10	468	12137.62
305	1913.16	346	2433.58	387	4674.17	428	10013.42	469	12013.38

470	11887.17	510	7791.51	550	7087.07	590	5780.47	630	4793.19
471	11759.32	511	7748.28	551	7057.98	591	5750.76	631	4772.96
472	11630.13	512	7708.27	552	7028.13	592	5721.34	632	4752.88
473	11499.89	513	7671.39	553	6997.61	593	5692.19	633	4732.96
474	11368.88	514	7637.57	554	6966.47	594	5663.33	634	4713.18
475	11237.39	515	7606.69	555	6934.78	595	5634.75	635	4693.54
476	11105.68	516	7578.67	556	6902.60	596	5606.45	636	4674.03
477	10974.01	517	7553.38	557	6869.99	597	5578.43	637	4654.65
478	10842.62	518	7530.71	558	6837.01	598	5550.68	638	4635.38
479	10711.77	519	7510.52	559	6803.69	599	5523.21	639	4616.22
480	10581.67	520	7492.66	560	6770.10	600	5496.02	640	4597.15
481	10452.54	521	7476.99	561	6736.27	601	5469.10	641	4578.17
482	10324.61	522	7463.35	562	6702.26	602	5442.44	642	4559.26
483	10198.07	523	7451.57	563	6668.09	603	5416.05	643	4540.41
484	10073.11	524	7441.47	564	6633.81	604	5389.93	644	4521.61
485	9949.92	525	7432.86	565	6599.45	605	5364.07	645	4502.84
486	9828.68	526	7425.54	566	6565.04	606	5338.47	646	4484.09
487	9709.54	527	7419.31	567	6530.62	607	5313.12	647	4465.34
488	9592.66	528	7413.95	568	6496.22	608	5288.03	648	4446.58
489	9478.19	529	7409.24	569	6461.86	609	5263.18	649	4427.78
490	9366.27	530	7404.94	570	6427.57	610	5238.58	650	4408.93
491	9257.03	531	7400.81	571	6393.36	611	5214.23	651	4390.01
492	9150.57	532	7396.59	572	6359.27	612	5190.11	652	4370.98
493	9047.02	533	7392.02	573	6325.31	613	5166.24	653	4351.84
494	8946.47	534	7386.83	574	6291.49	614	5142.59	654	4332.55
495	8849.01	535	7380.74	575	6257.84	615	5119.18	655	4313.08
496	8754.73	536	7373.46	576	6224.38	616	5095.99	656	4293.41
497	8663.70	537	7364.69	577	6191.10	617	5073.03	657	4273.50
498	8575.97	538	7354.11	578	6158.04	618	5050.29	658	4253.33
499	8491.60	539	7341.42	579	6125.19	619	5027.76	659	4232.86
500	8410.65	540	7326.29	580	6092.57	620	5005.45	660	4212.05
501	8333.13	541	7308.36	581	6060.19	621	4983.35	661	4190.86
502	8259.08	542	7285.24	582	6028.05	622	4961.45	662	4169.25
503	8188.51	543	7263.05	583	5996.17	623	4939.75	663	4147.18
504	8121.44	544	7241.50	584	5964.55	624	4918.26	664	4124.60
505	8057.85	545	7218.59	585	5933.18	625	4896.95	665	4101.47
506	7997.74	546	7194.43	586	5902.09	626	4875.84	666	4077.73
507	7941.09	547	7169.11	587	5871.27	627	4854.91	667	4053.33
508	7887.86	548	7142.72	588	5840.73	628	4834.17	668	4028.21
509	7838.02	549	7115.35	589	5810.46	629	4813.60	669	4002.32

670	3975.59	710	2939.75	750	2934.04	790	2449.03	830	1782.71
671	3947.95	711	2944.93	751	2927.25	791	2432.83	831	1767.22
672	3919.34	712	2949.95	752	2920.13	792	2416.52	832	1751.86
673	3889.69	713	2954.77	753	2912.69	793	2400.11	833	1736.63
674	3858.91	714	2959.40	754	2904.93	794	2383.61	834	1721.53
675	3826.94	715	2963.81	755	2896.84	795	2367.02	835	1706.58
676	3793.68	716	2968.01	756	2888.44	796	2350.35	836	1691.77
677	3759.05	717	2971.97	757	2879.72	797	2333.60	837	1677.10
678	3722.96	718	2975.70	758	2870.70	798	2316.79	838	1662.58
679	3685.32	719	2979.18	759	2861.37	799	2299.93	839	1648.21
680	3646.02	720	2982.39	760	2851.74	800	2283.01	840	1633.99
681	3604.96	721	2985.35	761	2841.81	801	2266.04	841	1619.93
682	3562.04	722	2988.03	762	2831.59	802	2249.03	842	1606.03
683	3517.14	723	2990.43	763	2821.08	803	2232.00	843	1592.29
684	3470.14	724	2992.54	764	2810.29	804	2214.94	844	1578.72
685	3420.93	725	2994.36	765	2799.22	805	2197.85	845	1565.30
686	3369.37	726	2995.88	766	2787.88	806	2180.76	846	1552.06
687	3315.34	727	2997.10	767	2776.28	807	2163.66	847	1538.98
688	3258.69	728	2998.01	768	2764.40	808	2146.57	848	1526.07
689	3199.29	729	2998.60	769	2752.27	809	2129.47	849	1513.33
690	3136.98	730	2998.87	770	2739.90	810	2112.40	850	1500.76
691	3071.62	731	2998.83	771	2727.27	811	2095.34	851	1488.36
692	3003.03	732	2998.45	772	2714.40	812	2078.31	852	1476.13
693	2931.07	733	2997.75	773	2701.30	813	2061.31	853	1464.07
694	2850.14	734	2996.71	774	2687.98	814	2044.35	854	1452.19
695	2850.65	735	2995.34	775	2674.43	815	2027.44	855	1440.48
696	2856.66	736	2993.64	776	2660.66	816	2010.57	856	1428.94
697	2862.74	737	2991.59	777	2646.69	817	1993.76	857	1417.57
698	2868.88	738	2989.21	778	2632.52	818	1977.01	858	1406.37
699	2875.04	739	2986.49	779	2618.15	819	1960.33	859	1395.34
700	2881.22	740	2983.42	780	2603.59	820	1943.72	860	1384.48
701	2887.38	741	2980.02	781	2588.84	821	1927.18	861	1373.78
702	2893.53	742	2976.27	782	2573.92	822	1910.74	862	1363.26
703	2899.62	743	2972.18	783	2558.83	823	1894.37	863	1352.89
704	2905.66	744	2967.74	784	2543.58	824	1878.11	864	1342.69
705	2911.62	745	2962.97	785	2528.17	825	1861.93	865	1332.64
706	2917.49	746	2957.86	786	2512.61	826	1845.87	866	1322.76
707	2923.25	747	2952.41	787	2496.91	827	1829.91	867	1313.02
708	2928.89	748	2946.62	788	2481.08	828	1814.06	868	1303.44
709	2934.39	749	2940.49	789	2465.11	829	1798.32	869	1294.01

870	1284.72	912	948.33	954	454.57	996	493.90	1038	265.00
871	1275.58	913	938.93	955	465.05	997	489.21	1039	259.91
872	1266.57	914	929.31	956	474.81	998	484.43	1040	254.88
873	1257.70	915	919.44	957	483.87	999	479.54	1041	249.91
874	1248.95	916	909.32	958	492.26	1000	474.56	1042	245.02
875	1240.33	917	898.93	959	500.00	1001	469.49	1043	240.20
876	1231.84	918	888.25	960	507.11	1002	464.34	1044	235.46
877	1223.46	919	877.28	961	513.62	1003	459.12	1045	230.78
878	1215.19	920	866.00	962	519.54	1004	453.83	1046	226.20
879	1207.02	921	854.39	963	524.90	1005	448.48	1047	221.70
880	1198.96	922	842.43	964	529.72	1006	443.07	1048	217.30
881	1190.99	923	830.12	965	534.01	1007	437.61	1049	212.98
882	1183.10	924	817.44	966	537.80	1008	432.10	1050	208.76
883	1175.30	925	804.36	967	541.10	1009	426.55	1051	204.64
884	1167.58	926	790.88	968	543.93	1010	420.97	1052	200.63
885	1159.92	927	776.98	969	546.32	1011	415.34	1053	196.73
886	1152.33	928	762.64	970	548.27	1012	409.70	1054	192.94
887	1144.79	929	747.84	971	549.81	1013	404.03	1055	189.28
888	1137.30	930	732.57	972	550.95	1014	398.34	1056	185.73
889	1129.84	931	716.82	973	551.70	1015	392.64	1057	182.31
890	1122.42	932	700.55	974	552.08	1016	386.92	1058	179.04
891	1115.03	933	683.76	975	552.11	1017	381.20	1059	175.89
892	1107.64	934	666.43	976	551.81	1018	375.47	1060	172.90
893	1100.27	935	648.55	977	551.18	1019	369.74	1061	170.05
894	1092.89	936	630.08	978	550.24	1020	364.02	1062	167.36
895	1085.51	937	611.02	979	549.01	1021	358.30	1063	164.84
896	1078.10	938	591.34	980	547.49	1022	352.59	1064	162.48
897	1070.66	939	571.03	981	545.70	1023	346.89	1065	160.30
898	1063.18	940	550.07	982	543.65	1024	341.21	1066	158.30
899	1055.65	941	528.44	983	541.36	1025	335.55	1067	156.49
900	1048.07	942	506.12	984	538.83	1026	329.91	1068	154.88
901	1040.41	943	483.09	985	536.07	1027	324.29	1069	153.48
902	1032.67	944	459.33	986	533.11	1028	318.71	1070	152.28
903	1024.84	945	434.82	987	529.94	1029	313.15	1071	151.31
904	1016.91	946	409.54	988	526.58	1030	307.63	1072	150.57
905	1008.86	947	371.22	989	523.04	1031	302.14	1073	150.07
906	1000.69	948	375.19	990	519.32	1032	296.70	1074	149.81
907	992.38	949	390.51	991	515.44	1033	291.29	1075	149.81
908	983.92	950	404.97	992	511.41	1034	285.93		
909	975.30	951	418.57	993	507.23	1035	280.63		
910	966.50	952	431.36	994	502.91	1036	275.35		
911	957.52	953	443.35	995	498.47	1037	270.15		

BIBLIOGRAPHY

[1] D. R. Bates, A. E. Kingston, and R. W. P. McWhirter, *Proc. Royal Soc. London.*, vol. 267, pp. 297, 1962.

[2] N. R. Badnell, *J. Phys. B*, vol. 19, pp. 3827, 1986.

[3] Graphical Autostructure Code, *http://vanadium.rollins.edu/GASP/GASP.html*.

[4] G. H. Golub and C. F. Van Loan, *Johns Hopkins University Press*, vol. 1, pp. 8.3, 1989.

[5] A. Burgess, M. C. Chidichimo, and J. A. Tully, *J. Phys. B.*, vol. 30, pp. 33, 1997.

[6] D. C. Griffin, C. P Ballance, S. D. Loch, and M. S. Pindzola, *J. Phys. B*, vol. 40, pp. 4537, 2007.

[7] C. T. Johnson and A. E. Kingston, *J. Phys. B.*, vol. 23, pp. 3393, 1990.

[8] M. E. Galavis, C. Mendoza, and C. J. Zeippen, *A&A. Suppl. Ser.*, vol. 111, pp. 347, 1995.

[9] H. E. Saraph, *Comput. Phys. Commun.*, vol. 15, pp. 247, 1978.

[10] F. P. Keenan and S. M. McCann, *J. Phys. B.*, vol. 23, pp. L423, 1990.

[11] *http://www.adas.ac.uk*.

[12] H. P. Summers and M. B. Hooper, *Plasma Phys.*, vol. 25, pp. 1311, 1983.

[13] H. P. Summers, W. J. Dickson, M. G. O'Mullane, N. R. Badnell, A. D. Whiteford, D. H. Brooks, J. Lang, S. D. Loch, and D. C. Griffin, *Plasma Phys. and Control. Fusion*, vol. 48, pp. 263, 2006.

[14] A. Burgess and H. P. Summers, *Mon. Not. R. Astron. Soc.*, vol. 174, pp. 345, 1976.

[15] J. A. Bittencourt, *Fundamentals of Plasma Physics*, Springer-Verlag, Ney York, NY, 3rd Edition, 2004.

[16] R. D. Cowan, *The Theory of Atomic Structure and Spectra*, University of California Press, Berkeley and Los Angeles, CA, 1st Edition, 1981.

[17] E. U. Condon and H. Odabasi, *Atomic Structure*, Cambridge University Press, New York, NY, 1st Edition, 1980.

[18] D. W. Norcross and M. J. Seaton, *J. Phys. B: At. Mol.*, vol. 9, pp. 2983, 1976.

[19] W. Eissner, M. Jones, and H. Nussbaumer, *Comput. Phys. Commun.*, vol. 8, pp. 270, 1974.

[20] Jr. J. Abdallah, R. E. H. Clark, and R. D. Cowan, *Theoretical atomic physics code development I CATS: cowan atomic structure code*, 1988.

[21] N. R. Badnell, M. S. Pindzola, I. Bray, and D. C. Griffin, *J. Phys. B*, vol. 31, pp. 911, 1998.

[22] NIST ASD Team, *NIST Atomic Spectra Database (version 3.1.5), [Online]*, National Institute of Standards and Technology, Gaithersburg, MD, http://physics.nist.gov/asd3 Edition, 2008.

[23] M. A. Bautista, *J. Phys. B: At. Mol. Opt. Physics*, vol. 41, pp. 65701, 2008.

[24] P. G. Burke, *Potential Scattering in Atomic Physics*, Plenum Press, Ney York, NY, 1st Edition, 1977.

[25] D. J. Griffiths, *Introduction to Quantum Mechanics*, Pearson-Prentice Hall, Upper Saddle River, NJ, 2nd Edition, 2005.

[26] M. Inokuti, *Inelastic Collisions of Fast Charged Particles with Atoms and Molecules-the Bethe Theory Revisited.*, Reviews of Modern Physics, Argonne, IL 60439, 1nd Edition, 1971.

[27] E. P. Wigner and L. Eisenbud, *Phys. Rev. Letts.*, vol. 72, pp. 29, 1947.

[28] P. G. Burke, A. Hibbert, and W. D. Robb, *J. Phys. B: At. Mol. Phys.*, vol. 4, pp. 153, 1971.

[29] P. G. Burke and K. A. Berrington, *J. Atomic and Molecular Processes an R-Matrix Approach*, Institute of Physics Publishing, Bristol and Philadelphia, 1993.

[30] F. F. Chen, "Langmuir Probe Diagnostics," in *IEEE-ICOPS*, Jeju, Korea, June 2003, pp. 2–29.

[31] I. H. Hutchinson, *Principles of Plasma Diagnostics*, Cambridge University Press, Cambridge, UK, 1st Edition, 1987.

[32] H. M. Mott-Smith and I. Langmuir, *Phys. Rev. Letts.*, vol. 28, pp. 727–763, 1926.

[33] R. F. Boivin, *ASTRAL Spectrometer and Diagnostics. Internal Report AU008*, Auburn-University, Auburn, AL, 2006.

[34] McPherson, *Instruction Manual for the Model 209, 1.33 Meter Scanning Monochromator*, McPherson, Inc., Chelmsford, MA, 1st Edition, 1998.

[35] KestrelSpec, *KestrelSpec for Windows Software Manual*, Catalina Scientific Corp., Tucson, AZ, 1st Edition, 2003.

[36] D. G. Whyte, T. C. Jernigan, D. A. Humphreys, A. W. Hyatt, C. J. Lasnier, P. B. Parks, T. E. Evans, M. N. Rosenbluth, P. L. Taylor, A. G. Kellman, D. S. Gray, E. M. Hollmann, and S. K. Combs, *Phys. Rev. Letts.*, vol. 89, pp. 055001, 2002.

[37] M. Mattioli, K. B. Fournier, L. Carraro, I. Coffey, C. Giroud, K. Lawson, P. Monier-Garbet , M. O'Mullane, J. Ongena, M. E. Puiatti, F. Sattin, P. Scarin, and M. Valisa, *J. Phys. B: At. Mol. Opt. Phys.*, vol. 34, pp. 127, 2001.

[38] S. D. Loch, Sh. A. Abdel-Naby, C. P. Ballance, and M. S. Pindzola, *Phys. Rev.*, vol. 76, pp. 22706, 2007.

[39] R. Boswell, *Plasma Phys. Control. Fusion*, vol. 26, pp. 1147, 1984.

[40] F. F. Chen, *Plasma Phys. Control. Fusion*, vol. 33, pp. 339, 1991.

[41] C. Diaz, "An Overview of the VASIMIR Engine: High Power Space Propulsion with RF Plasma Generation and Heating" in *RADIO FREQUENCY POWER IN PLASMAS, 14th Topical Conference*, Oxnard, CA, Apr. 2001, p. 595.

[42] J. Khachan, C. Carter, B. James, and I. Falconer, "Helicon Wave and Ion Density Measurements in an RF Plasma Deposition Reactor" in *APS, Gaseous Electronics Conference*, Argonne, IL, Oct. 1996, p. 16.

[43] N. R. Badnell, M. G. O'Mullane, H. P. Summers, Z. Altun, M. A. Bautista, J. Colgan, T. W. Gorczyca, D. M. Mitnik, M. S. Pindzola, and O. Zatsarinny, *A&A*, vol. 406, pp. 1151, 2003.

[44] M. F. Gu, *The Ap. J.*, vol. 590, pp. 1131–1140, 2003.

[45] C. P. Ballance, D. C. Griffin, M. S. Pindzola, and S. D. Loch, *J. Phys. B*, vol. 40, pp. F27, 2007.

[46] N. R. Badnell, *The Astrophysical Jourmnal Supplement Series*, vol. 167, pp. 334, 2006.

[47] D. C. Griffin, M. S. Pindzola, J. A. Shaw, N. R. Badnell, M. G. O'Mullane, H. P. Summers, *J. Phys. B*, vol. 30, pp. 3543, 1997.

[48] J. M. Munoz Burgos, C. P. Ballance, S. D. Loch, and R. F. Boivin, *A&A*, (Accepted 03/12/09), 2009.

[49] F. P. Keenan and E. S. Conlon, *The Astrophysical Journal.*, vol. 410, pp. 426, 1993.

[50] L. H. Aller and C. D. Keyes, *The Astrophysical Journal Supplement Series.*, vol. 65, pp. 405, 1987.

[51] E. Perez-Montero, G. F. Hagele, T. Contini, and A. Diaz, *Mon. Not. R. Astron. Soc.*, vol. 381, pp. 125, 2007.

[52] M. M. De Robertis, R. J. Dufour, and R. W. Hunt, *J. Roy. Astron. Soc. Can.*, vol. 81, pp. 195, 1987.

[53] C. P. Ballance and D. C. Griffin, *J. Phys. B.*, vol. 41, pp. 065201, 2008.

[54] D. C. Griffin, C. P. Ballance, S. D. Loch, and M. S. Pindzola, *J. Phys. B: At. Mol. Opt. Phys.*, vol. 40, pp. 4537, 2007.

[55] D. H. Madison, A. Dasgupta, K. Bartschat, and D. Valid, *J. Phys. B.*, vol. 37, pp. 1073, 2004.

[56] M. E. Galavis, C. Mendoza, and C. J. Zeippen, *A&A. Suppl. Ser.*, vol. 133, pp. 245, 1998.

[57] D. C. Griffin, N. R. Badnell, and M. S. Pindzola, *J. Phys. B.*, vol. 31, pp. 3713, 1998.

[58] C. P. Ballance and D. C. Griffin, *J. Phys. B.*, vol. 41, pp. 195205, 2008.

[59] D. M. Mitnik, D. C. Griffin, C. P. Ballance, and N. R. Badnell, *J. Phys. B: At. Mol. Opt. Phys.*, vol. 36, pp. 717, 2003.

[60] C. P. Ballance and D. C. Griffin, *J. Phys. B.*, vol. 37, pp. 2943–2957, 2004.

[61] K. A. Berrington, W. B. Eissner, and P. H. Norrington, *Comput. Phys. Commun.*, vol. 92, pp. 290, 1995.

[62] *http://www-cfadc.phy.ornl.gov/data_and_codes*.

[63] C. Mendoza and C. J. Zeippen, *Mon. Not. R. Astr. Soc.*, vol. 202, pp. 981, 1983.

[64] A. Burgess, *J. Phys. B.*, vol. 7, pp. L364, 1970.

[65] M. C. Witthoeft, A. D. Whiteford, and N. R. Badnell, *J. Phys. B.*, vol. 40, pp. 2969, 2007.

[66] *http://cdsweb.u-strasbg.fr/cgi-bin/qcat?J/A+A/*.

[67] S. A. Moshkalyov, P. G Stenn, S. Gomez, and W. G. Graham, *Appl. Phys. Lett.*, vol. 75, pp. 328, 1999.

[68] P. H. Hauschildt, S. Starrfield, S. N. Shore, F. Allard, and E. Baron, *Astrophys. J.*, vol. 447, pp. 829, 1995.

[69] V. Puech and S. Mizzi, *Appl. Phys.*, vol. 24, pp. 1974, 1991.

[70] V. M. Donnelly, M. V. Malyshev, M. Schabel, A. Kornblit, W. Tai, I. P. Herman, and N. C. M. Fuller, *Plasma S. Sci. and Tech.*, vol. 11, pp. A26–A30, 2002.

[71] C. P. Ballance and D. C. Griffin, *Private Communication*

[72] O. Zatsarinny and K. Bartschat, *J. Phys. B: At. Mol.*, vol. 37, pp. 2173–2189, 2004.

[73] J. E. Chilton, M. D. Stewart Jr, and C. C. Lin, *Phys. Rev. A*, vol. 61, pp. 052708, 2000.

[74] J. B. Boffard, M. L. Keeler, G. A. Piech, L. W. Anderson, and C. C. Lin, *Phys. Rev. A*, vol. 64, pp. 032708, 2001.

[75] C. E. Moore, *Atomic Energy Levels, National Bureau of Standards*, Circular 467, 1949.

[76] V. Zeman and K. Bartschat, *J. Phys. B*, vol. 30, pp. 4609, 1997.

[77] S. Tsurubuchi, K. Arakawa, S. Kinokuni, and K. Motohashi, *J. Phys. B*, vol. 33, pp. 3713, 2000.

[78] E. Machado, E. P. Leal, and G. Csaniak, *Phys. Rev. A*, vol. 29, pp. 1811, 1984.

[79] J. A. del Val, J. A. Aparicio, V. Gonzales, and S. Mar, *A&A*, vol. 357, pp. 1137–1142, 2000.

[80] G. Tachiev and C. F. Fischer, *http://atoms.vuse.vanderbilt.edu/*.

[81] D. H. Madison and W. N. Shelton, *Phys. Rev. Letts.*, vol. 7, pp. 499, 1973.

[82] *Spectra Physics Oriel, Report of Calibration of One Standard of Spectral Irradiance (250 - 2400 nm)*, 2004.

[83] D. Branscomb and R. F. Boivin, *ASTRAL Spectrometer Wavelength Calibration, Ar I Spectrum. Internal Report AU002*, Auburn-University, Auburn, AL, 2005.